UNDERSTANDING DRIVERS OF PRESENT AND FUTURE WATER TEMPERATURE PATTERNS IN A THERMALLY VULNERABLE COASTAL LAGOON

By

Jason J. KarisAllen

Submitted in partial fulfilment of the requirements

of the degree of Master of Applied Science

at

Dalhousie University

Halifax, Nova Scotia

September 2021

dedicated to my wonderful friends, family, and colleagues

TABLE OF CONTENTS

LIST OF TABLES

LIST OF FIGURES

ABSTRACT

Basin Head Harbour is a small coastal lagoon off the shore of Prince Edward Island, Canada, that is becoming increasingly warm in the summer to the detriment of the local biota. Precipitation is transported to the lagoon via groundwater-dominated streams, as well as diffuse and focussed groundwater discharge. The primary contribution of this study was to quantify the focussed (near-shore springs) and indirect (stream baseflow) groundwater delivered to Basin Head Harbour and examine their temperature signatures and influence on lagoon summertime water temperature. Secondly, this study assessed the sensitivity of these cold-water inputs to future climate conditions using a numerical model. The study period spanned the summer of 2019 to the fall of 2020, with a 35-day focussed study occurring between July 23rd and August 26th, 2020. Field investigations applied drone-assisted thermal infrared imaging in combination with a suite of sensors and were complemented by a rigorous literature review. Lagoon water temperatures averaged about 22°C during the summer and were measured above 33°C in some parts of Basin Head Harbour, whereas stream temperatures ranged from 8 to 13°C and spring temperatures ranged from 7 to 10°C. Stream baseflow was estimated to contribute 153,000 m^3 over the focussed study period, whereas the discharge associated with near-shore springs was estimated between 60,000 and 130,000 m^3. Although the overall temperature of the lagoon system is likely largely dominated by solar radiation, focussed and indirect groundwater discharges generated localised cold-water refuges within the lagoon, and the advective heat flux of the springs were of comparable magnitude to the streams. In conjunction with the detailed field investigations, a 1D subsurface model was used to demonstrate that some springs within Basin Head Harbour will likely warm in response to future air temperature increases, although this warming will be at least temporarily attenuated in comparison to atmospheric warming. Results suggested that there is potential for the degree of warming to be negligible to potentially harmful to the ecological health of the harbour, as shallower groundwater may warm more than 2°C by the year 2100. A more complex, robust, and data-rich modelling exercise may engender greater certainty in the future projections of groundwater temperature in Prince Edward Island; however, this study provides compelling preliminary findings and the initial motivation for such a labour-intensive modelling investment.

LIST OF ABBREVIATIONS & SYMBOLS USED

Abbreviation	Description
BHH	Basin Head Harbour
C. crispus	*Chondrus crispus* (Irish moss)
DalWell	Dalhousie Piezometer (located in the Kingsboro watershed)
DELJ	PEI Department of Environment, Labour and Justice
DFO	Fisheries and Oceans Canada
ECCC	Environment and Climate Change Canada
GIM	Giant Irish Moss (giant *Chondrus crispus*)
GsI	Grayscale Intensity
IPCC	Intergovernmental Panel on Climate Change
KW	Kingsboro Watershed
NA	Not Applicable
N.D./ND	No Date or No Data
NE Arm	Northeast Arm (of Basin Head Harbour)
PEI	Prince Edward Island
PEIGov Well	Souris Line Road Government Observation Well
RCP	Representative Concentration Pathway
RMSE	Root Mean Squared Error
RSR	RMSE Normalised with Respect to the Standard Deviation
S	Signal
T	Temperature
TDA	Thermal-Discharge Assessment
TIR	Thermal Infrared
XT2	DJI ZENMUSE™ XT2 Thermal Infrared Camera

Symbol	Description	Units
a	rating curve calibration constant	NA
A_{gauged}	watershed area for the gauged location	m^2
$AreaHigh_n$	high tide plume area of a given spring	m^2
$AreaLow_n$	low tide plume area of a given spring	m^2
$A_{ungauged}$	watershed area for the ungauged location	m^2

b_1	regression fitting coefficient (specific capacity)	NA
C	rating curve calibration constant	NA
C_{ana}	empirical recovery coefficient computed via an electrical resistance analog	NA
C_c	specific capacity coefficient	NA
c_l	specific heat capacity of liquid water	J kg^{-1} °C^{-1}
C_s	specific volumetric heat capacity of given soil (particles)	J kg^{-1} °C^{-1}
E	total evapotranspiration from soil and vegetation	Kg m^{-2} s^{-1}
E_1	exponential integral function	NA
E_{adv}	net advective heat to the lagoon	J
E_{la}	downward longwave radiation absorbed by the lagoon	W m^{-2}
E_{le}	longwave radiation emitted from the lagoon	W m^{-2}
E_{rad}	net radiation to and from the lagoon	W m^{-2}
E_{sh}	downward shortwave radiation absorbed by the lagoon	W m^{-2}
G	soil heat flux	W m^{-2}
h	stream stage	m
H	sensible heat flux	W m^{-2}
H_o	initial well drawdown	m
H_t	final well drawdown at time t	m
i	index value	NA
K	horizontal saturated hydraulic conductivity	m s^{-1}
k_s	soil thermal conductivity	W m^{-1} °C^{-1}
K_{unsat}	unsaturated hydraulic conductivity	m s^{-1}
L_e	length of screen section	m
L_f	latent heat of fusion (ice)	J kg^{-1}
L_v	latent heat of evaporation (liquid water)	J kg^{-1}
m	correction factor for channel meandering	NA
M_{fixed}	fixed head boundary condition	NA
M_{free}	free drainage boundary condition	NA
n	Manning's roughness coefficient	NA
N	total number of springs	NA
n_1	correction factor for stream surface irregularities	NA

n_2	correction factor for variation in stream cross-section shape and size	NA
n_3	correction factor for stream obstruction	NA
n_4	correction factor for stream vegetation and flow conditions	NA
n_{avg}	intermediate estimate of Manning's roughness coefficient (n)	NA
n_b	base value of Manning's roughness coefficient (n) for a straight, uniform, smooth channel of natural materials	NA
n_{bhv}	n estimate from Bedient et al. (2013)	NA
n_{max}	probable highest values of Manning's roughness coefficient (n) from Cowan (1956)	NA
n_{min}	probable lowest values of Manning's roughness coefficient (n) from Cowan (1956)	NA
P	precipitation	mm
P_b	air-entry (bubble) pressure	Pa
P_c	capillary pressure at S_e	Pa
p_v	vapor water density within the soil	kg m^{-3}
Q	stream discharge rate	m^3 s^{-1}
Q_{in}	volume of water discharged to the lagoon	m^3
Q_{pump}	well pumping rate	m^3 s^{-1}
Q_{gauged}	measured flow of the gauged location	m^3 s^{-1}
q_l	liquid water flux	m s^{-1}
$Q_{ungauged}$	calculated flow of the ungauged location	m^3 s^{-1}
q_v	water vapour flux	kg m^{-2} s^{-1}
R	hydraulic radius	m
r	radius of well casing	m
R_{infl}	radius of influence of the pumping well	m
R_n	net all-wave radiation	W m^{-2}
R_{rad}	radial distance from pumping well	m
R_{screen}	radius of well screen	m
R_{solar}	shortwave downwelling solar radiation	W m^{-2}
S_E	energy slope	m m^{-1}
s	well drawdown	m

S_{aq}	aquifer storativity	$m^3\ m^{-3}$
S_c	specific capacity	$m^2\ s^{-1}$
S_e	effective saturation	NA
S_f	storativity of the fracture	$m^3\ m^{-3}$
$StDev.P$	population standard deviation	NA
S_{irr}	relative saturation residual	NA
S_m	storativity of the matrix	$m^3\ m^{-3}$
s_w	change in hydraulic head within the well	m
S_x	relative saturation at given capillary pressure	NA
$T_{0.5}$	absolute lagoon water temperature at half a meter depth	Kelvin
T_{abs}	absolute temperature	Kelvin
T_{calc}	calculated thermal boundary condition	℃
T_{dew}	dewpoint temperature	℃
T_{fixed}	fixed thermal boundary condition	℃
T_{in}	temperature of water discharged to the lagoon	℃
T_{lagoon}	representative temperature of the lagoon	℃
T_{max}	maximum temperature	℃
T_{min}	minimum temperature	℃
$T_{3m\ or\ 7m}$	temperature series extracted from 3 or 7 metres depth in the SHAW surface model domain	℃
t	time	s or days
T	soil temperature	℃
t_{37}	time for the well water level to recover 37%	s
T_{bulk}	bulk transmissivity of aquifer	$m^2\ s^{-1}$
T_f	transmissivity of the fracture	$m^2\ s^{-1}$
T_m	transmissivity of the matrix	$m^2\ s^{-1}$
U	water source/sink term	$m^3\ m^{-3}\ s^{-1}$
V	stream channel velocity	$m\ s^{-1}$
V_{wind}	windspeed	$m\ s^{-1}$
W	rate of radiation emittance	$W\ m^{-2}$
W_S	annual temperature waveform	℃
x_{mean}	mean of observed values	any

x_{model}	modelled value	any
x_{obs}	observed value	any
z	vertical domain distance	m
α	soil media compressibility	$\mathrm{Pa^{-1}}$
β	empirical watershed coefficient 1	NA
φ	empirical watershed coefficient 2	NA
ψ	soil matrix potential	m
ξ	specific capacity regression fitting coefficient	NA
ε_w	emissivity of water	NA
η	sample size	NA
σ	Stefan-Boltzmann constant	$\mathrm{W\ m^{-2}\ K^{-4}}$
λ	pore size distribution index	NA
Θ	rating curve calibration constant	NA
Θ_i	volumetric ice water content	$\mathrm{m^{-3}\ m^{-3}}$
Θ_l	volumetric liquid water content	$\mathrm{m^{-3}\ m^{-3}}$
ρ_i	density of ice (water)	$\mathrm{kg\ m^{-3}}$
ρ_l	density of liquid water	$\mathrm{kg\ m^{-3}}$

ACKNOWLEDGEMNTS

I am enormously grateful for the financial support provided to this project by the Ocean Frontiers Institute Opportunities Fund, the Natural Sciences and Engineering Research Council of Canada (ASPIRE program and CGS-M), Fisheries and Oceans Canada, and Dalhousie University.

Maps throughout this composition were created using ArcGIS® software by Esri. ArcGIS® and ArcMap™ are the intellectual property of Esri and are used herein under license. Copyright © Esri. All rights reserved. For more information about Esri® software, please visit www.esri.com.

Certain climate data for thermal modelling in this report, including solar radiation, humidity, and wind speed, were obtained from the NASA Langley Research Center POWER Project funded through the NASA Earth Science Directorate Applied Science Program.

My colleagues at Dalhousie and my supervisory committee have been instrumental in guiding and assisting this project. Without their various contributions in the field and in the office, this work would not have been feasible. I am honoured by the personal and professional relationships that I have shared with so many of you. A special thank you is extended to my supervisor Dr. Barret Kurylyk, Dr. Aaron Mohammed, Dr. Rob Jamieson, Dr. Shannon Sterling, and Ray Craddock who have invested a considerable amount of time supporting me throughout this process.

I extend my thanks to Dr. Phillipe Renard for their quick and helpful assistance with Hytool; Peter Joostema for providing well pumping data from Souris, PEI; Dr. Joe Tamborski for frequently supporting field planning; and Dr. Serban Danielescu for supplying their historical data and discussing research opportunities. The contributions made by the staff of various organisations (e.g., Fisheries and Oceans Canada, Souris Wildlife, Government of Prince Edward Island, Environment and Climate Change Canada) have been critical to this project, and I extend my appreciation for their efforts. A special thank you is extended to Marie-Hélène Thériault and Dr. Irené Novaczek for sharing their knowledge and enthusiasm.

I would like to end by thanking my family and friends for their support and companionship through my extended academic journey – it would not have been the same without you.

CHAPTER 1: INTRODUCTION

1.1 Problem Statement & Thesis Objectives

Coastal lagoon ecosystems are threatened globally by stressors such as changing sea level, altered water quality, coastal squeeze, erosion, ice dynamics, and human developments (Lemmen et al., 2016). Furthermore, it is anticipated that future climate change will be enormously impactful on marine ecosystems, threatening the social and economic services attributed to them (Anthony et al., 2009; Harley et al., 2006; Lemmen et al., 2016). Approximately 13% of global coastlines have lagoon features (Barnes, 1980), which provide nursery habitat for juvenile fish, nesting and feeding habitat for birds, manage nutrients, sediment, and carbon, serve as recreational boating areas, create birding and fishing opportunities, and shield internal shorelines from wave action (Anthony et al., 2009; Lemmen et al., 2016).

The project site of this thesis is Basin Head Harbour (BHH), Prince Edward Island (PEI), an ecologically degraded coastal lagoon (Figure 1) along the coast of the Kingsboro watershed (KW). This region of PEI is best known for Basin Head Provincial Park, which includes a heritage fisheries museum and beach, and its Marine Protected Area that was established in 2005 under the *Oceans Act* (S.C. 1996, c. 31; DFO, 2009). The BHH Marine Protected Area was established to conserve a distinct morphotype of Irish moss [*Chondrus crispus* or giant Irish moss (GIM)], which exists exclusively within the harbour, and to recover the degraded lagoon[1] ecosystem for fishing, recreation, and tourism purposes (DFO, 2009). Giant Irish moss is of scientific and economic interest, as it has unique reproductive and constitutional properties relative to other varieties (DFO, 2009). Giant Irish moss within BHH experience a variety of anthropogenic and natural stressors that threaten them with extinction. Thus, regulations are in place that prohibit the disturbance,

---

[1] Kjerfve & Magill (1989) defined lagoons as poorly flushed coastal landforms with limited connection to the ocean that are ephemeral on a geologic time scale, which is appropriate in describing BHH.

damage, destruction, or removal of any marine organism or any part of its habitat within the northeast arm (NE Arm) of the Marine Protected Area (Figure 1; DFO, 2009).

Considering that the streams of PEI are groundwater-dominated, and that groundwater also directly discharges to the coast via focussed and diffuse discharge, it is possible that the influence of groundwater on the thermal regime of many small coastal embayments of PEI is significant to their ecological function. Significance in this context would refer to groundwater appreciably reducing the thermal stress on a particular marine species of interest as evidenced by its physiological response or behaviour. In the case of BHH, blue mussels and GIM are approaching catastrophic temperature thresholds (as detailed in Appendix B, Section 1), and critical temperature changes may result if the capacity of groundwater to cool the lagoon is depressed. Thus, understanding the role of groundwater as a thermal control to BHH and its responsiveness to climate change may be important to present and future management initiatives in the lagoon.

The objective of this thesis is to support the continued conservation efforts directed towards the distinct Irish moss morphotype and the BHH ecosystem. This thesis focussed on the hydrogeological characterisation of the local watershed and coastline by exploring the role of fresh groundwater in maintaining survivable thermal stress levels for GIM in BHH. The primary contribution of this study was to quantify the focussed (i.e., near-shore and intertidal springs) and indirect (i.e., stream baseflow) groundwater delivered to BHH and examine their temperature signatures and influence on lagoon water temperature over the summer. Secondly, this study investigated the sensitivity of these cold-water inputs to future climate conditions using a numerical model. The novelty and value of this work, in the context of the initiatives of the Marine Protected Area and the broader field of coastal ecohydrology, will be summarized at the end of this chapter.

1.2 Irish Moss in Basin Head Harbour

The ranges of marine species have been shifting as a result of warming climates, and these changes will likely become more significant in the following decades (Harley et al., 2012). Thus, marine species must have the capacity to tolerate or adapt to more rapidly changing environmental conditions in order to survive (Harley et al., 2012). The long-term persistence of GIM depends on its ability to cope with biotic and abiotic stressors (e.g., water quality, light availability, predation, competition, water depth, and hydraulics; Harley et al., 2012; Raven & Geider, 1988). Stressful conditions are herein defined as conditions that directly or indirectly impact species growth or survival.

The biomass of GIM within BHH declined over 99% from 1980 to 2008, and was measured just above one tonne in 2008 (DFO, 2009). This decline in biomass is what prompted Fisheries and Oceans Canada (DFO) to establish the Marine Protected Area, and it has been attributed to several natural and anthropogenic stressors interacting with the vulnerabilities of GIM. For example, hypoxia and algal blooms, storm events, sediment movement, the predation of mussels by green crab, environmental causes of blue mussel mortality, nutrient inputs, ice damage, and thermal stress have all been regarded as compounding stress factors for GIM within BHH (Joseph et al., 2021). The impending extinction of GIM has since been averted in the short term by extensive and arduous reestablishment programs led by the DFO. However, the sustainability of these successes depends on future monitoring and management action within the watershed (Joseph et al., 2021). Understanding the thermal controls within BHH and along PEI coastlines in general, as well as their sensitivity to climate change, is but one element critical to the informed future management of GIM and other PEI marine resources.

Much of the physiological research about seaweeds is limited in that it predates the modern understanding of future climate change (Harley et al., 2012). Additionally, there is currently an incomplete understanding of the ecophysiology of *C. crispus* (Harley et al., 2012) and the complex ways that climate change will influence their environment. It is not the purpose of this research to elucidate the metabolic intricacies of GIM, but it is important to establish that temperature is inextricably linked to their continued survival. Temperature is a critical consideration in algae ecophysiology, as it exerts a significant degree of control on the enzyme and metabolic functions of all marine organisms (Eggert, 2012; Juanes & McLachlan, 1992a; Raven & Geider, 1988). Common amongst seaweeds, GIM has evolved apt cellular mechanisms to manage thermal stress over various timescales (Davison & Pearson, 1996; Eggert, 2012), but any significant reallocation of resources for this purpose may impede growth and lead to cellular damage or death (Davison & Pearson, 1996). Exact thermal stress thresholds are elusive for the BHH strain of *C. crispus*, but temperatures beyond 30℃ are likely directly detrimental to GIM metabolic activity and survival (see Appendix B, Section 1 for further explication).

C. crispus can reproduce by asexual fragmentation, but this is typically a minor mechanism (Sharp et al., 2003). In contrast, GIM can only reproduce via asexual fragmentation (Sharp et al., 2003). Furthermore, the ability of GIM to anchor to benthic substrates has atrophied, making them reliant on the byssal threads of blue mussels (*Mytilus edulis*) for anchoring (Sharp et al., 2003). Thus, the primary mechanism of successful dispersion of GIM is suspected to be fragmented portions of fronds being recruited by mussel byssal threads (DFO, 2009).

The inability of GIM to anchor itself to substrates is a key vulnerability, in that their survival is dependent on the survival of blue mussels in BHH. The growth and survival of blue mussels also depends on thermal stress, which affects their metabolic function (Almada-Villela et al., 1982; LeBlanc et al., 2005, 2010; Read & Cumming, 1967; Seuront et al., 2019) and susceptibility to predation (Dowd & Somero, 2013). In simple terms, prolonged exposure to temperatures beyond 25-33℃ may adversely impact blue mussel survival (Dowd & Somero, 2013; LeBlanc et al., 2005; Seuront et al., 2019).

Focussing exclusively on thermal stress oversimplifies the complex and dynamic feedback that will occur between GIM and the environmental changes induced by climate change. Nonetheless, considering thermal stress on GIM is essential to effectively managing their continued survival in the future. A more detailed overview of Irish moss and blue mussel ecophysiology is included in Appendix B, Section 1 for reference.

1.3 Groundwater Thermal Sensitivity

Several generalisations are typically adopted when studying the subsurface thermal behaviour of natural systems that facilitate the interpretation of field and modelling data. Subsurface temperatures are driven by their connection with geothermal sources of heat, water flow, soil properties, air temperatures, and radiative fluxes at the surface (Anderson, 2005). Daily and annual air temperatures vary near-harmonically, and these signals propagate into the subsurface. As these signals descend through the soil column, they become dampened and lagged relative to the surface signal (i.e., smaller amplitude and lagged timing) until the harmonic signal is no longer apparent. Typically, the amplitude of diurnal surface temperature signals is measurable down to 1.5 metres (Silliman & Booth, 1993), whereas annual signals may be measured down to 10-15 metres (referred to as the surficial zone; Anderson, 2005; Bense & Kurylyk, 2017; Parsons, 1970). Below the surficial zone the geothermal gradient typically dominates, as temperatures often begin to linearly increase by 1°C per 20-40 metres of depth (Anderson, 2005). Models built on these thermodynamic principles may theoretically be used to predict subsurface temperature and how it may change over time, or alternatively to estimate the source depth of a groundwater discharge based on its temperature or seasonal harmonic signal (e.g., Kurylyk et al., 2015). Although these generalisations are extremely useful in conceptualizing the behaviour of a system, they are non-exhaustive, and variations in the response of the subsurface to surficial and geothermal forcing may vary by locale.

The sensitivity of groundwater resources to climate change has been acknowledged by virtue of inferring past climate trends, land-use conditions, and long-term transience in well temperature profiles (e.g., Bayer et al., 2016; Bense & Kurylyk, 2017; Ferguson & Woodbury, 2005; Mareschal & Beltrami, 1992; Taniguchi et al., 1999). Although long-term datasets are scarce, several studies have documented subsurface temperature increases (e.g., Hemmerle & Bayer, 2020; Riedel, 2019) and water level changes (e.g., Chen et al., 2004) in response to climate change. Bense & Kurylyk (2017) demonstrated that the climate warming signal was capable of propagating downward into the subsurface beyond the surficial zone, and the magnitude of this propagation was dependent on factors such as flow conditions and land-use. Thus, downwelling conditions and concomitant downward heat advection may be expected to more rapidly propagate a multi-decadal warming signal, relative to upwelling conditions (Bense & Kurylyk, 2017). Bayer et al. (2016) demonstrated that the impact of urbanisation on groundwater thermal regime may exceed that of climate warming in cityscapes. Menberg et al. (2014) documented shallow groundwater temperature increases in response to increasing air temperatures over several decades and found that groundwater warming manifested with short lags (<5 years) relative to atmospheric or land surface warming. Similar response times were simulated in a study conducted by Kurylyk, MacQuarrie, and Voss (2014), which further highlighted the importance of changes in the timing and magnitude of recharge and freeze-thaw dynamics on the thermal response of the subsurface.

The impact of seasonal snow cover on subsurface temperature is an important factor to consider in the Atlantic provinces (Kurylyk et al., 2013; Mareschal & Beltrami, 1992; Zhang, 2005) . Land-use, cover changes, topography, and wind dynamics are expected to influence the duration and extent of snowpack accretion and snowmelt processes (Dadic et al., 2010; Szczypta et al., 2015; Zhang, 2005). The inference of past climate conditions from borehole temperature logs and the forward projection of subsurface impacts typically depend on an assumed relationship between atmospheric temperatures and land surface temperatures (e.g., Bayer et al., 2016; Mareschal & Beltrami, 1992; Menberg, Blum, Kurylyk, & Bayer, 2014). However, differences in air and ground temperature have been identified to largely depend on the presence of an insulative snow cover (Kurylyk et al., 2014; Mareschal & Beltrami, 1992; Menberg et al., 2014). For example, snowpack in Eastern Canada has been observed to maintain ground temperatures near freezing when air temperatures drop well below -15°C (Val d'Or, Quebec; Mareschal & Beltrami, 1992). At the same site, soil temperatures at 5 cm depth mirrored air temperatures very closely during the warmer half of the seasonal signal when snowpack was absent (Mareschal & Beltrami, 1992). Increasing air temperatures are expected to impact the extent of snowpack in the Northern Hemisphere as well as the timing of snowmelt events (IPCC, 2014), both of which may influence subsurface thermal regimes (Kurylyk et al., 2014; Mohammed, 2019; Pasha, 2018). Thus, the subsurface thermal dynamics of the KW can be expected to be seasonally affected by freeze-thaw dynamics and their complex interactions with soil hydraulic conductivity and preferential flow pathways (Iwata et al., 2010; Kurylyk et al., 2014; Mohammed, 2019).

Kane et al. (2001) demonstrated that conduction is typically the most important energy flux pathway in soils, particularly in deep subsurface environments due to comparably slow advective transport resulting from lower hydraulic conductivity. However, they also propose that all potential forms of energy transfer should be considered for accurate characterisation of surficial soil thermal regimes, which serve as a boundary condition for underlying soils (Kane et al., 2001). It is conceivable that minor or seasonal thermal processes may have a significant cumulative impact on deeper systems over long timescales, and that shallow systems may be more affected by advective heat transport. An example of a process that is apparent over short timescales is the seasonal mass infiltration of snowmelt, which has been shown to rapidly alter water table temperatures (Kane et al., 2001; Pasha, 2018).

Deforestation affects groundwater thermal regimes by altering the surface energy balance, potentially altering the subsurface thermal profile for centuries following the event (Bense & Beltrami, 2007; Y. Li et al., 2016; A. H. MacDougall & Beltrami, 2017). Large portions of the KW have been deforested for habitation, agriculture, and transport purposes (Government of PEI, 2018), and the thermal impacts of these changes could still be culminating. Prior to European settlement on PEI in the 1720s, the province was estimated to be approximately 98% covered in forests. By the 1900s, only 30% of this coverage remained, which has increased to approximately 44% today (Government of PEI, 2018). Although the exact history of the KW and the impact of deforestation is uncertain, land-use certainly influences the thermal response of the subsurface. Differences in surface temperature are often observable between adjacent forested and non-forested areas that induce subsurface thermal differentiation over time (Bense & Beltrami, 2007; Mareschal & Beltrami, 1992). The subsurface temperatures of the KW may presently be transiently responding to historical land-use and climate change. The aforementioned processes, as well as others not explicitly discussed, are expected to influence future subsurface thermal regimes over the extended timescale of this study (i.e., 2020-2100).

1.4 Groundwater as a Thermal Buffer to Aquatic Systems

Despite adequate documentation of the susceptibility of groundwater systems to climate variation, and the acknowledgment of the important role of groundwater as a thermal buffer for aquatic habitat (e.g., Caissie, 2006; Meisner, Rosenfeld, & Regier, 1988), the impact of climate-induced changes in groundwater temperature on aquatic systems is rarely accounted for in ecological studies (Kaandorp et al., 2019; Kurylyk et al., 2014; Menberg et al., 2014). Groundwater discharge often moderates seasonal extreme temperatures and provides thermal refuges to cold-water aquatic species in streams. These mechanisms have been studied extensively, and some studies have begun to adopt the principles of groundwater thermal sensitivity to climate change in their conceptual models and analysis (e.g., Briggs et al., 2018; Kaandorp et al., 2019). However, several authors have identified the need for an increased understanding of groundwater thermal sensitivity to climate change (e.g., Kanno, Vokoun, & Letcher, 2014; Kurylyk et al., 2014; Mayer, 2012).

Water temperature, climate and climate change, and groundwater influxes have been recognised as important drivers of lagoon ecological functionality (e.g., Anthony et al., 2009; Bintz, Nixon, Buckley, & Granger, 2003; Harley et al., 2006; Kjerfve, 1994; Kjerfve & Magill, 1989; Martínez-Alvarez, Gallego-Elvira, Maestre-Valero, & Tanguy, 2011; Menció et al., 2017; Sadat-Noori et al., 2016). However, few studies have considered the thermal buffering role of groundwater discharges to coastal lagoons (e.g., Chikita et al., 2015; Rodríguez-Rodríguez & Moreno-Ostos, 2006), and a study that has investigated the thermal sensitivity of groundwater to climate change in the context of its role as a thermal control on coastal habitat has not been identified. This is perhaps because the contributions of groundwater are often overlooked or assumed negligible when compared to the water volumes of streamflow or the ocean (e.g., Ryan et al., 2003). Groundwater discharge may be negligible in many coastal environments and for some large-scale studies or objectives, but this generalisation may not extend to studies of small lagoons with notable groundwater input or highly localized studies. Thus, groundwater as a thermal control on lagoon habitats is an area of research still largely unexplored, whereas studies exploring coastal groundwater as a conduit for contaminant transport to the ocean and its importance in water supply management have received notable traction in the literature (e.g., Danielescu et al., 2009; Hansen & Ferguson, 2012b; Sawyer et al., 2016).

Shallow coastal ecosystems may be among some of the more thermally sensitive marine features, possibly making them harbingers of future ecological change within the ocean. Due to the shallow bathymetry and low flushing rates characteristic of lagoons, they are anticipated to be more susceptible to warming conditions than estuaries and open coastlines (Anthony et al., 2009), potentially making lagoons more susceptible to invasive species (e.g., Dowd & Somero, 2013) and oxygen depletion (Bopp et al., 2002). Groundwater inputs may exert a significant degree of control on coastal water temperature (e.g., Bejannin, van Beek, Stieglitz, Souhaut, & Tamborski, 2017; Lee et al., 2016), and this control may be pronounced in shallow embayments with significant groundwater input (e.g., shallow lagoons and estuaries). Thus, groundwater thermal buffering mechanisms in coastal ecosystems may significantly influence the biochemical productivity and survival of temperature-sensitive species like GIM (e.g., Menció et al., 2017; Sadat-Noori et al., 2016). Kjerfve (1994) noted that the relative volumetric importance of surface water and groundwater to lagoons are inversely related. Thus, it is expected that the relative importance of groundwater to coastal systems varies based on the hydrologic conditions of the source watershed, which vary seasonally.

1.5 Thermal Imaging in Hydrogeology: Applications and Challenges

At its outset, thermal imagery was conceived for military applications, but it was adopted by the hydrological community no later than 1967 to study coastal discharge environments (Pluhowski, 1972). Thermal imaging is particularly useful in hydrology for mapping the mixing zone of two interacting sources of water of different temperatures (e.g., cold groundwater discharging into a warm lake). Thermal imaging devices compare measured electromagnetic radiation with a calibrated black body and convert this temperature-dependent difference to electrical signals that can be processed for user interpretation (Pluhowski, 1972). Black-body radiation represents the maximum possible emittance from matter at a given temperature and can be calculated using the Stefan-Boltzmann radiation law (Pluhowski, 1972):

$$W = \sigma {T_{abs}}^4 \tag{1}$$

where W is the rate of radiation emittance (W m^{-2})
σ is the Stefan-Boltzmann constant (W m^{-2} K^{-4})
T_{abs} is the absolute temperature (Kelvin)

In contrast, the measured emittance of a natural material is reduced by various factors like the emissivity, reflectance, and atmospheric attenuation of the signal (Pluhowski, 1972). These environmental factors are typically considered when calibrating raw signal data (FLIR Systems Ltd, 2012).

Thermal imaging devices have been mounted onto planes, helicopters, satellites, and more recently drones. Small aerial drones permit thermal surveying to be more temporally flexible, detailed in resolution, and resource efficient at small scales with respect to conventional aircraft (Jensen et al., 2012). Conversely, conventional aircraft can cover larger areas and have fewer technological challenges associated with data quality at this time (J. Kelly et al., 2019). Thermal satellite images are freely accessible, but often have a very coarse resolution (~100 metres; USGS, 2017) that limits their usefulness in small-scale applications.

Many challenges with drone-assisted thermal infrared (TIR) imaging have been identified by various studies and during our field tests. J. Kelly et al. (2019) identified various challenges with uncooled, non-radiometric cameras, and many of their findings likely extend to comparable radiometric devices when attempting to obtain accurate temperature data. Some of these issues are expected to impact relative temperature readings as well (J. Kelly et al., 2019). Many of the significant issues are associated with the development of thermal orthomosaics because of large discrepancies in temperature measurements between image frames. Vignetting is proposed as a particular concern for single-image analyses, as it has been observed to produce temperature differences between the centre and edge of the image of up to 2.6℃ (J. Kelly et al., 2019).

The environmental conditions during image capture can dramatically impact data quality. Favourable summertime thermal survey conditions include clear skies, low tide, peak temperature contrast, minimal wind, and minimal shadows (Danielescu et al., 2009; Pluhowski, 1972; Roseen, 2002). Intertidal springs are often most apparent during low tides and when there is a pronounced thermal contrast between groundwater and the receiving environment. Wind may alter the angle or stationarity of the camera and cause drone crashes, whereas patchy clouds may generate shadows and attenuate solar radiation nonuniformly. Shadows are smallest around midday and most significant at dusk and dawn.

Despite certain hurdles, thermal imaging has been used to identify locations of groundwater discharge as manifested by thermal anomalies (Coluccio et al., 2020; Danielescu et al., 2009; Johnson et al., 2008; Lee et al., 2016; Mundy et al., 2017; Ozotta & Gerla, 2018; Pluhowski, 1972; Roseen, 2002), evaluate seepage faces (Mundy et al., 2017; Roseen, 2002), assess stream thermal regimes (Jensen et al., 2012), and develop empirical relationships between the geometry of thermal anomalies and their source discharge (Bejannin et al., 2017; Danielescu et al., 2009; Kang et al., 2019; J. L. Kelly et al., 2019; Lee et al., 2016; Mundy et al., 2017; Tamborski et al., 2015) in various environments and at different scales. Empirical correlations between rates of groundwater discharge to coastal environments and the geometry of the thermal plume they generate are of particular interest for this study and will herein be referred to as "thermal-discharge assessments" (TDAs).

The concept that higher discharges result in larger plumes is intuitive; however, conducting TDAs involves several challenges and limitations. The geometry of thermal anomalies generated by the contrast between inputs and receiving waters may vary in time and space as a result of various tidal, daily, seasonal, and decadal climate and hydrodynamic forcing. Lee et al. (2016) demonstrated that plume surface area was negatively correlated with tidal level at two sites in Korea. The negative correlation, although pronounced at both sites, differed as the likely result of variations in coastal bathymetry, hydrodynamics, and groundwater discharge mechanisms (Lee et al., 2016). Likewise, Taniguchi et al. (2019) indicated that TDAs rely on the assumption that variation in the 3D geometry of the plume may be adequately characterised by the 2D variation observed from above, and Bejannin et al. (2017) found that empirical relationships between coastal groundwater discharge and thermal plume area are only transferable between sites when shoreline structure and aquifer characteristics are comparable. They compared several study sites that relate plume surface area to groundwater discharge, and although they all demonstrated pronounced positive correlations, the ultimate relationships differed significantly among sites (Bejannin et al., 2017). Similarly, the relationship between tide level and groundwater discharge is unlikely to be transferable between dissimilar sites (Lee et al., 2016) and is infrequently elucidated due to sampling challenges. As such, measurements must taken at comparable tidal stage and in similar discharge environments when developing empirical TDAs.

Several authors attest that TIR imagery is most effective at capturing coastal groundwater discharge at low tide (Coluccio et al., 2020; Danielescu et al., 2009; Lee et al., 2016). The greater density of sea water relative to freshwater drives freshwater plumes to the surface (Danielescu et al., 2009), allowing the thermal plumes to be detected by TIR sensors. This is a primary advantage of using TIR sensors to identify groundwater discharged to marine environments relative to freshwater environments (e.g., Jensen et al., 2012; Mundy et al., 2017; Ozotta & Gerla, 2018), as TIR sensors are only capable of capturing skin temperature. TDAs based on low-tide sampling exclusively characterise the plumes generated during the shallowest coastal conditions of the tidal cycle, and discharge may be expected to vary with tidal stage and water table fluctuations (Dong-Woon & Byoung-Seol, 2012; Kang et al., 2019; Zamora et al., 2017). If sampling is conducted exclusively in the Atlantic summer months, during which time depressed water tables generate lower coastal hydraulic gradients, then thermal imagery assessments may not identify groundwater discharge pathways present during other times of the year.

The areal magnitude of spring thermal plumes partly depends on the magnitude of the thermal gradient between the water sources and their mixing dynamics. For example, Tamborski et al. (2015) found that larger temperature contrasts were correlated with larger plume areas by studying various areas along the north shore of Long Beach, New York. The respective controls on the temperature of lagoon water and groundwater are complex, as they are numerous and vary in time and space (e.g., source depth of spring discharge, tidal range, weather, hydraulic gradient, shading). The thermal contrast observed during the thermal survey conducted on the north shore of PEI by Danielescu et al. (2009) was approximately 10℃ (i.e., 10℃ groundwater versus 20℃ estuarine water). Adequate thermal contrast is required to locate and differentiate groundwater inputs using TIR sensors, which is why seasonal temperature extremes are often targeted. Ultimately, the thermal plume area of springs is anticipated to increase with increasing thermal contrast, but this is mostly unaccounted for in TDAs. This is a current limitation of this empirical method that may be overcome through more comprehensive sampling in the future, or more physically based models that incorporate thermal dynamics, plume geometry, and channel hydraulics.

Despite the challenges associated with TDAs, strong site-specific correlations have been established at multiple sites as predictive tools (eg., Bejannin et al., 2017; Danielescu et al., 2009; Kelly et al., 2019; Tamborski et al., 2015). Although the drivers of these correlations are physically based, these empirical relationships assume only that the quantity of discharge to coastal water bodies may be effectively estimated by plume planar surface area. TDAs are data-driven, and their potential value should not be overlooked where accurate physical models for coastal groundwater discharge processes are either unavailable, impractical, or unapproachable for general industrial or research applications. The complicating factors do limit the confidence one should invest into the upscaling or transfer of TDAs between sites, particularly when similarities in site conditions are limited. TDAs must be applied with appropriate consideration of uncertainty, but may serve as powerful tools to derive first-order estimates of coastal groundwater discharge

(Danielescu et al., 2009). Ultimately, empirical methods require good data and competent application to entrain effective predictive capacity, but they regularly offer more efficient or practicable solutions relative to physically comprehensive methods. More complex data-driven models may be considered that account for geomorphologic, hydrogeologic, and hydrodynamic factors in the future that may empower the accuracy and physical defensibility of TDAs.

1.6 Thesis Contributions

The studies referenced in the previous sections have shown that groundwater systems will likely respond to future climate warming. Groundwater inputs to various aquatic systems have been recognized for their ability to temper thermal extremes and generate thermal refuges; however, the influence of groundwater on the thermal regime of coastal lagoons is rarely considered. Water temperature is a critical consideration in aquatic ecophysiology, as it exerts a significant degree of control on the metabolic functions of all organisms. A small number of riverine studies have considered the sensitivity of groundwater to climate change and the consequences this may involve, yet none have been identified that investigate this process as a driver of future change in coastal ecosystems, despite the basic principles being interchangeable. This study calls attention to this deficit in the literature and presents an exploratory investigation of these processes in BHH. In addition, methodological advancements and opportunities for the assessment of near-shore springs using drone-assisted TIR imagery and inexpensive temperature sensors are assessed and applied.

BHH is a lagoon feature where this area of research is particularly relevant because summertime water temperatures are nearing catastrophic thermal thresholds for several marine species of interest, including GIM and blue mussels. Previous biological and hydraulic research in the lagoon has been thorough, but hydrological characterisation has been limited. This thesis contributes novel data and interpretations on lagoon and watershed thermal dynamics, watershed and coastal hydrology, and groundwater thermal sensitivity to future climate change to local watershed groups and federal decision makers.

CHAPTER 2: METHODS

2.1 Study Period

Field work and data collection for this study occurred between June 2019 and November 2020 (i.e., the study period). Lagoon water temperatures typically peak in July and August in BHH, which reflects the period of greatest thermal stress for GIM. Contrast between groundwater and lagoon water temperatures is also greatest in July and August, which is favourable for TIR imaging, and this period is likely when groundwater cooling effects in the lagoon are most significant. Considering data density and study objectives, the period between July 23rd and August 26th, 2020 (i.e., the focussed study period) was selected for a more detailed assessment of groundwater discharge to BHH.

2.2 Site Description

2.2.1 Watershed Characterisation

2.2.1.1 Watershed Nomenclature & Hydrology

Prince Edward Island (Figure 1) is a crescent-shaped island located in the Maritimes Basin of Atlantic Canada (J. I. MacDougall et al., 1988; Rivera, 2014). PEI is approximately 230 km long, ranges in width (north to south) between approximately 6 and 50 km, has 1600 km of coastline, and has a total area of 5,750 km^2 (J. I. MacDougall et al., 1988; van de Poll, 1989). The greatest elevation of PEI is around 150 metres, and the landscape is defined by gently sloping hills (van de Poll, 1989).

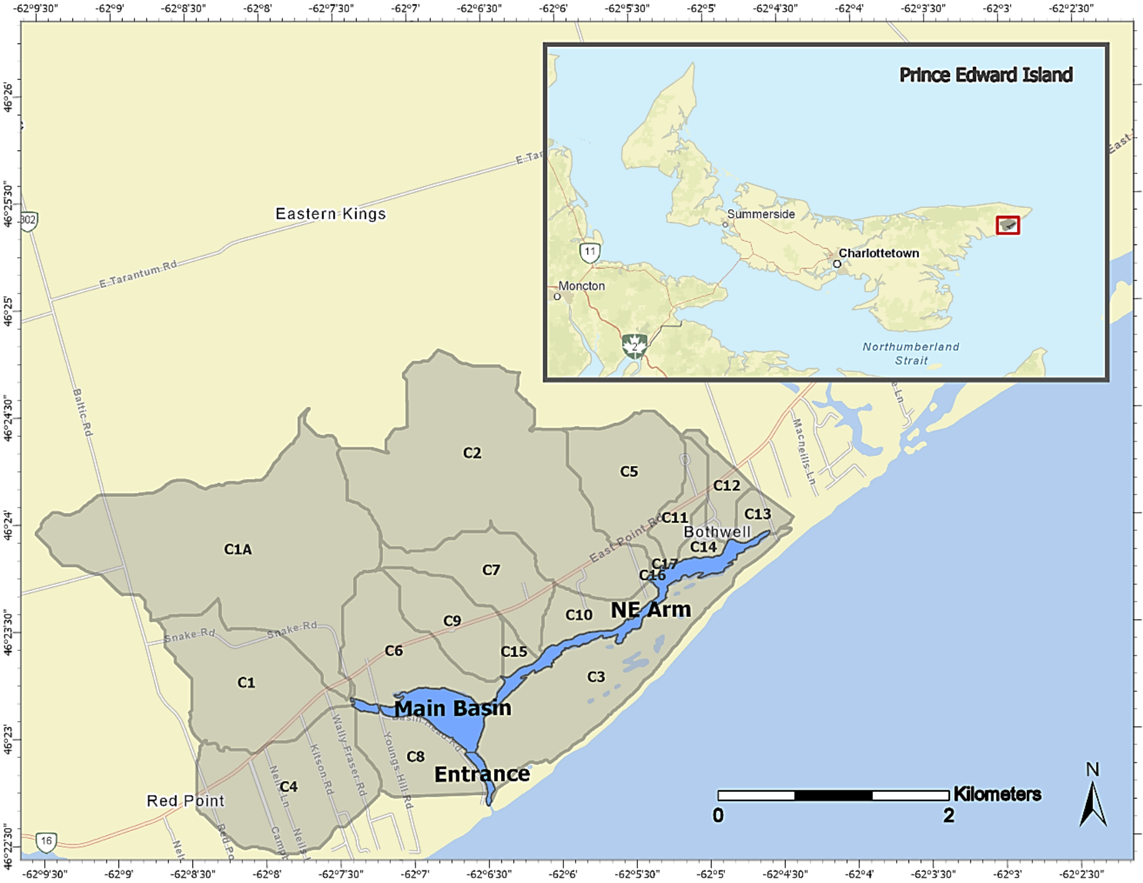

Figure 1. Location and delineation of the Kingsboro watershed and subcatchments in eastern Prince Edward Island. Map prepared in ArcGIS Pro (Version 2.3.3, 2018).

PEI is divided into three counties: Prince County, Queens County, and Kings County. The watershed of this study is located in Kingsboro, Eastern Kings, Kings County, PEI, and it drains into Basin Head Harbour (Figure 1). An overview of the geological history and nomenclature of the KW is included for reference in Appendix B, Section 2.

The total area of the watershed is approximately 14.6 km^2, and the topographically estimated area of each subcatchment (Figure 2) is outlined in Table 1. Groundwater boundaries have been shown to generally agree with watershed boundaries in the Maritimes Basin (Rivera, 2014). ArcGIS Pro (Version 2.3.3, 2018), satellite imagery (Esri et al., 2009+), elevation data (PEI Dept. Env., 2008), surficial soil data (PEI Dept. Env., 2002), the ArcHydro toolkit in ArcMap (Version 10.5.0.64.91, 2016), and field observations were used to delineate the catchments and drainage patterns of the KW (Figure 2). The topography of the watershed is available for reference in Figure 32, Appendix A.

Source: Esri, DigitalGlobe, GeoEye, Earthstar Geographics, CNES/Airbus DS, USDA, USGS, AeroGRID, IGN, and the GIS User Community

Figure 2. Topographically determined subcatchments of the KW watershed and their associated drainage networks. The total KW area is approximately 14.6 km^2, and each catchment is denoted by C1-C17, for a total of 18 subcatchments. Streams are designated by their respective subcatchments (e.g., Stream C1A). The major western streams (i.e., Streams C1, C1A, and C4) all converge in an intertidal salt marsh to form the largest stream discharge into Basin Head Harbour. Map prepared in ArcGIS Pro (Version 2.3.3, 2018).

Precipitation loading to the KW travels into BHH via groundwater-dominated streamflow, as well as diffuse and focussed groundwater discharge (Figure 2 and Figure 23, Appendix A). Diffuse groundwater discharge is defined herein as distributed freshwater discharge through benthic sediments, whereas focussed groundwater discharge to BHH arrives by means of springs and seeps, often associated with bedrock fracturing in PEI, in submerged, intertidal, or near-shore locations (<10 metres to shoreline).

Table 1. Nomenclature and areal extent of subcatchments in the Kingsboro watershed. Site maps describing the locations of each of these subcatchments are available for reference in Figure 2.

Subcatchment ID	C1[a]	C1A[a]	C2[a]	C3	C4[a]	C5[a]	C6	C7[a]	C8
Area (km^2)	1.2	3.2	2.8	1.4	1.3	0.9	0.8	0.7	0.6
Subcatchment ID	C9	C10	C11	C12	C13	C14	C15	C16	C17
Area (km^2)	0.5	0.3	0.2	0.2	0.15	0.10	0.08	0.009	0.001

[a] *These subcatchments have stream channel flow for at least most of the year.*

Approximately six small first- and second-order streams deliver flow to the harbour. By extension, there are twelve relatively small subcatchments (total area ≈ 4 km^2) without stream flow channels or that have small ephemeral or historical stream channels. It is suspected that some historical streams, as identified through soil surveys (Figure 34, Appendix A), have disappeared as the result of anthropogenic influences on the hydrologic function of the watershed (e.g., roadway construction, deforestation, and agriculture). The largest stream system converges and discharges into a riparian zone to the northwest of the harbour (Figure 2). Streams are referred to by the subcatchment in which they are located (e.g., the stream in subcatchment C2 is referred to as Stream C2).

Brandon (1966) proposed that baseflow maintains most streamflow during the dry and the winter seasons of PEI; albeit some streams (e.g., Stream C7 and C4) have been observed to run dry seasonally in the KW. Approximately 60-70% of PEI annual surface flow is groundwater-sourced, and groundwater contributes nearly 100% of surface flow throughout the summer (V. S. Benson et al., 2007; DELJ, 2013). It has been estimated that 80% of groundwater is sourced from within 22 metres of the ground surface in the Wilmot River watershed in western PEI, with residence times ranging from days to less than four years (Wilmot, PEI; Y. Jiang, Somers, & Paradis, 2007). In a study in Winter River, PEI, Francis (1989) suggested that streamflow was mainly derived from bedrock as well as the overlying till. Sandy tills and fractures across PEI often serve as preferential flow paths for infiltration and conduits to streams and coastlines (Francis, 1989; Rivera, 2014).

The most recent land use inventory of the study site (PEI Dept. Env., 2000a, 2000b) revealed that the primary land uses in the KW are agriculture, forestry, and wetlands (Table 2). In the year 2000, 2% of the watershed was paved, 34% was forested, 11.5% was wetland, and the primary crops were grain (22.3% coverage) and potatoes (13.5% coverage; PEI Dept. Env., 2000a). The spatial extent of various land uses throughout the KW for the year 2000 are presented in Figure 35, Appendix A. Given that there have been changes in land-use over the past 20 years, this level of detail may be unreliable.

Table 2. Land uses within the Kingsboro watershed presented as percent coverage. Data extracted from records of the PEI Dept. Env. (2000a, 2000b).

Land Use	Coverage (%)
Agriculture	41.4%
Forestry	31.1%
Wetland	11.5%
Non-Evident	8.2%
Residential	5.4%
Transportation	1.8%
Industrial	0.4%
Institutional	0.1%
Commercial	0.1%

2.2.1.2 Surficial Soil Characterisation

The primary surficial soils in the KW are clay-sand (Crowl, 1969c) to sand phase till (Prest, 1973b). The thickness of till appears to be highly variable across PEI, as observations commonly range from 0 to 8.5 metres (Brandon, 1966; Carr, 1969; Crowl, 1969a; Francis, 1989; Government of PEI, 2019; Joostema, 2015; J. I. MacDougall et al., 1988), with extreme observations as deep as 20 metres (Crowl, 1969a). A piezometer installed within the KW by Dalhousie (DalWell) encountered bedrock after approximately 4.6 metres, and historical well records in the region suggest depths ranging from 0 to 6.2 metres (Government of PEI, 2019; Joostema, 2015).

Francis (1989) conducted soil particle size analysis on 26 ground moraine samples from Winter Basin, PEI. By conducting a simple non-parametric analysis on their data, the median mass percent of gravel, sand, silt, and clay were calculated as approximately 24%, 61%, 12%, and 3%, respectively. Characterisation of sand phase till near Summerside, PEI, by Tibbet (2015) suggests comparable values, with higher estimations for clay and silt content at their site. In general, the mass percent of sand-sized grains dominated the PEI ground moraine tested. There is notable heterogeneity identified in the surficial deposits of PEI, but these data may reasonably be used to estimate the composition of the ground moraine in the KW for modelling purposes, in the absence of site-specific estimates, because of comparable parent material and depositional history (Carr, 1969).

The Charlottetown soil series, which has been characterised as fine sandy loam, or very fine sandy loam, can be assumed as generally representative of KW surficial soils, as it covers approximately 74% of the area (Figure 34, Appendix A). The Charlottetown soil series is well to moderately-well drained, forms slopes between 0.5 and 5%, has adequate to rapid drainage, and is moderately coarse textured (J. I. MacDougall et al., 1988). The generally anticipated slopes for the Charlottetown series are consistent with the gentle 2-5% slopes observed predominantly throughout the KW (Table 3; PEI Dept. Env., 2002). Other minor soil series are also found within the watershed (e.g., Winsloe, Alberry, Malpeque, Wood Island), as well as wetland areas that contain muck and peat features (Figure 34, Appendix A; PEI Dept. Env., 2002).

Table 3. The slope phases within the Kingsboro watershed and their relative areal coverage. The spatial topographical data for the Kingsboro watershed is available in Figure 32, Appendix A.

Slope Phase (%)	0.5	1	3.5	7	10	12	19.5	22.5	37.5	NA
Coverage (%)	1.5	4.6	65.6	11.4	2.7	1.8	1.4	0.1	0.3	10.5

J. I. MacDougall et al. (1988) estimated the saturated hydraulic conductivity of the Charlottetown soil series above 55 cm as 0.77 to 2.8 m/day and under 55 cm as 0.1 to 0.7 m/day. Similarly, Carter (1987) estimated the hydraulic conductivity above 8 cm as 2.82 m/day and from 8-32 cm as 0.1 to 0.58 m/day. Separately in Winter Basin, PEI, Francis (1989) used grain size distribution to estimate the hydraulic conductivities of ground moraine comparable to those found in the KW. Francis (1989) utilised the Kozeny-Carman empirical equation to estimate the hydraulic conductivity of clay-sand or clay-silt phase till and sand phase till as 0.17 m/day (n=11) and 0.28 m/day (n=15), respectively. A slug test was also conducted in the clay or clay-silt phase till of Winter Basin, which yielded a conductivity estimate of 0.047 m/day.

Macroporosity influences the hydraulic conductivity of the soil, as well as the range of estimated soil porosity. Therefore, it is appropriate to consider an upper macroporous root zone, assumed here as descending to a depth of 0.5 metres based on detailed core logs collected by Joostema (2015). Based on the available literature data on the Charlottetown soil series, a till porosity representative of the macroporous zone may be ~50% (Carter, 1987; J. I. MacDougall & Veer, 1981), whereas the porosity of the till below 0.5 metres may be closer to ~30% (Francis, 1989; Heath, 1983; J. I. MacDougall & Veer, 1981).

2.2.1.3 Bedrock Characterisation

Weakly consolidated, very fine to coarse sandstones are expected to dominate the uppermost layers of bedrock in the KW, with sparse occurrences of mudstone, conglomerate, and/or breccia (Brandon, 1966; Crowl, 1969a; Francis, 1989; van de Poll, 1989). In general, the strata beneath the KW have been interpreted as flat to gently sloping with a high occurrence of crossbedding that causes discontinuities in the lenticular soil layers (Brandon, 1966; Carr, 1969; Crowl, 1969a; van de Poll, 1989). Francis (1989) suggested that PEI bedrock is likely to be 80-85% sandstone, with the remainder being composed mainly of mudstone. Carr (1969) suggests that interbedded sandstone and mudstone may be considered as a single hydraulic unit due to extensive vertical fracturing[2]. Furthermore, Carr (1969) proposed that PEI strata display little variation in their mineralogical compositions, have similar dispositional mechanisms, and have comparable post-depositional stress history; thus, the findings of hydrogeological assessments conducted at one site can be applied elsewhere in PEI without introducing significant error. Although this hypothesis may be limited at a local scale due to the

---

[2] This thesis adopts the terminology used by Francis (1989), where fractures refer to joints, bedding planes separations, faults, cracks, and cavities.

heterogeneity of tills, fracture connectivity, and mudstone distributions, data from surrogate sites on PEI were used when local data were not available.

There is a long history of inquiry into the subsurface processes of PEI, much of which has focussed on the fracturing of PEI aquifers. All sedimentary rocks contain fractures, but the density, interconnectedness, and distribution of these formations, on which hydraulic conductivity depends, may be highly variable (Francis, 1989). Fractures often serve as preferential flow paths in the subsurface, but are typically a small fraction of the total porosity of PEI aquifers, and the relative significance of fracture flow increases with decreasing capacity for intergranular transport (Francis, 1989). Rapid recharge and lateral flow are facilitated by the interconnected vertical and horizontal fractures in the bedrock and overburden (e.g., Carr, 1969; Francis, 1989; Zebarth et al., 2015). Fractures are found in both PEI sandstone and mudstone strata, and although they both have appreciable porosity, sandstones were noted to release water more rapidly (Carr, 1969; Francis, 1989).

Past hydraulic tests on PEI may be used to estimate the subsurface hydraulic properties of the KW. Carr (1969) conducted pumping tests on thirty-two municipal wells in PEI and used them to calculate an average hydraulic conductivity of 1.6 m/day for PEI bedrock. Carr (1969) subsequently conducted falling head permeameter tests on thirteen bedrock cores taken from beneath the water table and calculated a maximum intergranular hydraulic conductivity of 0.1 m/day, which confirmed that most water flowed through the fracture networks of the *in-situ* bedrock. Francis (1989) noted bulk hydraulic conductivities of fractured PEI bedrocks between 10^{-3} to 10^{-7} m/s, anisotropy ratios between 0.1 to 0.001, that horizontal bedding plane fractures were the most important fluid conduits, and that fracturing, hydraulic conductivity, and specific storage declined with depth in Winter Basin, PEI. Francis (1989) measured an approximate bulk hydraulic conductivity for the upper 25 metres of approximately 125 m/day. Conversely, they measured bulk conductivities of approximately 4.3 m/day from 25 to 150 metres depth. Specific storage declined much more modestly over the same depth ranges, from approximately 3.4×10^{-5} to 2×10^{-5} m^{-1}. During their pumping tests, Francis (1989) observed that the early data matched the Theis curve (likely a result of the fractures emptying), and the later data behaved as a leaky aquifer (likely due to the media beginning to replenish the depleted fractures). Similarly in Borden, PEI, Carr (1971) noted that bedrock aquifers often existed under semi-confinement and also suggested that their layers were not homogenous, nor were they of uniform thickness. Regardless, they were able to apply idealised confined theory in their subsurface analysis (Carr, 1971). Estimates of hydraulic conductivity at their site ranged from 0.1-0.4 m/day, porosities ranged from 14-27%, and specific storage was approximately 3×10^{-6} m^{-1} (Carr, 1971).

Additional characteristics of the KW subsurface were interpreted from various public and private well logs. The logs of nine historical wells within the KW were on record (Figure 36, Appendix A; Government of PEI, 2019), but their detail and quality was limited. These well logs suggested a surficial soil thickness between 0 and 5.2 metres, underlain by layers of sandstone, mudstone, and various water bearing zones (Government of PEI, 2019). Fracturing is identified in some of the historical well logs and there are indications of discontinuous geological confining units (Government of PEI, 2019). Three higher quality core logs were identified in Souris that may be used in conjunction with other literature values to speculate the thickness of a highly fractured zone, the stratigraphy, and the water bearing mechanisms (Joostema, 2015). These commercial well logs suggest 0.5 metres of organic-rich topsoil, underlain by 4-6.2 metres of till, proceeded by layers of sandstone and mudstone (Joostema, 2015). Discrete water bearing zones were identified over the entire depth of the wells (i.e., 94.5 m; Joostema, 2015), which may indicate the channeling of groundwater through vertical and bedding plane fractures. Static water levels of wells in the Souris and Kingsboro regions suggest some level of aquifer confinement (Government of PEI, 2019; Joostema, 2015).

2.2.1.4 Present Climate & Weather

Prince Edward Island has a humid continental climate influenced by continental and oceanic air masses (Rivera, 2014). This coastal region is often characterised by high humidity (>85%), sudden temperature changes, and regular freeze-thaw cycles (Rivera, 2014). Historical annual precipitation rates in PEI ranged between 1046 to 1241 mm/yr, and mean monthly air temperatures ranged from -7.9 to 18.6°C, as calculated by Rivera et al. (2014) using data from eight Environment and Climate Change Canada (ECCC) stations. Approximately 20-30% of precipitation falls as snow over the winter, and the remainder arrives as rain (Jiang et al., 2004; Rivera, 2014). Complete annual ECCC historical data exist for the KW between 2001 and 2005 only (Station ID 30618; ECCC, 2019a). These five years of data suggest a mean annual rainfall of 1219 mm/yr and a mean annual air temperature of 6°C (Station ID 30618; ECCC, 2019a). Monthly averages and harmonic trend estimates over this five-year period are included to present the patterns of precipitation and air temperature that may be expected locally throughout the year in the KW (Figure 3). A remote Onset HOBO® weather station was installed at the site (Figure 7) for the duration of the study period.

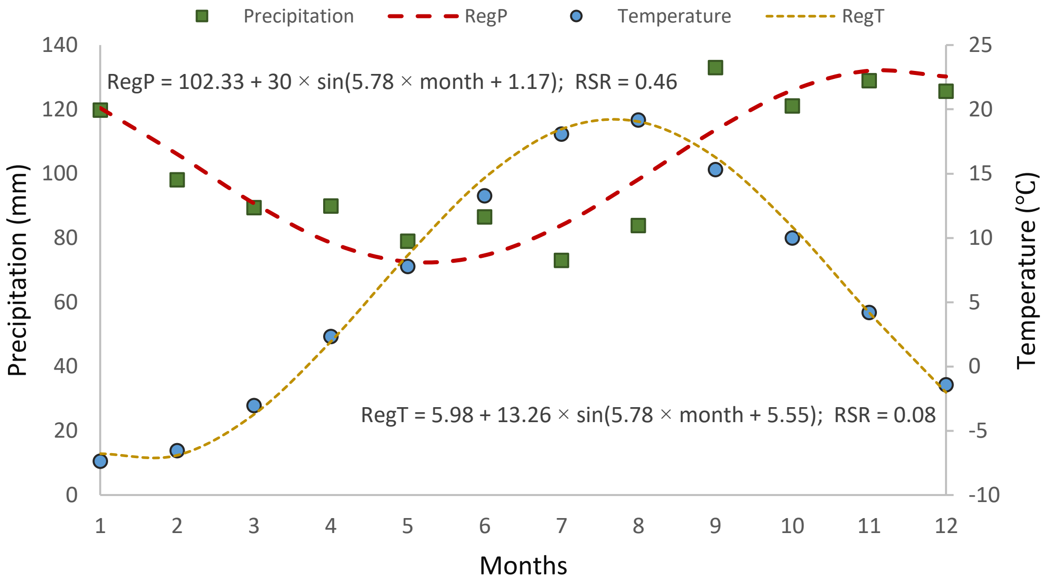

Figure 3. Average monthly precipitation and temperature data for the Kingsboro weather station from 2001-2005 (Station ID 30618, ECCC, 2019a). Sinusoidal curves were fit using an error minimisation regression in Microsoft Excel based on the RSR. RegT = fitted harmonic trend of station temperature data and RegP = fitted harmonic trend of station precipitation data. P = precipitation, T = temperature, month = number between 1 and 12, and Reg = regression (harmonic). Refer to the list of abbreviations or Appendix D for the definition of RSR.

The local and regional weather of PEI is affected by the regional water bodies, orographic boundaries, and seasonal trends that make the transposition of alternative weather station data questionable due to the potential for seasonally variable connectedness between locations. In other words, the weather and climate controls of PEI are complex, and there may be reason to suspect that the relationships between climate variables of different stations may not be stable throughout the year (Nav Canada, 2000). Thus, it is likely more suitable to use site-specific data where it exists as other locations may not be representative. This assessment is supported by observed disagreement of 2004 precipitation data between the ECCC Kingsboro station (Station ID 30618; ECCC, 2019a) and the two closest ECCC stations: East Point (Station ID 7177; ECCC, 2021a) and St. Peter's (Station ID 41903; ECCC, 2021b). Approximate annual rainfalls were 935, 808, and 1035 mm/yr for Kingsboro, East Point, and St. Peter's, respectively. In addition, the temporal patterns and magnitudes were not consistent. This may demonstrate the significance of local weather variability, as precipitation estimates vary by upwards of 200 mm, despite being within 50 km of one another.

2.2.1.5 Future Climate

The Intergovernmental Panel on Climate Change (IPCC) stipulated that they are 95% confident that anthropogenic contributions are driving the majority of observed climate warming (IPCC, 2014). Thermal trends are expected to enhance the frequency and intensity of extreme precipitation in many regions (IPCC, 2014), which will likely impact groundwater quantity and quality and aquatic habitat suitability. Changes in precipitation and air temperature are expected to affect groundwater temperature over multi-decadal time scales (Bense & Kurylyk, 2017). In fact, Mareschal and Beltrami (1992) have reconstructed historical changes in air temperature by inverting measured borehole temperature profiles, suggesting that Eastern Canada has already experienced a 1 to 2℃ increase in temperature over the past 1-2 centuries.

Uncertainty arises in climate models from not knowing future emissions and related atmospheric greenhouse gas concentrations, a limited understanding of climate physics, and climate system modelling limitations (ECCC, 2018b). To account for this uncertainty, an array of possible future scenarios of greenhouse gas emissions were developed by the IPCC, which they named representative concentration pathways (RCP). The convention proposed by the Canadian Government for future climate modelling is to assess RCP2.6, RCP4.5, and RCP8.5 for an ensemble of climate scenarios, where the numbers (i.e., 2.6, 4.5, and 8.5) indicate the radiative forcing (W m^{-2}) by the year 2100. These RCPs project end-century median global air temperature to increase by approximately 0-2℃, 1-3℃, and 2.9-5.6℃, respectively, relative to 2005 (ECCC, 2018b). Simulations with magnitudes between RCP4.5 and RCP8.5 appear most probable currently, as RCP2.6 requires significant international mitigative action to occur rapidly.

Two statistically downscaled global climate models, shortlisted for Charlottetown by Warner (2016) from the Coupled Model Intercomparison Project Phase 5 ensemble (i.e., CNRM-CM5 and MRI-CGCM3), were used to project potential future conditions for the study site (ECCC, 2018a; Voldoire et al., 2013; Yukimoto et al., 2012). RCP4.5 and RCP8.5 future simulations were tested for each model. These models have been downscaled from ~100 km to a ~10 km grid resolution by using the second version of bias correction/constructed analogues with quantile mapping (ECCC, 2019b). It is understood that the selection of a future rainfall and air temperature scenario will bias modelling results and will only represent the selected projections. However, this approach was taken to conserve resources without compromising the modelling objectives. The IPCC 6th Assessment Report and associated climate model ensemble were released coincident with this thesis submission and represent the newest available future climate projections. Alternative and more expansive model data may be considered in future work.

2.2.2 Lagoon Characterisation

2.2.2.1 Lagoon Nomenclature & Geometry

The DFO oversaw the collection of bathymetry data for BHH in 2017 (Figure 4; Guyondet, 2019). BHH is a lagoon that is approximately 0.6 km^2 in size, and it is divided into three zones based on distinguishing characteristics (Figure 1 and Figure 4): the NE Arm (0.3 km^2) is a reach, typically less than 1 metre deep, that runs parallel to the shore and is where GIM is found; the main basin (0.3 km^2) is typically under three metres deep, receives the largest stream inputs to BHH in its northwestern corner, and is armoured with stone along the western shore; and the entrance (0.03 km^2) is the manmade and maintained outlet of the harbour to the ocean that periodically gets impeded by sediment. A primary challenge in characterising this coastal environment is the frequent redistribution of sediment, so the present accuracy of the 2017 bathymetry data may be limited.

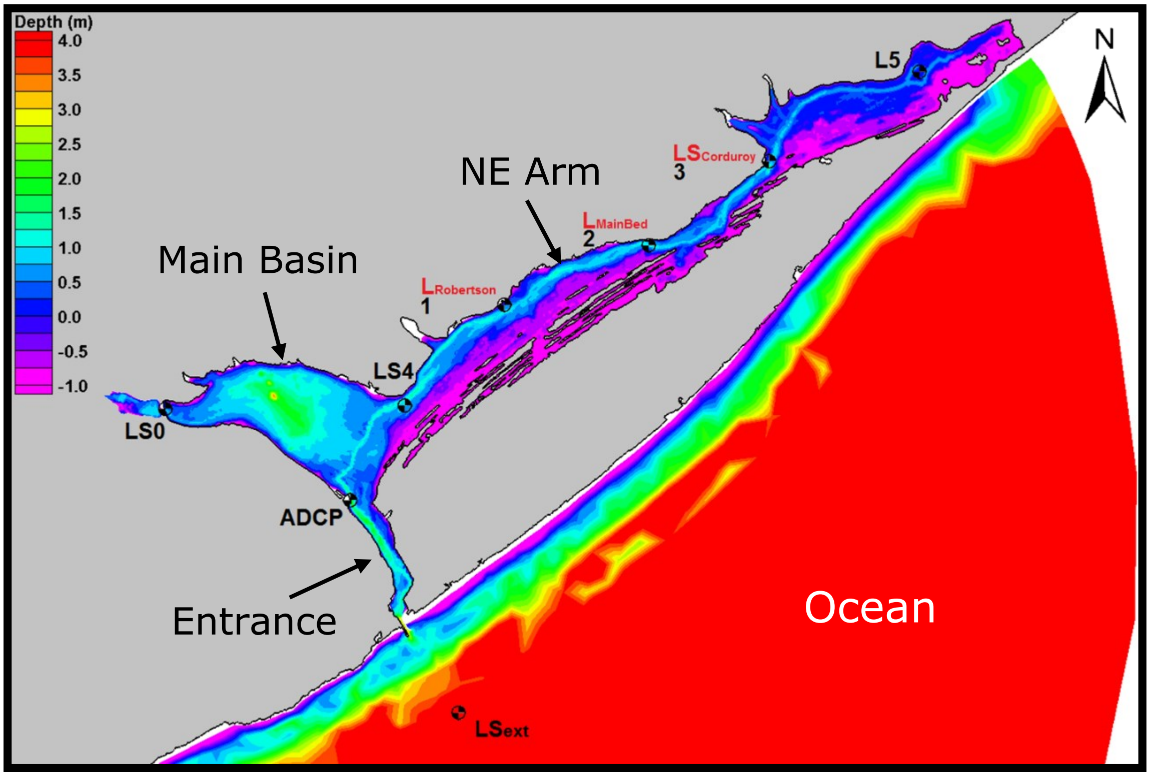

Figure 4. Heat map of 2017 bathymetry for Basin Head Harbour and DFO sensor locations. L = water level sensor; S = salinity sensor; ADCP = acoustic Doppler current profiler. The grey areas represent land mass, whereas the coloured zones are water (depth). Figure from Guyondet (2019), reproduced with the permission of the DFO.

2.2.2.2 Lagoon Hydrodynamics & Morphodynamics

Developing a general understanding of BHH hydraulic processes is important for the interpretation of field data and observations. Hydrodynamics affect both the biotic and abiotic characteristics of BHH, which makes them relevant to the conservation of GIM. Figure 5 is a modified version of the Haines (2006) conceptual model of the factors influencing coastal lagoon hydrodynamics, with some additional considerations that may be relevant for the smaller scale processes considered in this study. The interdependency of numerous variables that vary in time and space is in part what makes coastal environments so challenging and compelling to study.

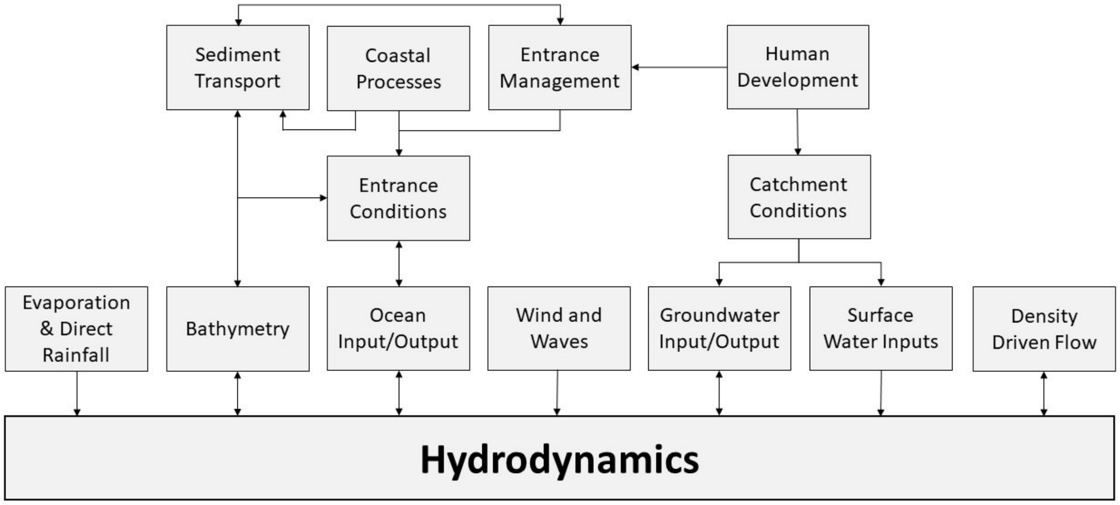

Figure 5. Conceptual diagram of the hydrodynamic elements affecting Basin Head Harbour. Many of the identified factors are interdependent and may have complex feedback loops with the hydrodynamics of the lagoon. Figure modified from Haines (2006).

Past and future human developments may influence the hydrodynamics and morphodynamics of BHH (e.g., Figure 5 and Figure 41, Appendix B, Section 2), and the water quantity and quality of BHH are certainly impacted by various human activities (e.g., agricultural lands, transport infrastructure, artificial channelisation, and channel dredging). Sediment transport and sediment mobility also play important roles in defining the geometry of the lagoon, as well as the entrance conditions that control ocean inputs and outputs (Figure 5). Large amounts of sediment regularly get displaced within the lagoon, and periodic dredging is required at the entrance of BHH to maintain ocean access. Longshore sediment transport, onshore-offshore processes, and/or bank erosion may be responsible for the periodic impedance of the entrance (Haines, 2006; Prest, 1973a). Regardless of the cause, different hydrodynamic and thermodynamic regimes may be expected when the ocean inlet is open, partly blocked, or entirely blocked (Haines, 2006). Slower flushing rates may lead to increases in water temperature, by enabling greater absorption of solar radiation in the time it takes for water to be replaced by marine or freshwater sources. Thus, the significance of freshwater inputs to mixing dynamics and water quality may be expected to vary with the entrance conditions and seasonal regimes of BHH.

Several additional factors may be expected to influence the hydrodynamics of BHH, which may in turn affect the bathymetry, groundwater discharge, and entrance conditions of the lagoon. Because of the shallow bathymetry of many lagoons, density driven flow is likely only important when considering the saltwater-freshwater interface of the coastal aquifer and in the local mixing zones of freshwater discharges. The effect of evaporation and direct rainfall on the hydrodynamics of BHH is likely minimal, as it is normally well connected to the ocean and the climate is humid continental. Finally, future climate change has the potential to indirectly or directly affect all of the hydrodynamic and morphodynamic controls discussed in this section (Haines, 2006), but this relationship is complex and largely beyond the scope of this thesis.

The DFO calibrated a hydrodynamic model for BHH using hydrodynamic, bathymetric (Figure 4), and water quality data collected in 2017 (Guyondet, 2019). The water level within the lagoon was largely dominated by the tidal signal, although the timing and amplitude of the tidal signal were attenuated by the entrance to the harbour. The greatest velocities were modelled in the entrance channel and the lower and middle NE Arm, and the lowest velocities were observed in the upper NE Arm and northwest extremities of the main basin (DFO, 2009; Guyondet, 2019). The average flushing time of the lagoon was modelled as 24.5 hours using the tidal prism method (DFO, 2009); however, the modelled flushing time of the NE Arm upper reach may be greater than three days (Figure 6; Guyondet, 2019). The model’s connection to the ocean was unobstructed, so it is possible that the flushing rates are periodically longer than estimated (DFO, 2009; Haines, 2006).

2.2.2.3 Lagoon Heat Budget

A conceptual model of the heat fluxes associated with BHH is presented in Figure 6.

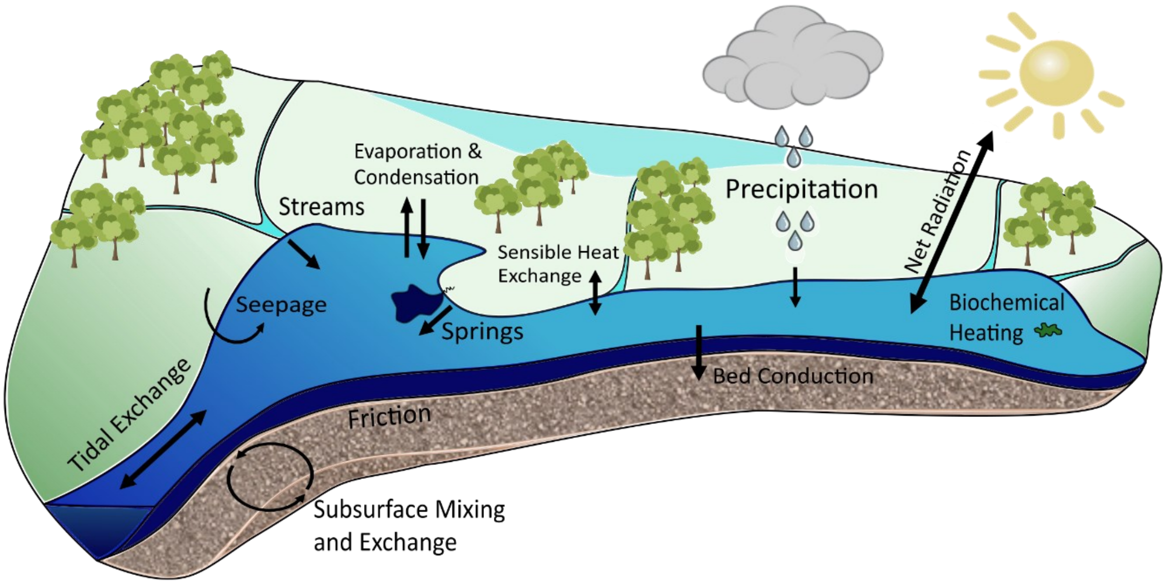

Figure 6. Conceptual model of the various heat fluxes associated with the Basin Head lagoon. Components were identified from Ji (2017) and Rodríguez-Rodríguez and Moreno-Ostos (2006).

Lagoon water temperature may theoretically be calculated by summing the energy fluxes shown in Figure 6, as described in more detail in other work (e.g., Ji, 2017; Rodríguez-Rodríguez & Moreno-Ostos, 2006). Net solar radiation, latent heat of evaporation, and sensible heat transfer to the atmosphere are typically the primary drivers of water temperature, whereas biochemical reactions, bed conduction, and friction are normally negligible (Ji, 2017; Rodríguez-Rodríguez & Moreno-Ostos, 2006). Only five components of the lagoon heat budget were estimated in this study due to data limitations. For relative comparisons, these components were assessed over the 35-day focussed study period in terms of net heat (Joules). Net radiation may be broken into three components:

$$E_{rad} = E_{sh} + E_{la} - E_{le} \tag{2}$$

where	E_{rad}	is the net radiation to and from the lagoon (W m^{-2})
	E_{sh}	is the downward shortwave radiation absorbed by the lagoon (W m^{-2})
	E_{la}	is the downward longwave radiation absorbed by the lagoon (W m^{-2})
	E_{le}	is the longwave radiation emitted from the lagoon (W m^{-2})

Downward longwave radiation was not quantified, whereas downward shortwave radiation was measured and longwave radiation emitted from the lagoon was estimated via (Rodríguez-Rodríguez & Moreno-Ostos, 2006):

$$E_{le} = \sigma(T_{0.5})^4\varepsilon_w \tag{3}$$

where	σ	is the Stefan-Boltzmann constant (5.57×10^{-8} W m^{-2} K^{-4})
	$T_{0.5}$	is the absolute lagoon water temperature at half metre depth (K)
	ε_w	is the emissivity of water (assumed as 0.96)

The net advective heat contributions of the springs, streams, and rainfall were estimated at the lagoon scale using an equation developed for the advective input to a finite segment of a stream or streambed (e.g., Caissie & Luce, 2017; Kurylyk et al., 2016):

$$E_{adv} = \sum_{i=1}^{N} Q_{in}(T_{in} - T_{lagoon})c_l\,\rho_l \tag{4}$$

where	E_{adv}	is the net advective heat to the lagoon (J)
	Q_{in}	is the volume of water discharged to the lagoon (m^3)
	T_{lagoon}	is the representative temperature of the lagoon (°C)
	T_{in}	is the temperature of the water discharged to the lagoon (°C)
	c_l	is the specific heat capacity of liquid water (J kg^{-1}°C^{-1})
	ρ_l	is the density of liquid water (kg m^{-3})

Although this equation may be limited conceptually in this application, as the lagoon likely behaves closer to a terminal for freshwater inputs, this will ultimately be of little importance because the results will only be used for relative comparisons. The remaining heat budget components of Figure 6 were not computed in this study.

2.3 Instrumentation & Remote Sensing

An Onset HOBO® weather station, which collected precipitation, downward shortwave radiation, air temperature, relative humidity, and wind speed data, and a piezometer were installed near the centre of the lagoon (device locations shown in Figure 7). Additional climate data were available from nearby ECCC weather stations. In addition, numerous temperature, conductivity, and pressure sensors were deployed throughout the lagoon and watershed (sensor locations shown in Figure 7), and preliminary drone investigations began in summer 2019. The following section outlines the equipment deployed during the summers of 2019 and 2020 that were used in the final analysis.

The outlets of the four largest tributaries were instrumented with temperature sensors in 2019 and 2020. Temperature sensors were installed into the outlet aperture of a single intertidal spring in 2019 and three springs in 2020. Three pairs of temperature sensors, each of which had one sensor located at the lagoon surface and the other at the channel bottom, were deployed in 2019, and two were installed in 2020. These temperature sensors were all Onset HOBO® MX2203 TidbiTs (±0.2°C accuracy and 0.01°C resolution) configured to log at a 15-minute interval. Sensor locations are shown in Figure 7 for reference.

Electrical conductivity loggers were installed in the lagoon (Onset HOBO® U24-002-C) and major tributary (Stream C1A; Onset HOBO® U24-001-C) in 2019 to monitor stream outlet salinisation and to estimate representative conductivities for both fresh and lagoon waters (sensor locations shown in Figure 7). These conductivity data were supplemented in 2020 with the installation of stage-temperature-conductivity loggers (Solinst Levelogger® 5 LTC) in the DalWell, the lagoon, and two of the gauged intertidal springs (i.e., Spring A and C). Discrete measurements of conductivity and temperature were taken for the other two gauged springs using a handheld device (EC400S Portable Conductivity/TDS/Salinity/Resistivity Meter) to interpret the proportion of discharge attributable to recirculated lagoon water at the time of gauging. This same handheld device and a YSI Multiparameter Sonde were used for rapid field investigations throughout the lagoon and associated wetlands. The final LTC logger was installed near the ocean entrance to the lagoon and offered an estimate of tidal stage over the study period, which was critical for the interpretation of data collected within the lagoon.

Figure 7. Map outlining the locations of temperature loggers (Onset HOBO® MX2203 TidbiT), conductivity loggers (Onset HOBO® U24-001/2-C), pressure transducers (Onset HOBO® U20-001-01/04), pressure-temperature-conductivity loggers (Solinst Levelogger 5 LTC), the Dalhousie piezometer (Well), and Onset HOBO® weather station within the Kingsboro watershed for their respective sampling periods during 2019-2020. Sensors with short-term deployments (<2 weeks) were not included in this figure. Near-shore springs and stream locations are indicated. Map prepared in ArcGIS Pro (Version 2.3.3, 2018).

Thermal infrared images were taken of the lagoon and cold-water springs at various tidal stages throughout the summer of 2019 and 2020. This study used a Matrice 210 RTK v2 aerial drone, equipped with a 13 mm non-radiometric DJI ZENMUSE™ XT2 TIR camera with FLIR technologies (XT2; DJI, 2018). Real-time kinetic processing is used for drone navigation, as well as image geotagging, and the relative positional accuracy of the images relative to the base station are expected to be highly accurate (<5 cm) even without using ground control points (Kalacska et al., 2020). The XT2 has a 45° × 37° field of view, 640 × 512 resolution, 8-bit colour pallet (i.e., 256 distinct colours), spectral band between 7.5

and 13.5 μm, a sensor sensitive range between -25 and 135°C (*High Gain Mode*), and an thermal accuracy of ±5 to 10°C (DJI, 2018). The XT2 has a sensor width of 8.704 mm, sensor height of 10.88 mm, and focal length of 13 mm (Personal email communication with DJI, February 22nd, 2020). Stationary nadir images were generally captured from a height of approximately 60 metres above mean sea level in R-JPEG format.

The accuracy of the temperature values embedded in the thermal imagery were not considered reliable due to the internal drift of the device (DJI ZENMUSE™ XT2), lack of radiometric correction, and large observed disagreement in temperature values between frames. However, it was assumed that the relative temperature differences in each frame were sufficiently precise for the consistent definition of plume geometry, given the reproduceable ability of the XT2 to identify surficial thermal anomalies that were confirmed with *in-situ* temperature measurements. In lieu of the appropriate equipment for developing a per-pixel corrections matrix for the XT2, only the central portion of each image was used for analysis, as recommended by J. Kelly et al. (2019). Cropping to the centre of the image should also reduce the degree of spatial distortion; therefore, it was assumed during the graphical area analysis that each pixel represented the same area (i.e., spatial distortion is negligible).

2.4 Streamflow Assessment

Stream stage and flow data were recorded within the KW between June 2019 and August 2020. Total streamflow estimates were developed for the focussed study period over which indirect and direct groundwater delivered to the lagoon were compared. The timing and location of streamflow measurements were largely dictated by travel logistics and site access, respectively. As a result, stream gauging was primarily done during the summer and fall, which provides a limited flow range with which stage-discharge relationships could be developed. Thus, an indirect estimate of peak channel flow was used to better constrain the upper range of the stage-discharge relationships, as proposed by Rantz et al. (1982a).

2.4.1 Stage Measurement

Pressure transducers (Onset HOBO® U20-001-04; ± 0.3 cm accuracy, and 0.14 cm resolution) were used to monitor stage at a 15-minute interval in the stilling wells of the four largest tributaries to BHH (i.e., Stream C1, C1A, C2 and C5; Figure 33, Appendix A). Figure 8 portrays conceptual diagrams of the two stilling well designs.

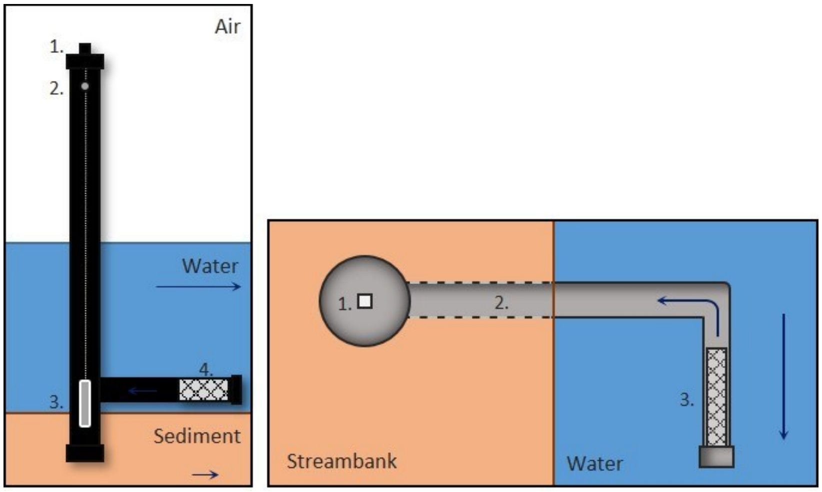

Figure 8. Conceptual diagrams of stilling wells installed in the Kingsboro watershed. (Left) Side view of custom in-stream ABS Dalhousie stilling well (Stream C1, C2, and C5): (1) well cap, (2) vent hole, (3) pressure transducer, and (4) screened section of intake pipe and filter sock. (Right) Top view of DFO PVC stilling well (Stream C1A): (1) well cap, (2) lateral intake pipe, and (3) screened section of intake pipe.

Manual stage measurements were made semi-regularly during site visits for manual calibration and data redundancy purposes. Air pressure data from nearby ECCC weather stations (i.e., Station IDs 7177 and 41903; ECCC, 2021b, 2021a) were used to correct stilling well data for atmospheric pressure at an hourly resolution. It was assumed that drawdown and pileup effects were negligible in the stilling wells throughout this study (Rantz et al., 1982a). When no stage record was available for a gauged stream, measured discharges were instead correlated with the stage record of a nearby stream instead.

2.4.2 Direct Gauge Measurement

Discharge was periodically measured in Stream C1, C1A, C2, C5, and C7 (Figure 33, Appendix A). The conventional current-meter midsection method and a 0.6-depth measurement of velocity were used to gauge flow at each stilling well (Rantz et al., 1982a; Turnipseed & Sauer, 2010). Flow and depth measurements were taken using a Sontek FlowTracker2® and remained within the operational range of the device (Turnipseed & Sauer, 2010). Measurement uncertainty associated with velocity-area discharge quantification is typically between 2-19% (Mcmillan et al., 2012). Timed volumetric measurements of hanging culvert discharges were occasionally taken at Stream C5 and exclusively taken at Stream C7, with uncertainties estimated ranging between 8-43%. Further details on these fundamental methods and gauging best practices can be found in Rantz et al. (1982a), Stone et al. (2012), and Turnipseed & Sauer (2010).

2.4.3 Indirect Gauge Measurement

Indirect measurement techniques constrain stage-discharge relationships by applying hydraulic and energy conservation theory to model inadequately captured discharge regimes of channels (Domeneghetti et al., 2012; Rantz et al., 1982a). High streamflow events were not captured during field expeditions due to time constraints, budgetary limitations, and conflicting field objectives, whereas low streamflow events are thought to have been captured effectively. The uniform flow Slope-Area Method was applied in this study to estimate peak channel discharge based on Manning's equation (Bedient et al., 2013; Rantz et al., 1982a):

$$V = \frac{1}{n} R^{\frac{2}{3}} \sqrt{S_E} \tag{5}$$

where	V	is channel velocity (m/s)
	R	is hydraulic radius (m)
	S_E	is the energy slope (m/m)
	n	is the Manning's roughness coefficient

The estimated discharges in this study did not include flow through floodplains, as their extents were more difficult to estimate. The U.S. Geological Survey guidelines were followed for the selection of Manning roughness coefficients for stream channels (Arcement & Schneider, 1989). This procedure was based primarily on work conducted by Cowan (1956) and Aldridge and Garrett (1973). Base Manning's roughness coefficients were adopted from Chow (1959) and Benson and Dalrymple (1967). Cowan (1956) proposed the following formulation to calculate Manning's roughness coefficient for a natural stream:

$$n = (n_b + n_1 + n_2 + n_3 + n_4)m \tag{6}$$

where	n_b	is the base value of n for a straight, uniform, smooth channel of natural materials
	n_1	is the correction factor for surface irregularities
	n_2	is the correction factor for variation in cross-section shape and size
	n_3	is the correction factor for obstructions
	n_4	is the correction factor for vegetation and flow conditions
	m	is the correction factor for channel meandering

The value of n decreases with increasing depth (Arcement & Schneider, 1989), ranges from as low as 0.012 to greater than 0.1, and its accurate determination depends on experience, with much room for interpretation (Rantz et al., 1982a). The base Manning's roughness coefficients and adjustment factor values for the Cowan (1956) method are available in Arcement and Schneider (1989).

The soil composition and flow conditions were assessed for each stream channel, and a probable minimum and maximum value was estimated for each of the correction factors (n_1, n_2, n_3, n_4, and m) based on these channel assessments. Uncertainty is present in the parameterisation of this method, so an average (n_{avg}) of the probable maximum and minimum n values from the Cowan (1956) approach, and a third estimate from Table 7-1 of Bedient, Huber, and Vieux (2013), was adopted for the calculation so that extreme error resulting from this process might be avoided. The equation for this procedure was as follows:

$$n_{avg} = \frac{n_{max} + n_{min} + n_{BHV}}{3} \tag{7}$$

where n_{max} is the probable highest Manning's roughness coefficients calculated using the approach prescribed by Cowan (1956)
n_{min} is the probable lowest Manning's roughness coefficients calculated using the approach prescribed by Cowan (1956)
n_{BHV} is the estimate using the approach prescribed by Bedient et al. (2013)

Conventional optical surveying equipment was used to dimension stream channel cross-sections, reach lengths, calculate the slope of the stream surfaces, and associate the estimated peak channel stage to a datum (i.e., the pressure transducer sensor elevation). Stream morphological features were used to estimate the maximum channel stage and the hydraulic radii of the streams. The mean velocities of the streams were calculated and multiplied by a measure of their respective cross-sectional areas to compute the peak channel discharge of each stream.

Manning's equation is empirical and limited in its representation of natural systems (Bedient et al., 2013; Mitchell, 1954). Uncertainty is introduced by the inaccuracy of the channel survey, the selection of Manning's roughness coefficients, and the non-uniformity of the stream channel. Steady uniform flow was assumed (i.e., the energy grade line was equal to the slope of the water surface and the slope of the stream channel; Bedient et al., 2013; Mitchell, 1954). Assumptions of uniform flow were often violated within the streams; however, this is often accepted in engineering applications with the understanding that this assumption is only an estimation of the true hydraulic conditions.

2.4.4 Drainage-Area Ratio

Drainage-area ratios are commonly used to estimate streamflow for catchments that lack field data (i.e., ungauged) by assuming that their ratio of flow to catchment area will be equivalent to that of a nearby catchment with streamflow data (i.e., gauged; assuming a value of 1 for the correction factors). Drainage-area ratios were used in this study to estimate the amount of streamflow attributable to subcatchment area downgradient of gauging locations and to estimate the flow of Stream C4 (Emerson et al., 2005; Figure 33, Appendix A). It is generally accepted that this method should only be applied where the drainage area ratio ($A_{ungauged}/A_{gauged}$) is between 0.5 and 1.5, though liberties are often taken (Hortness, 2006). The drainage area ratio equation can be expressed as (Archfield & Vogel, 2010; Asquith et al., 2006; Emerson et al., 2005; Hortness, 2006; Mohamoud, 2008):

$$Q_{ungauged} = \beta \times \left(\frac{A_{ungauged}}{A_{gauged}}\right)^{\varphi} \times Q_{gauged} \qquad (8)$$

where	$Q_{ungauged}$	is the calculated flow from the ungauged location
	Q_{gauged}	is the measured flow from the gauged location
	$A_{ungauged}$	is the drainage area of the ungauged location
	A_{gauged}	is the drainage area of the gauged location
	φ	is a correction factor often assumed as 1 (Asquith et al., 2006)
	β	is a correction factor often assumed as 1 (Asquith et al., 2006)

Correction factors often diverge from 1 in reality (e.g., Asquith et al., 2006; Emerson et al., 2005), but were assumed as unity for this study. More sophisticated models were not deemed necessary (e.g., Archfield & Vogel, 2010; Li et al., 2019; Mohamoud, 2008) given the similarity and proximity of the subcatchments within the KW.

2.4.5 Stage-Discharge Relationship

It is common practice to plot discrete pairs of stream stage and discharge in order to perform a regression that allows for the interpolation and/or extrapolation of values not directly measured (Rantz et al., 1982b). Stage-discharge relationships are typically computed using a power function, as outlined in Braca (2008) and Rantz et al. (1982b):

$$Q = C(h - a)^{\theta} \qquad (9)$$

where	Q	is the (stream) discharge (m^3/s)
	h	is the stream stage (m)
	C	is a calibration coefficient related to the stream characteristics (m^2/s)
	a	is a calibration term related to the stream characteristics (m)
	Θ	is a calibration exponent related to the stream characteristics

Power functions for stage-discharge relationships were defined in Microsoft Excel using least-squares regression in this study. Errors in the discharge estimates extracted from these rating curves are associated with the selected curve fit, the stability and robustness of the derived relationship, the accuracy of stage and flow measurements, and the neglect of variables other than stage that may influence the accuracy of the stream discharge estimate (Dymond & Christian, 1982). Aggregated uncertainty for low-flow stream discharge estimates using stage-discharge relationships are typically high, with confidence bounds between ±50-100% (Mcmillan et al., 2012).

2.5 Hydrogeological Assessment

2.5.1 Groundwater Well Installation & Design

This study utilised *in-situ* field measurements of certain aquifer properties to inform subsurface modelling. Based on the provincial soil surveys, a shallow groundwater piezometer (DalWell) was installed near the centre of the watershed to target surficial soils decently representative of the watershed. Due to budgetary and technological limitations, only one piezometer was installed at the site, and it did not penetrate the bedrock. The DalWell design is presented in Figure 9. This well was used to monitor groundwater level and temperature, and it was used to conduct a slug test adjacent to the lagoon. In addition, temperature and pressure data from a nearby government upland observation well (herein referred to as PEIGov Well) were used (well located at 46.4000°N, -62.2500°W; Government of PEI, 2021). These two wells provide insight into the range of water table depths and vadose zone thicknesses that may be expected within the KW.

Driving methods are regarded as the best installation method to minimise the disruption of the subsurface formation (Aller et al., 1991; Butler, 1998); however, this installation method was unfeasible for the DalWell within the project constraints. A diamond-tipped backpack drill that flushed the soil using water was used to produce a hole in which PVC casing was later installed. The flushing mechanism of the drill made it necessary to fill extra circumferential space with an artificial filter pack (medium sand), but it is expected that the surrounding till rapidly intruded this sand pack, reducing the opportunity for preferential vertical flow. A filter sock was installed over the screened section of the well to reduce sediment intrusion. Finally, the circumference of the well towards the ground surface was capped using bentonite powder.

Minimal well development occurred immediately following well installation on August 15th, 2019; however, approximately nine well volumes were removed from the well with a bailer between November 4-6th, 2019, prior to initiating the slug test. Slow water recovery rates were a challenge, but the water clarified significantly over the development process. Regardless, it is expected that the screened section is partially developed, as straddle packers or surge blocks were not employed to enhance well skin removal (Butler, 1998), which may reduce the hydraulic conductivity estimate derived from the slug test.

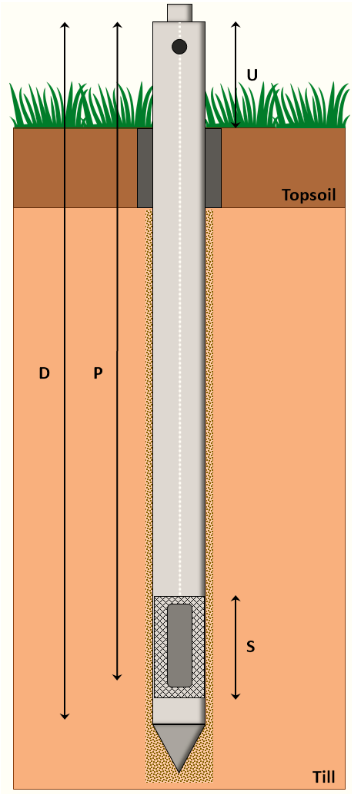

Figure 9. Conceptual diagram of the Dalhousie piezometer (DalWell; not to scale). The well was constructed from a 1-inch PVC pipe outfitted with a screened portion of horizontal incisions, a filter sock, a vent hole, a plastic conical tip, and a J-plug to cap it. A HOBO U20-001-01 (±0.5 cm accuracy and 0.21 cm resolution) pressure transducer was suspended into the well from the J-plug to a depth of approximately 4.3 metres below ground. D = well length ≈ 4.75 m; S = screen length ≈ 0.225 m; U = stick-up length ≈ 0.295 m; P = length to sensor ≈ 4.11 metres before Nov 5th, 2019, and 4.53 metres thereafter.

2.5.2 Slug, Pumping, & Specific Capacity Hydraulic Tests

A slug test is a single well test to assess the *in-situ* hydraulic conductivity of the subsurface materials immediately surrounding a well casing (Aller et al., 1991; Butler, 1998). During a slug test, a record of well recovery is taken after a near-instantaneous volumetric change is induced in the well (Aller et al., 1991; Butler, 1998). Estimates of hydraulic conductivity and specific storage may be calculated by comparing the recovery data with theoretical models of the systems response under various assumptions (Butler, 1998). Due to common installation and development challenges (e.g., well skins, limited development), slug tests should always be regarded as a lower bound of the hydraulic conductivity of the tested soils (Butler, 1998).

A slug test was conducted within the DalWell using an Onset HOBO® U20-001-01 level logger at 10:49 on November 6th, 2019. The well penetrated to a depth of approximately 4.3 metres into till overburden. The well was bailed dry using a manual ball-valve bailer, and the logger was installed using a 10-second interval for over 3 hours. The logger was then removed, the data extracted, and the logger reinstalled using a 15-minute logging interval. The data for the second half of the recovery curve was collected on November 26th, 2019. Thus, the well was permitted to recover to 100% (Figure 19), which aligns with the recommendation of Butler et al. (2003). As before, local pressure data were corrected using nearby pressure data from ECCC weather stations (Station IDs 7177 and 41903).

The Hvorslev slug test method (Hvorslev method) was applied in this study for its simplicity and widespread adoption in practice for overdamped recovery data (Butler, 1998; Fetter, 2001; Hvorslev, 1951). The Hvorslev method was developed for confined aquifer slug tests (Butler, 1998); however, if the length of a fully-penetrating screen section (L_e) is greater than 8 times larger than the radius of the screen (i.e., the casing diameter and filter pack, R_{screen}), than the Hvorslev method may be applied to unconfined systems (Fetter, 2001). The equation applied in the Hvorslev method is (Butler, 1998; Fetter, 2001):

$$K = \frac{r^2 \ln\left(\frac{L_e}{R_{screen}}\right)}{2L_e t_{37}} \tag{10}$$

where	K	is the horizontal hydraulic conductivity (m/s)
	r	is the radius of the well (m)
	R_{screen}	is the radius of the well screen (m)
	L_e	is the length of the screen section (m)
	t_{37}	is the time it takes for the water level to recover 37% (s)

The response data should plot a relatively straight line to apply the Hvorslev method. The mathematical basis and limitations for the Hvorslev method can be found in Butler (1998).

The Bouwer and Rice (1976) empirical model was also applied and likely represented a more theoretically sound model for the DalWell. This model is based on a particular formulation of the Thiem equation representing the flow into a well from an unconfined aquifer (Bouwer & Rice, 1976). The Bouwer and Rice (1976) model assumes that the drawdown of the water table is negligible, unsaturated flow may be ignored, screen effects are negligible, and that the aquifer is homogenous and isotropic. Saturated radial conductivity can be computed using recovery data and well dimensions through the following equation (Bouwer & Rice, 1976):

$$K = \frac{r^2 C_{ana}}{2L_e} * \frac{1}{t} \ln\left(\frac{H_o}{H_t}\right) \tag{11}$$

where t is time (sec)
C_{ana} is an empirical coefficient computed via an electrical resistance analog
H_o is the initial drawdown (m)
H_t is the drawdown at time t (m)

The hydraulic conductivity of the surficial soils was estimated via slug test analysis, and the characterisation of the surficial soils was further bolstered by the definition of a soil-water characteristic curve for the Charlottetown soil series (approach detailed in Appendix D). Additionally, bedrock bulk hydraulic conductivity was estimated through the analysis of a former pumping test conducted by Joostema (2015) in Souris, PEI (approach detailed in Appendix C, Section 1), and a specific capacity test performed on a residential well in the KW. Both the Theis (1935) and Warren and Root (1963) models were used to analyse the drawdown data of the pumping test, and limitations for these models are presented in Halford and Kuniansky (2002) and Kruseman and de Ridder (2000), respectively. Separately, the specific capacity test was assessed using the Thomasson Jr. et al. (1960) semi-analytical model as well as several empirical relationships (approach detailed in Appendix C, Section 2). The results of the hydraulic analyses were considered during the parameterisation and calibration of the numerical subsurface model.

2.6 Spring Thermal-Discharge Assessments

The methods within this section are based on an approach proposed by Roseen (2002), which was later modified by Danielescu, MacQuarrie, and Faux (2009). Thermal-discharge assessments (TDAs) are empirical approaches to groundwater discharge quantification that utilise the geometry of a thermal plume to infer discharge to a receiving body. Different TDA methods have been demonstrated in the literature. Roseen (2002) defined plume area graphically by binning the grayscale intensities (GsI) of thermal image pixels, whereas Danielescu et al. (2009) used calibrated temperature pixel values instead. At their core, their methods were the same, as GsI and red-green-blue intensity are relative scales used in thermal images to visually represent temperature pixel data to the user. These approaches are mathematically distinct from methodologies that define the plume boundary as the average maximum rate of change in temperature, among a sample of plume transects, which has been adopted to analyze several large scale thermal anomalies (e.g., Bejannin et al., 2017; J. L. Kelly et al., 2013; Tamborski et al., 2015). Each of these methods incorporates practitioner bias into the analysis, but they are systematic and efficient approaches to analyze the spatial data of thermal plumes. However, it is important to recognise that plume analysis methods may calculate different areal magnitudes for the same thermal plume based on their definition of plume extents.

Roseen (2002) demonstrated that the GsI of thermal images could be graphed with respect to cumulative area to yield a type-curve with a characteristic S-shape (Figure 10). They used the "inflection points" of the graph to identify various "thermal groups". Each thermal group of their type-curves demonstrated near-linear behaviour with a sharp transition zone between them (Figure 10), but this pattern is dependent on adequate thermal contrast between thermal groups and mixing dynamics. It was observed that additional inflection points may exist along the curve where multiple thermal groups exist within a frame (e.g., Figure 43, Appendix B) – though this phenomenon is mostly avoidable through image cropping. If the analysis conditions are uncomplicated, the first inflection point on the type-curve generally indicates the area of the plume thermal group (Figure 10). Sharp transitions in slope can be associated with transitions between thermal groups, which can be confirmed through the manual inspection of image pixel values.

Danielescu et al. (2009) demonstrated that the methodology of Roseen (2002) may be applied to quantify direct spring discharges to coastal environments by correlating discharge measurements with the area of spring thermal plumes. Initially it was believed that the correlation function of their study could be directly applied to BHH to estimate focussed spring discharge (Danielescu et al., 2009), but despite the many similarities the studies share, the methodological differences were too substantial to ignore. Ultimately it was decided that exclusively site-specific measurements for BHH would be more reliable and theoretically defensible in this study.

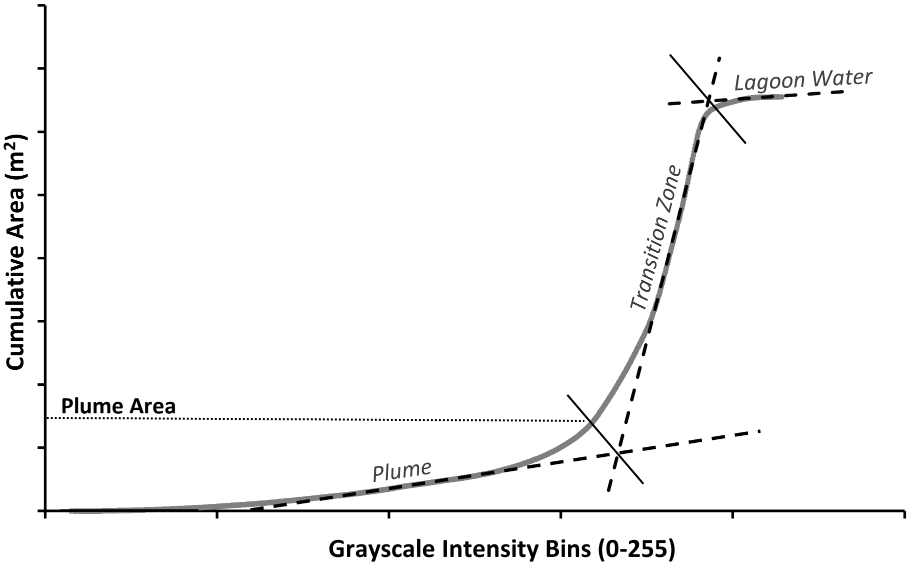

Figure 10. Generic characteristic type-curve used in the areal analysis of a thermal-discharge assessment. Inflection points are identified using perpendicular lines connecting the type-curve and the linear intersects. The plume thermal group (i.e., plume area) extends to the plume area inflection point, the lagoon thermal group begins at the second inflection point and extends onward, and there is a steep transition zone between them.

The TDA method of this study applied FLIR Tools®, ImageJ, MATLAB®, and M-B Ruler (Bader, 2020) in conjunction with images captured by the XT2. FLIR Tools® and ImageJ are image analysis software products, and M-B Ruler is a digital measurement application that enabled pixel-level accuracy when analyzing type-curves manually. Given the novelties of this approach, a short comparative study was conducted to assess the differences between the calculated plume areas of slightly different areal quantification procedures (included for reference in Appendix B, Section 3). Experiments were devised to assess the effect of different FLIR Tools® enabled colour scales (i.e., temperature linear, signal linear, histogram equalisation, and contrast optimised), image cropping, axis scale, and the utilisation of either temperature or GsI pixel data. The outcome of this brief study was the selection of a protocol that utilised temperature linear grayscale data and extensive cropping procedures on thermal images with springs near their centre (i.e., GiS-2, Appendix B, Section 3).

The main drone expedition was conducted from July 21 to 24th, 2020 under mainly clear conditions. Images were taken from approximately 60 metres above mean sea level (spatial resolution of 6 cm/pixel), apart from two images that were respectively taken from 50 and 100 metres (spatial resolution of 5.23 and 10.46 cm/pixel, respectively). Surveys were temporally planned to target the diel lagoon water temperature extremes, low-low tide (±2 hours), and the seasonal period of greatest thermal contrast between groundwater and the lagoon. Two plumes in the main basin (i.e., Spring 1 and 2) were inadequately captured in the initial survey and were rephotographed during the next field visit on August 29th, 2020, when lagoon water temperatures were notably cooler than the last week of July. Colder lagoon waters may result in reduced contrast between the springs and lagoon, smaller areal extent of the plumes captured using TIR imagery, and ultimately lower discharge estimates relative to the July conditions.

Drone thermal images were imported into FLIR Tools®, and the full range of the colour scale was converted to a linear GsI. Images were subsequently imported to ImageJ for cropping, removing the FLIR logo and scale, reducing the impact of vignetting effects, and minimizing interference with thermal group definition. Within ImageJ, cropped thermal images were formatted as 8-bit grayscale images (e.g., Figure 11), wherein black represented colder zones and white represented relatively warmer zones. The image was then exported to spreadsheet software (e.g., Microsoft Excel, or MATLAB®) as a text matrix of GsI pixel values for analysis.

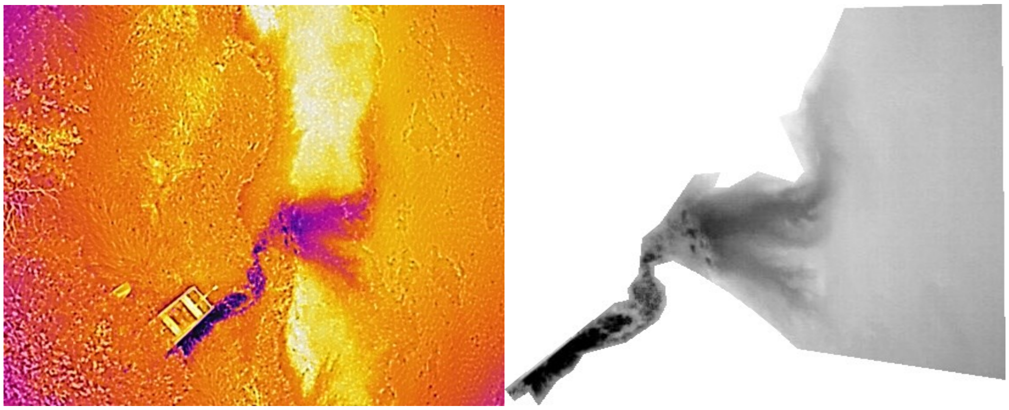

Figure 11. Raw thermal image of groundwater spring in Basin Head Harbour (left) and example of image cropping (ID_GiS-2). These images are to scale, but do not share the same scale for the purpose of visual clarity. As a spatial reference, the angular object in the bottom left of the coloured image is the back of a motorboat that is approximately 10 ft in length. The image was taken on August 16, 2019, at 17:00 AST during clear skies, low tide, and near-peak thermal contrast.

The post-processing of GsI matrix data exported from ImageJ was automated using a custom MATLAB® script developed by the author. Matrix data were transformed into a single vector of grayscale intensities for ease of use. The area represented by each pixel (i.e., spatial resolution) was estimated using the Pix4D GSD Calculator (Pix4D, 2020). A binning procedure was applied to each image to calculate the area occupied by each unique grayscale value (i.e., grayscale intensities between 0 and 255), assuming that spatial distortion was negligible. Differences in spatial resolution, colour depth, survey environmental conditions, and camera accuracy introduce uncertainty into the intercomparison of images.

Cumulative area was graphed with respect to unique GsI values (from smallest to largest) to yield a type-curve for the thermal image. Inflection points can be estimated graphically using the method described by Roseen (2002), through visual inspection, or by automated search algorithm so long as there is adequate thermal contrast between thermal groups (Danielescu et al., 2009). Each method introduces arbitrary bias, so the simple graphical method of Roseen (2002) was adopted. Thus, inflection points between thermal groups were determined graphically by fitting linear segments for each group and connecting their intersections with a perpendicular line to the type-curve (e.g., Figure 10). The inflection points of the graphs were analyzed with coincident consideration of the associated thermal image pixel values and available site data to define thermal groups. For systematic consistency, the inflection point between the transition zone and the spring was chosen to define the spring area thermal group (Danielescu et al., 2009; Roseen, 2002).

Volumetric measurements of springs were made with an accuracy of ±10 mL, but flows were not entirely captured at the spring outlet due to limitations with the water collection technique, soil properties, and geometry of the outlet. The proportion of missed flow was estimated by relative comparison with the captured flow and used to increase flow estimates accordingly. Three involved field workers came to a provisional consensus that the flows estimated via this technique were likely within 25% of the true spring discharge.

Three calculated plume areas were correlated with temporally paired direct volumetric measurements of discharge at low tide (i.e., Springs A, B and C). The area-discharge relationship based on this correlation was used to estimate discharge for all ungauged springs in BHH based on their areal extent alone. Discharge estimates were temporally paired with water table measurements and the nearest stream baseflow measurement to compute two proportionality constants. These empirical associations are based on the premise that the magnitude of spring flow is physically controlled by the hydraulic gradient via Darcy's Law. It was assumed that both baseflow and groundwater levels are controlled by associated hydrogeological mechanisms and were effective proxies for land-to-lagoon hydraulic gradients. Thus, continuous baseflow and water table records were used in conjunction with the computed proportionality constants to derive rough estimates of continuous spring discharge over the sample period. These approaches are comparable to the method of Danielescu et al. (2009) to estimate annual discharge from coastal springs, wherein baseflow was used as a proxy for water table measurements.

In addition to the influence coastal gradients have on spring discharge, field observations and physical theory suggest that tidal head affects the flow rate of springs (e.g., Dong-Woon & Byoung-Seol, 2012; KarisAllen & Kurylyk, 2021). Over the tidal cycle, the plume area and discharge of springs at low tide may be assumed at a maximum due to the peak hydraulic gradient, although aquifer desaturation processes and hydrodynamic factors may have an effect based on field observations. The author was unable to identify a TDA that incorporated provisions for the influence of tidal head, so field observations and data were used to develop a simplistic model to estimate the tide-averaged spring discharge from the discharge measured or estimated at low tide. The plume areas of select springs were compared in July at high and low tide to develop a correction factor to account for the influence of tidal head on spring discharge. The proposed generalised tidal correction factor (C_{tidal}), is based on the average ratio of low tide and high tide plume areas for a sample of springs in BHH:

$$C_{tidal} = \frac{\sum_{n=1}^{N} 1 - (1 - \frac{AreaHigh_n}{AreaLow_n})/2}{N} \tag{12}$$

where	i	is the spring index
	N	is the total number of assessed springs
	$AreaHigh_n$	is the high tide plume area of a given spring
	$AreaLow_n$	is the low tide plume area of a given spring

Equation 12 utilises the plume area of a spring as a proxy for volumetric discharge, consistent with the TDA framework. It was assumed that the differences in discharge may be characterised by comparing the low tide and high tide plume areas, which reflect different discharge conditions influencing plume geometry. This conception also assumes symmetry of ebb tides, flood tides and of the discharge magnitudes across both. Equation 12 suggests that springs have no flow once high tide is reached if there is no observable thermal plume (i.e., $AreaHigh_n = 0$), and that discharge linearly increases from no flow to maximum flow from high tide to low tide and vise versa. Thus, a C_{tidal} of 0.5 assumes that tidal influences reduce the total discharge rate by 50% over a tidal cycle compared to a low tide-based estimate. In reality, tidal asymmetry is present at BHH, controls on spring discharges are numerous and complex, and at least some flow has been observed from certain springs during high tides even though a plume may not be evident at the surface using thermal imaging. The simplicity of this mathematical model was deemed acceptable as a suitable first step towards accounting for the influence of tidal action on groundwater discharge using TDAs, as discharge could not be directly quantified in any of the intertidal springs at high tide.

Given the uncertainty with the adopted model for the generalised tidal correction factor, several assumed values were tested to examine their impact on spring discharge:

1. Spring discharge is unaffected by tidal stage ($C_{tidal} = 1$);
2. Spring discharge stops exactly at high tide with symmetrical tides ($C_{tidal} = 0.5$);
3. An intermediate value ($C_{tidal} = 0.75$); and
4. C_{tidal} computed by Equation 12 using plume areas from thermal images.

The first scenario is currently the most common assumption in past studies involving TDAs of coastal springs and assumes that tidal head has an insignificant effect on the groundwater discharge of springs. Field observations and theory do not corroborate this framework. The second scenario and its assumptions were discussed previously, and the third scenario is probably closer to reality, where spring discharge dynamics probably fall in between the first and second scenario on average. The final scenario attempted to use field data of plume areas from six springs of diverse magnitude to calibrate a representative tidal correction factor for BHH. Based on field observations, it is likely that the hydrodynamics of each spring have their own unique relationship with tidal stage, as the thresholds and processes that enable or impede their flow are different and dynamic (e.g., aperture location and shape, magnitude of spring flow, and aperture blockages from sediment or seaweed). In addition, thermal imagery can only capture skin temperature and may not always be able to register thermal disturbances that are either too deep or small.

The calculated density of near-shore spring discharge (i.e., discharge per meter of coastline) along the surveyed coastline of BHH was used to estimate the discharge originating from coastal segments that could not be surveyed due to safety concerns (i.e., presence of power lines, hazardous access, and public roadways). Approximately 20% of the northwestern shore of BHH was unsurveyed by drone. These regions included a small embayment in the northwestern part of the main basin and a segment to the west of the main basin and entrance of BHH.

Finally, it is anticipated that springs unable to generate thermal disturbances at the surface of the lagoon were inevitably missed, and that some amount of recirculated salt water may be present during discharge measurements. Local knowledge indicated that there were large springs near the centre of the main basin (personal communication in Basin Head

Advisory Board Meeting, 2019), but these were not readily identified via airborne thermal surveys or by handheld devices. Uncaptured flow of this kind could not be estimated in an informed manner, so this is an unaddressed uncertainty of the study. Conversely, the proportion of salt water in the measured spring discharge was estimated via a two-component mixing model by using electrical conductivity as a proxy for water salinity. A summary of the workflow for this study's TDA is provided for additional clarity in Figure 12.

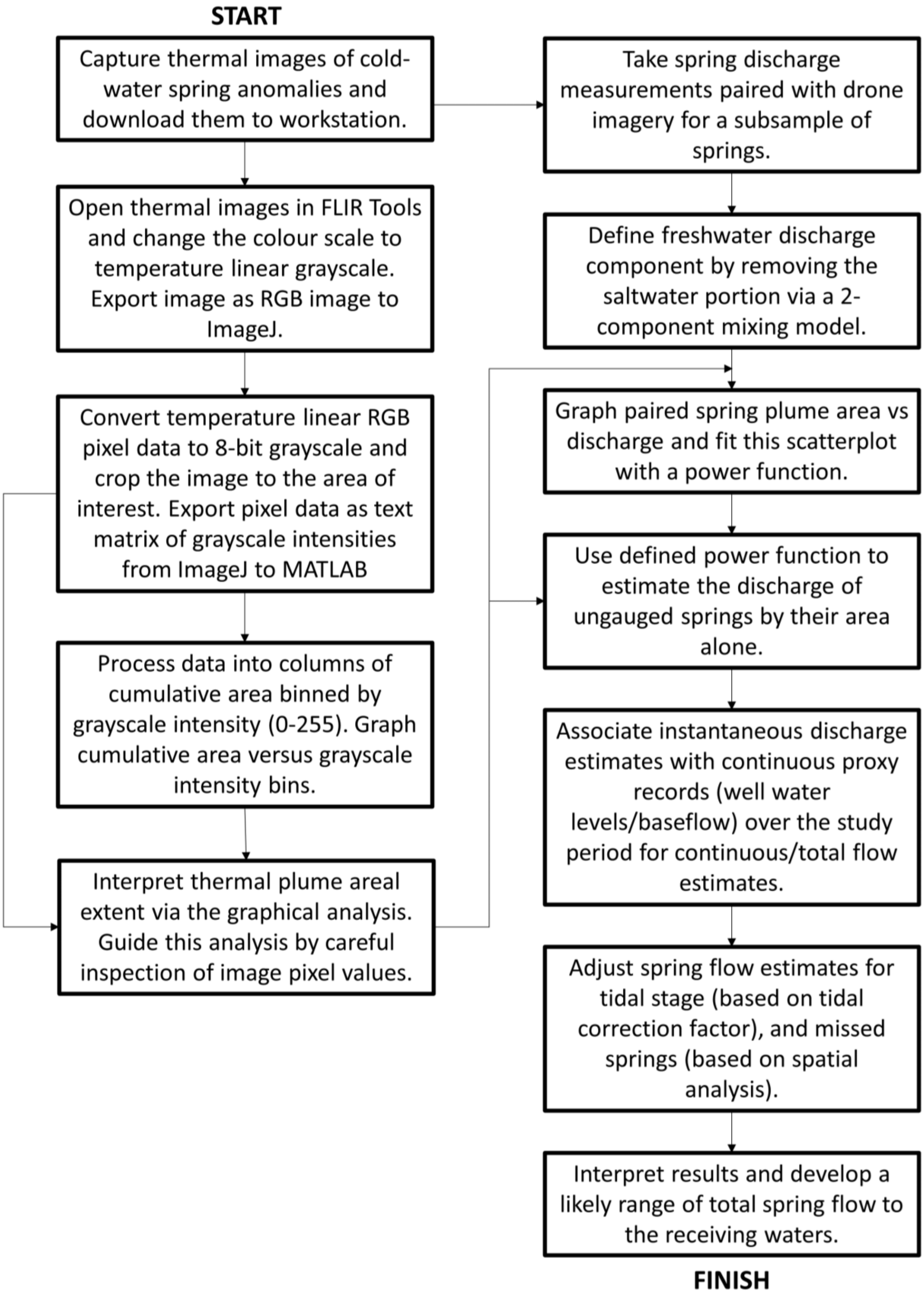

Figure 12. Summary workflow of the thermal-discharge assessment applied in Basin Head Harbour.

2.7 Thermal Modelling – SHAW

Numerical modelling of an aquifer's response to projected future climate change is one method that can be implemented to investigate how the buffering capacity of groundwater in BHH may change over time. Given the lengthy 81-year projection period and various unavoidable uncertainties throughout, adequately capturing the physical processes of the system is especially important. Topographically variable groundwater depth, frozen soil dynamics, snowpack dynamics, vegetation, and climatological factors will play important roles in dictating future thermal changes in the subsurface. Considering the resource limitations and exploratory nature of the project, a physically complex one-dimensional model was selected to model soil processes: the Simultaneous Heat and Water model (SHAW; Flerchinger & Saxton, 1989). This section gives a brief introduction to the SHAW model (version 3.0), which is designed and freely distributed by the U.S. Department of Agriculture.

SHAW simultaneously solves sophisticated transient one-dimensional simulations of energy, moisture, and solute transport through a canopy, snow layer, plant residue, and soil layers in a vertical domain at hourly or daily timescales (Flerchinger, 2017). The software simultaneously computes implicit finite difference solutions for these processes using an iterative Newton-Raphson technique (Flerchinger, 2017). Input climatological parameters force the simulation of surface boundary radiation, conduction, and convection to the subsurface as well as precipitation-infiltration and runoff processes (Flerchinger, 2017). The ability of SHAW to simulate snowpack, canopy, and seasonally frozen soils (e.g., Mohammed et al., 2017) made it an appealing choice for this long-term thermal study, as these processes likely impact subsurface thermal trends.

The soil water flux equation used by SHAW to simulate water storage and transport is:

$$\frac{\partial \theta_l}{\partial t} + \frac{\rho_i}{\rho_l}\frac{\partial \theta_i}{\partial t} = \frac{\partial}{\partial z}\left[K_{unsat}\left(\frac{\partial \psi}{\partial z} + 1\right)\right] + \frac{1}{\rho_l}\frac{\partial q_v}{\partial z} + U \qquad (13)$$

where	Θ_l	is the volumetric liquid water content ($m^3\ m^{-3}$)
	Θ_i	is the volumetric ice content ($m^3\ m^{-3}$)
	ρ_l	is the density liquid water ($kg\ m^{-3}$)
	ρ_i	is the density of ice (water) ($kg\ m^{-3}$)
	K_{unsat}	is the unsaturated conductivity ($m\ s^{-1}$);
	ψ	is the soil matrix potential (m)

	q_v	is the water vapor flux (kg m^{-2} s^{-1})
	U	is a source/sink term for water flux (m^3 m^{-3} s^{-1})
	z	is the location within the vertical domain (m)
	t	is time (s)

The surface energy balance of SHAW is computed via (Flerchinger, 2017):

$$R_n + H + L_v E + G = 0 \tag{14}$$

where	R_n	is the net all-wave radiation (W m^{-2})
	H	is the sensible heat flux (W m^{-2})
	L_v	is the latent heat of evaporation of water (J kg^{-1})
	G	is the soil heat flux (W m^{-2})
	E	is the total evapotranspiration from the soil and vegetation (kg m^{-2} s^{-1})

The soil heat transport equation used by SHAW to account for subsurface conductive and advective heat transfer, freeze-thaw, and vaporisation is (Flerchinger, 2017):

$$C_s \frac{\partial T}{\partial t} - \rho_i L_f \frac{\partial \theta_i}{\partial z} = \frac{\partial}{\partial z}\left(k_s \frac{\partial T}{\partial z}\right) - \rho_l c_l \frac{\partial q_l T}{\partial z} - L_v \left(\frac{\partial q_v}{\partial z} + \frac{\partial \rho_v}{\partial t}\right) \tag{15}$$

where	C_s	is the volumetric specific heat capacity of the soil (J m^{-3} °C^{-1})
	T	is the temperature of the soil (°C)
	k_s	is the soil thermal conductivity (W m^{-1}°C^{-1})
	L_f	is the latent heat of fusion of ice (335,000 J kg^{-1})
	c_l	is the specific heat capacity of liquid water (J kg^{-1}°C^{-1})
	q_l	is the liquid water flux (m s^{-1})
	ρ_v	is the vapor water density within the soil (kg m^{-3})

Additional one-dimensional heat and mass transport equations are also defined for the canopy, vegetation residue, and snowpack layers in the model. These equations, as well as the available solute transport and boundary condition options of SHAW are detailed in the technical documentation (i.e., Flerchinger, 2017). A modified version of SHAW was used for the lower domains, which exclusively calculated subsurface thermal transport via conduction. Thermal conductivity and heat capacity of the subsurface is estimated within the model based on DeVries (1963) by using user-input soil compositions and water content.

2.7.1 Modelling Framework & Objectives

The first objective of the modelling component of the study was to develop a subsurface heat transport and water flow model that was manually calibrated to subsurface temperature observations within the KW. Secondly, the resulting domain was assumed generally indicative of current conditions, and future climate projections were imposed on this domain to simulate possible future subsurface conditions. Data scarcity was a significant constraint on this modelling study. As such, attempts were made to limit the complexity of the model to facilitate the interpretation and parameterisation of the model, while still preserving key heat transport processes. Ultimately, the goal was to assess the potential sensitivity of springs to projected multidecadal warming signals.

A surface domain was developed which included complex heat exchange processes occurring in an idealised canopy, residue layer, snow layer, and shallow unsaturated soil domain. After calibration to field observations, daily temperature timeseries were extracted from the surface domain and used as upper boundary conditions for two deeper, fully-saturated, conduction-only model domains. The division of the model into two separate domains enhanced the stability and resolution of the model at the cost of some physical complexity and succinctness. This simplified approach enabled a systematic model calibration and sensitivity analysis while still accounting for many intricacies of thermal transport at the ground surface and throughout the vadose zone. The results of the model sensitivity analysis and calibration are discussed in Section 3.7.

After the model was calibrated to baseline conditions, four future climate simulations (two climate models and two RCPs) were applied to the domains, resulting in eight possible projections (four climate scenarios and two domains) of spring temperatures for the year 2100. The resulting 2100 subsurface temperatures were compared to the modelled subsurface and air temperatures of 2020 to estimate the relative temperature changes and warming rates experienced by the modelled system.

2.7.2 Modelling Period & Temporal Resolution

All simulations and input data had a daily resolution. Based on the years of data collection for this study and the availability of historic data and climate projections, historical simulations were conducted over 37 years (1984-2020), and future simulations were run over 81 years (2020-2100). Outputs were extracted and analysed at a daily timestep.

2.7.3 Boundary Conditions & Climate Data

The upper boundary condition of the surface domain was forced using daily climate data. These model inputs control the transport of water and heat in/out of the subsurface. Climate inputs required by SHAW include maximum air temperature, minimum air temperature, dew point temperature, wind speed, total precipitation, and all-sky radiation. The minimum and maximum air temperatures, as well as total precipitation for the historical simulation period were sourced from the CNRM-CM5, RCP4.5 hindcast model (Voldoire et al., 2013). The CNRM-CM5 model was demonstrated to reflect historical conditions for Charlottetown, PEI, more accurately than the other short-listed options evaluated by Warner (2016). Dew point temperature, wind speed at two metres above ground level, and all-sky solar radiation data were sourced from the NASA POWER database for BHH (Sparks, 2018).

The surface domain had a free drainage bottom boundary and a calculated bottom temperature boundary (A, Figure 13 and Figure 14). Within SHAW, a calculated bottom boundary involves the interpolation of the bottom temperature boundary using the node above it and an estimation of the extinction depth of the thermal signal below it (assumed as a temperature of average air temperature). The surface domain simulated the vadose zone processes for both lower domains.

For the two lower domains, the bottom boundary was far below the anticipated extinction depth calculated by SHAW. As SHAW is typically intended for shallow domains, a geothermal heat flux boundary is not possible within the model. Therefore, a constant temperature boundary was defined based on regional geothermal surveys (Grasby et al., 2009). The two lower domains were designed to investigate the impact of water table depth. Daily temperature timeseries were extracted at depths of 3 and 7 metres (i.e., the average water table depths in the lowland and upland well, respectively) in the surface domain and used to force the upper boundary of the respective deeper saturated domains (Figure 13Figure 14 and Figure 14). These lower domain simulations only account for conductive heat transport in the fully saturated zone.

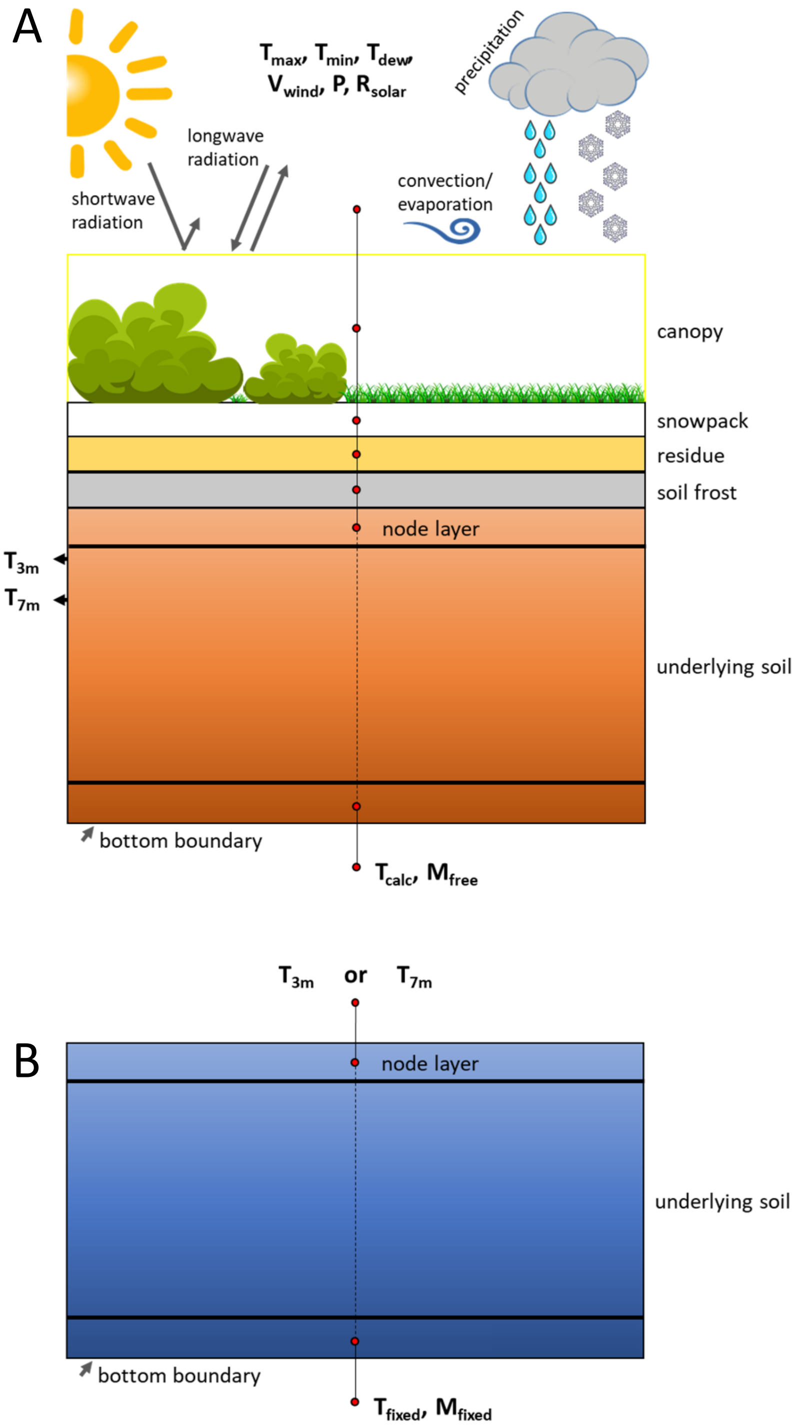

Figure 13. (A) Conceptual diagram of the 1D SHAW surface model domain and boundary conditions. Atmosphere-subsurface-interface processes at the upper boundary are computed via the input of min and max temperature (T_{min} and T_{max}), dew point temperature (T_{dew}), windspeed (V_{wind}), precipitation (P), and solar radiation (R_{solar}). The bottom thermal boundary is calculated based on an estimation of annual signal extinction depth, and water drains freely from the bottom maintaining the simulation of a vadose zone. (B) Conceptual diagram of the1D SHAW bottom model domains and boundary conditions. The upper boundary condition is either the temperature output from 3 m (T_{3m}) or 7 m (T_{7m}) from the surface model domain. The bottom thermal boundary is a fixed temperature (T_{fixed}), and the domain is maintained fully saturated by a fixed matric potential boundary (M_{fixed}).

The link between the surface domain and two lower domains was identical for the future simulation period, but the climate data of the surface domain was altered. There were no readily accessible future projections for dew point temperature, wind speed, and all-sky solar radiation, so these were estimated by repeating the 36-year historical period of 1985-2020 from the NASA POWER database (Sparks, 2018). Maximum air temperature, minimum air temperature, and total precipitation were sourced from four future climate simulations available from the Canadian Government (ECCC et al., 2021). Ideally, the entire range of available climate projections would have been investigated; however, this was deemed excessively detailed for such an exploratory project with limited resources and data. Four future simulations were selected based on work by Warner (2016) as a compromise: (1) CNRM-CM5, RCP4.5; (2) CNRM-CM5, RCP8.5; (3) MRI-CGCM3, RCP4.5; and (4) MRI-CGCM3, RCP8.5.

2.7.4 Model Initial Conditions

The temperature of the domain must be initialised in SHAW. The average air temperature is recommended in the SHAW technical documentation as the bottom boundary and is approximately 5.8°C for East Baltic, PEI (ECCC, 2021a). A warmer initial temperature was adopted in the shallow model based on field data. For the lower domains, initial temperatures were graded from 6.8°C at 3 metres, to 7.4°C at 50 metres, to 8.4°C at 93 metres based on the geothermal gradient. The extended simulation period is expected to regulate the model sensitivity to initial conditions over the depths of interest.

The matric potential of the domain must also be initialised in SHAW. The modelling framework simplified water table fluctuations to avoid model instability. Thus, the surface domain was unsaturated upon initialisation and had free drainage at the bottom, and the lower domains were maintained fully saturated for the duration of their respective simulations.

2.7.5 Model & Domain Parameterisation

Initial values for the model were determined through a comprehensive literature review and an analysis of regional well water level and core log data. An estimate of the median value of each parameter was initially adopted, and then a manual calibration was conducted within the expected range of possible values to improve agreement with the observation data. Due to the natural variability of fractured bedrock and till, there is a large possible range for the hydraulic properties. The Brooks and Corey (1966) soil-water characteristic curve was selected in SHAW for this study. Thermal properties are calculated by the model internally based on soil composition and moisture, but they are innately less variable than soil hydraulic properties (Anderson, 2005).

Figure 14 displays the soil stratigraphy assumed in the model, the water table depth (which matches the division between the surface and lower domains) for each set of simulations, and the overall dimensions of the domain. Similarly, the range of literature-based estimates of stratigraphy, and those initially selected for the model, are compiled in Table 4 for reference. Water table depths were selected to generally reflect the annual average of two wells (i.e., the DalWell and PEIGov Well) that were expected to be representative of the range experienced in the watershed over the study period (Table 5 and Table 19).

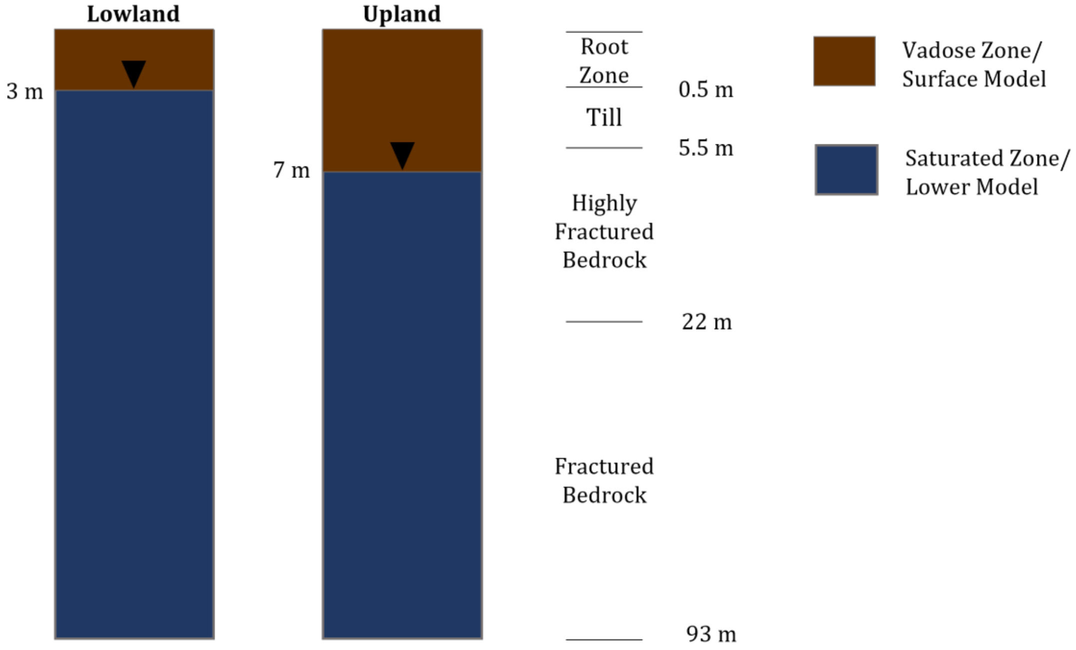

Figure 14. Setup of the lowland and upland domains and their assumed stratigraphy for SHAW modelling of the Kingsboro watershed. Water table depths were selected to reflect the average annual water table depth of a(n) upland and lowland environment in the watershed based on the water level data of two wells. The surface domain model (brown) was simulated in SHAW version 3.0, whereas the lower domain model (blue) was simulated in an early beta version of SHAW that only accounted for conductive heat transport.

Table 4. Estimated stratigraphy of the Kingsboro watershed used in the initial parameterisation of the site's SHAW model. The estimated values for the model (model) are presented with the likely lower (low) and upper (high) bound for the parameters based on literature values for Prince Edward Island geology and the analysis of local well logs.

Layer	**Thickness (m)**			**References**
	Low	**High**	**Model**	
Root Zone	0.5	1	0.5	(Carter, 1987; Joostema, 2015; Zebarth et al., 2015)
Till	0	7	4.5	(Brandon, 1966; Carr, 1969; Crowl, 1969a; Francis, 1989; Government of PEI, 2019; Joostema, 2015; J. I. MacDougall et al., 1988; Tibbet, 2015) and local data
Highly Fractured Bedrock	0	32.5	17	(Francis, 1989; Joostema, 2015) and local data
Fractured Bedrock	NA	NA	71	(Francis, 1989) and local data

Table 5. Initial estimate of water table depths for the site's SHAW model. The estimated values for the model (model) are presented with the likely lower (low) and upper (high) bound for the parameters based on an upland observation well (PEIGov Well) and a lowland piezometer (Dalhousie piezometer or DalWell).

Well ID	**Well Elevation (m)**	**Water Table Depth (m)**		
		Low	**High**	**Model**
DalWell	~5	5	0	2
PEIGov Well	~55	8.9	3.6	7

Estimates of hydraulic conductivity were compiled for the stratigraphic layers of the model from literature and available well test data (Table 6). These conductivities influence the vadose zone processes (i.e., the surface domain simulation) but have no effect on the lower domains. Porosity and density estimates for the stratigraphic layers were compiled in Table 7 and Table 8, respectively.

Table 6. Initial estimate of the hydraulic conductivity of subsurface deposits found in the Kingsboro watershed used in the site's SHAW model. The estimated values for the model (model) are presented with the likely lower (low) and upper (high) bound for the parameters based on literature values for Prince Edward Island and the analysis of local data.

Layer	Hydraulic Conductivity (cm/hr)			References
	Low	High	Model	
Root Zone	0.42	11.75	0.5	(Carter, 1987)
Till	0.02	11.75	2	(Carter, 1987; Francis, 1989; J. I. MacDougall et al., 1988) and local slug test (Section 3.2.2)
Highly Fractured Bedrock	0.036	522	266	(Carr, 1969, 1971; Francis, 1989; Hansen & Ferguson, 2012a; Joostema, 2015), local pumping test and specific capacity-based estimates
Fractured Bedrock	0.036	266	100	(Carr, 1969, 1971; Francis, 1989; Hansen & Ferguson, 2012a; Joostema, 2015), local pumping test and specific capacity-based estimates

Table 7. Initial estimate of the porosity of deposits found in the Kingsboro watershed used in the site's SHAW model. The estimated values for the model (model) are presented with the likely lower (low) and upper (high) bound for the parameters based on literature values for Prince Edward Island.

Layer	Porosity (%)			References
	Low	High	Model	
Root Zone	45	61	50	(Carter, 1987; J. I. MacDougall & Veer, 1981)
Till	20	47	30	(Francis, 1989; Heath, 1983; J. I. MacDougall & Veer, 1981)
Highly Fractured Bedrock	5	38	24	(Brandon, 1966; Carr, 1971; Chi et al., 2003; Dobereiner, 1984; Francis, 1989)
Fractured Bedrock	5	38	18	(Brandon, 1966; Carr, 1971; Chi et al., 2003; Dobereiner, 1984; Francis, 1989; Hansen, 2012)

Table 8 Initial estimate of the bulk density of deposits found in the Kingsboro watershed used in the site's SHAW model. The estimated values for the model (model) are presented with the likely lower (low) and upper (high) bound for the parameters based on literature values for Prince Edward Island.

Layer	**Bulk Density (kg/m³)**			**References**
	Low	**High**	**Model**	
Root Zone	1050	1500	1300	(Carter, 1987; J. I. MacDougall et al., 1988)
Till	1050	1860	1500	(Carter, 1987; J. I. MacDougall et al., 1988)
Highly Fractured Bedrock	1600[a]	2275	1800	(Dobereiner, 1984)
Fractured Bedrock	1700[a]	2275	2000	(Dobereiner, 1984)

[a] *Conservatively low estimate based on observed fracture formations observed in the field and lower bound of Dobereiner (1984).*

Till and bedrock composition and hydraulic properties may be expected to vary substantially in the watershed. Without a substantial soil sampling campaign in the KW, literature values for PEI soils of comparable classification were instead compiled to estimate initial model values and reasonable ranges (Table 9). Gravel and rock content was assumed to be dominantly sandstone (i.e., compositionally mostly sand) for the purpose of this modelling exercise. Initial soil composition estimates were based primarily on detailed studies by Francis (1989) and Tibbet (2015). Organic content in the root zone may be expected to be less than 5% (Carter, 1987) and is likely negligible below this depth.

Table 9. Initial estimate of the composition of till surficial deposits and sandstone bedrock found in the Kingsboro watershed used in the site's SHAW model. The estimated values for the model (model) are presented with the likely lower (low) and upper (high) bound for the parameters based on literature values for Prince Edward Island.

Geological Unit	**Soil Component**	**Proportion (%)**		
		Low	**High**	**Model**
Till	Clay	1	13.3	3
	Silt	7	37	12
	Gravel	3	44	25
	Sand	39	65	60
Sandstone	Clay	2	5	3
	Silt	13	24	18
	Gravel	20	34	29
	Sand	40	54	50

Snowpack likely plays a significant role in buffering the subsurface from heat loss during the winter in PEI, and SHAW has highly detailed physically-based routines for snowmelt and soil freeze-thaw processes (Flerchinger, 2017). User-input climate variables force coupled mass and heat transport processes in a multi-layered snowpack, which are associated with computations of snowpack compaction, settling, and maturation processes in each layer. SHAW infers when precipitation is snow or rain using a user-input temperature threshold and precipitation data. The initial estimate used as a representative rain-snow temperature threshold for the SHAW model was 0.6°C, with a likely upper bound of 2.4°C and a likely lower bound of -0.4°C, based on a study conducted by Jennings et al. (2018). Additional detail on how SHAW accounts for the snowmelt and freeze-thaw processes can be found in the associated technical support document (i.e., Flerchinger, 2017).

CHAPTER 3: ANALYSIS

3.1 Streamflow Assessment

Stream discharge measurements and estimates of maximum stream channel flow were compiled and paired with discrete measurements of stage to develop four stage-discharge relationships fitted using power functions (Figure 15). Periodic volumetric measurements of discharge from a hanging culvert along Stream C7 were correlated with stage measurements from Stream C5 using a power function (Figure 16), as no stilling well was installed therein.

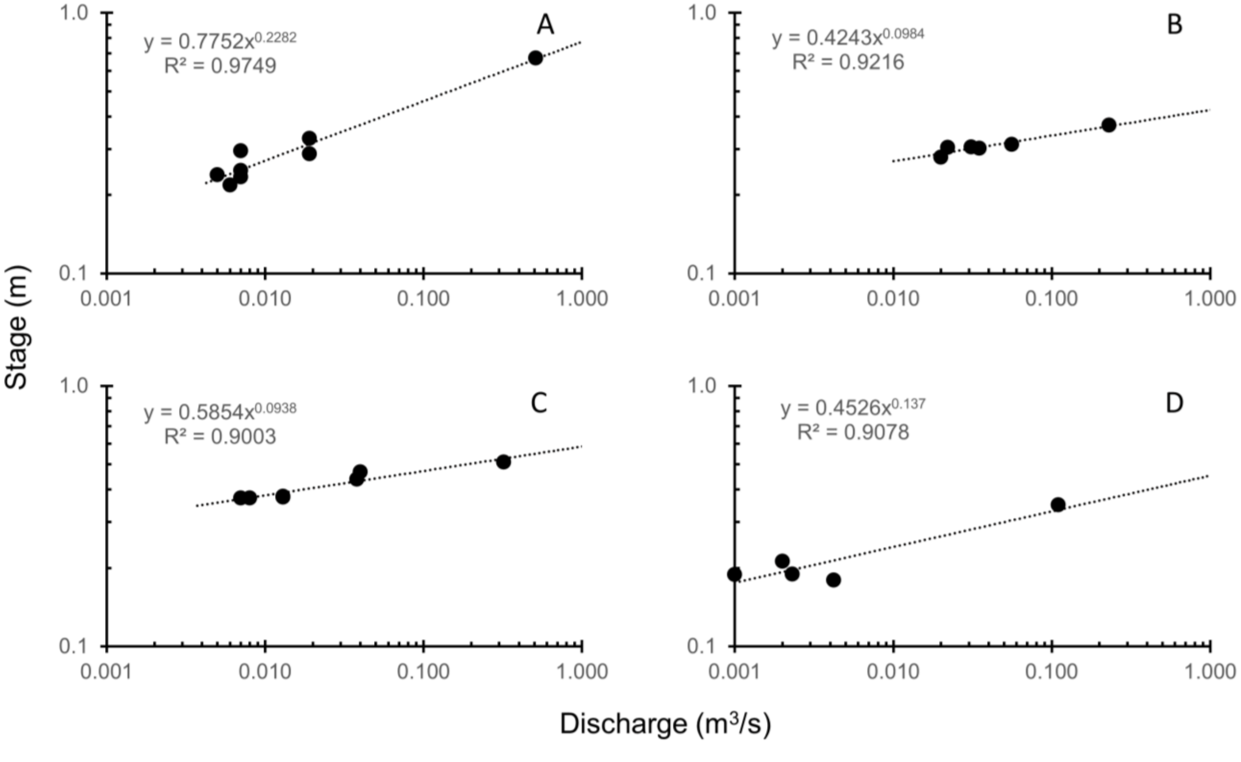

Figure 15. Stage-discharge power curves fitting data from summer and fall of 2019 and 2020 for Stream C1 (A), C1A (B), C2 (C), and C5 (D).

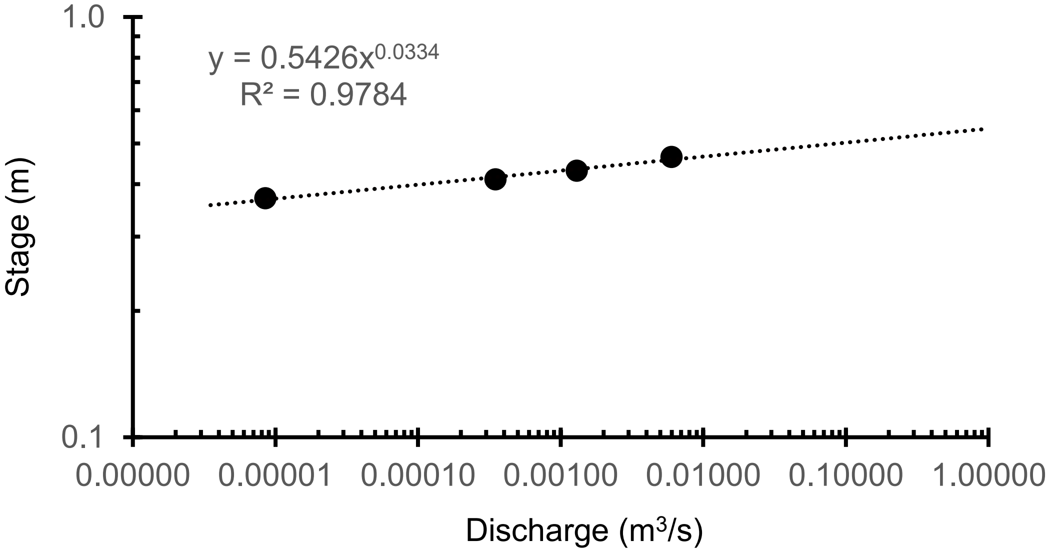

Figure 16. Stream C7 stage-discharge power curve fitting data from summer and fall of 2019 and 2020. Stream C7 discharge measurements were correlated with stage measurements from Stream C5.

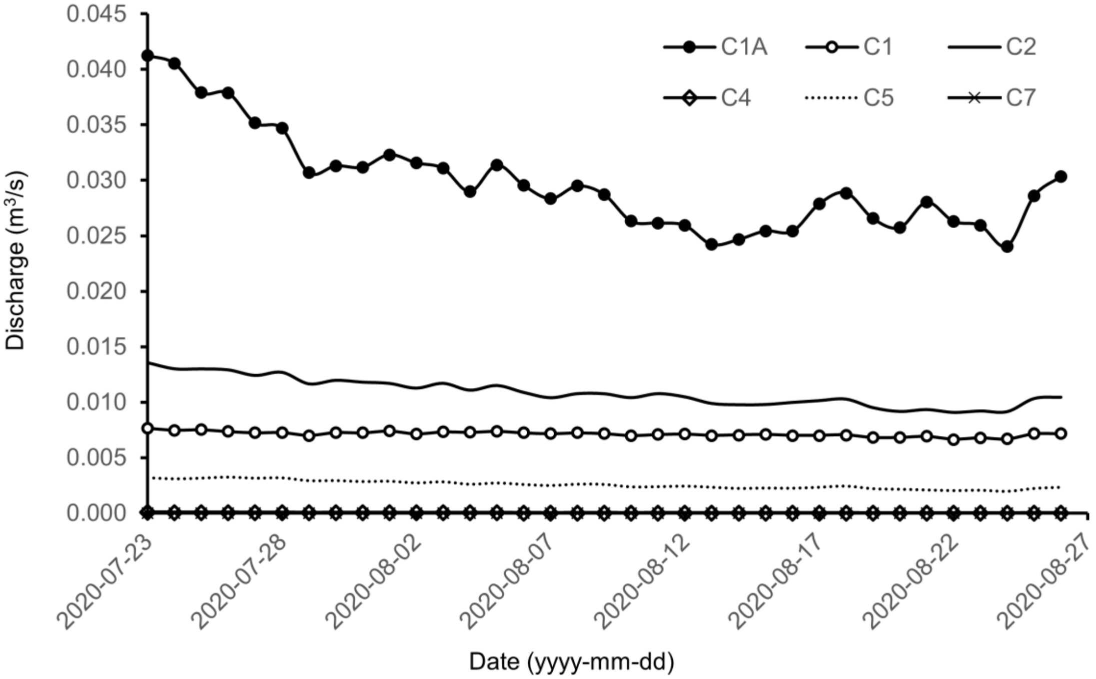

Figure 17. Stream hydrographs of the primary six Kingsboro watershed tributaries discharging to Basin Head Harbour over the 35-day focussed study period (Time zone: UTC-3). Discharge is largely attributed to baseflow over the entire period.

The five stage-discharge relationship curves (i.e., Stream C1, C1A, C2, C5, and C7) were then applied to the hourly records of stage in the respective streams to construct continuous hydrographs for the focussed study period. These hydrographs (Figure 17) were adjusted using a drainage-area ratio to account for downstream watershed areas that were not captured by the gauging stations (Table 10). Following these corrections, the hydrograph for Stream C4 was estimated via the drainage-area ratio method between Stream C7 and C4 (drainage-area ratio = 1.92), based on their comparable flow magnitudes and channel geometry (Figure 17).

Table 10. Drainage-area ratios between the gauged and ungauged watershed area of the monitored streams in the Kingsboro watershed. These ratios were used to correct stream hydrographs for flow contributions made downstream of the gauging station.

	Stream ID				
	C1A	**C1**	**C2**	**C5**	**C7**
Gauged Area (m^2)	3060000	1090000	2550000	819000	567000
Ungauged Area (m^2)	180000	120000	283000	47600	127000
Drainage-Area Ratio	1.06	1.11	1.11	1.06	1.23

It should be considered that this study was conducted during the driest seasonal conditions, during which time the channel flow of Stream C7 and C4 were disproportionately depressed at their sampling locations. With consideration of the low water table, delayed or muted response to rainfall events, high permeability soils, and a thorough literature review, observed streamflows were assumed to be 100% baseflow over the 35-day focussed study period of July 23rd to August 26th, 2020. This simplification precluded the need for baseflow separation and is not anticipated to introduce significant error, as PEI streams have frequently been documented to be 80-100% baseflow during the summer. Furthermore, streams within the KW typically remain below 12°C in the summer, which suggests significant groundwater influence. Calculated streamflows over the 35-day focussed study period are compiled in Table 11. The advective heat flux of the streams to the lagoon were compared to that of the springs and rainfall to assess their relative influence on the heat budget of the lagoon (Table 17).

Table 11. Estimated cumulative streamflow for the six major streams of the Kingsboro watershed over the 35-day focussed study period (2020-07-23 to 2020-08-26) derived from a stage-discharge analysis. Data were rounded to at most 3 significant figures.

	Stream ID					
	C1	**C1A**	**C2**	**C4**	**C5**	**C7**
Total Streamflow (m^3)	21600	90000	32900	164	7740	86
				Grand Total (m^3)		153000

Drive-point piezometer sampling of the Stream C1A streambed appeared to indicate that at least some upper segments of the tributary were perched above the water table in August 2020, as the piezometer was dry beneath the streambed. The sustained flow in losing streams may be the combined result of low conductivity streambed materials, upland wetland storage, discontinuous perched aquifers, and/or transient subsurface aquifer dynamics (Tibbet, 2015).

3.2 Hydrogeological Assessment

3.2.1 Soil-Water Characteristic Curve Analysis

The parameters of a soil-water characteristic curve within SHAW control the soil wetting dynamics and their impact on the hydraulic and thermal properties of the aquifer. This study attempted to estimate these parameters by fitting the Brooks and Corey (1966) model to moisture-retention information available for the Charlottetown soil series of PEI (i.e., Carter, 1987; J. I. MacDougall et al., 1988; see Appendix D for this procedure). The fit of the Brooks and Corey (1966) soil-water characteristic curve was poor across all of the MacDougall et al. (1988) samples (RSR ≥ 0.5), which may be indicative of a systematic error in soil moisture-retention testing. This was reflected in high estimates of air-entry pressure using the log-linear method, which ranged between 3.8 and 8.4 metres. As a result, the parameter estimates based on the curve fitting and the log-linear solution methods that used the MacDougall et al. (1988) data were deemed unreliable.

Conversely, the results of the Carter (1987) dataset were much more reasonable. The observed data for both soil layers in their study were well-represented by the Brooks and Corey (1966) model (RSR ≤ 0.12; e.g., Figure 18), and parameter estimates from both evaluation methods seemed reasonable when compared to literature values. However, the log-linear method appeared to systematically yield higher parameter estimates than the curve fitting approach for both datasets. With consideration of the log-linear approach necessitating a poorly informed estimate of the irreducible water content and a power function regression on poorly resolved data, the curve fitting method was expected to be more reliable. The latter allows the inclusion of more data points for calibration, is likely less impacted by data resolution in the tail region of the log-log plot, and applies the complete formulation of the Brooks and Corey (1966) model.

An average of the properties calculated with the curve-fitting method of the two Carter (1987) soil layers yielded an air-entry pressure (P_b), pore size distribution index (λ), and irreducible water content (S_{irr}) of 8 cm H_2O, 0.23, and 0, respectively. Increased macroporosity of the upper soil layers, the typical underestimation of water retention in laboratory experiments (Healy & Cook, 2002; Meyboom, 1967), and the comparison of test results with literature values (Table 29) suggested that a greater air-entry pressure was warranted. This is further supported by Healy and Cook (2002), who caution the application of unadjusted laboratory water-retention findings. Therefore, the results of the curve fitting method were averaged with the lowest parameter estimates of the log-linear assessment using the Carter (1987) dataset (i.e., $\lambda = 0.33$, $P_b = 33$ cm H_2O, and $S_{irr} = 0$) to increase parameter magnitudes. As a result, the soil parameters $P_b = 16$ cm H_2O, $\lambda = 0.26$, and $S_{irr} = 0$ were assumed in the uncalibrated SHAW model of this study.

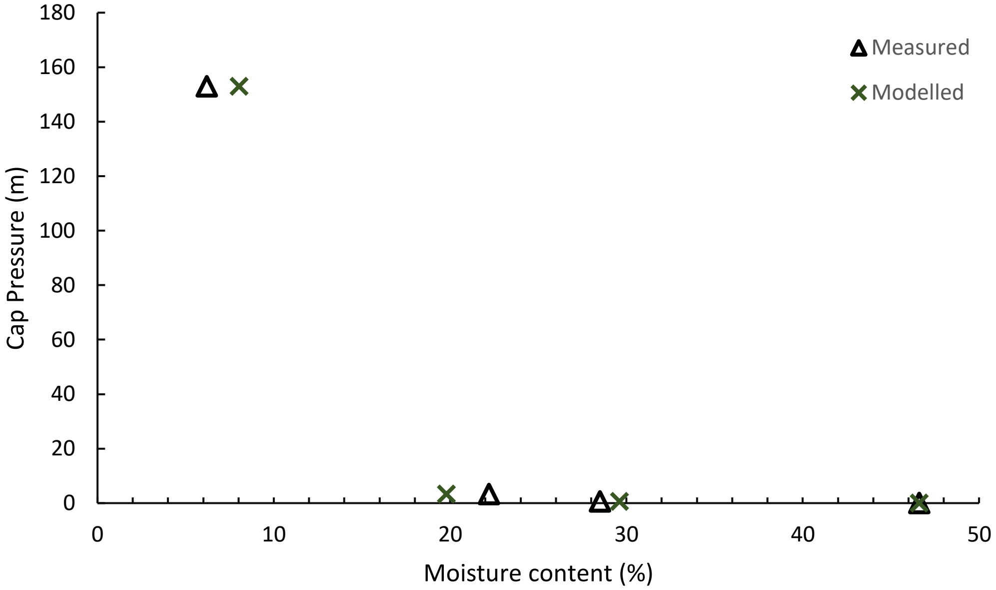

Figure 18. Brooks and Corey (1966) model fitted to the Charlottetown soil series moisture-retention data from Carter (1987). The model reproduced the measured data from Carter (1987) reasonably well (RSR = 0.11; refer to the list of abbreviations for the definition of RSR).

3.2.2 Slug Test Analysis

The DalWell responded to the slug test in an overdamped fashion (Figure 19). The curve maintained log-linear behaviour until the well was approximately 95% recovered (R^2=0.99; Figure 20). With consideration of the local weather station data, it is believed that small recharge events account for the minor divergences from linear recovery (Figure 20).

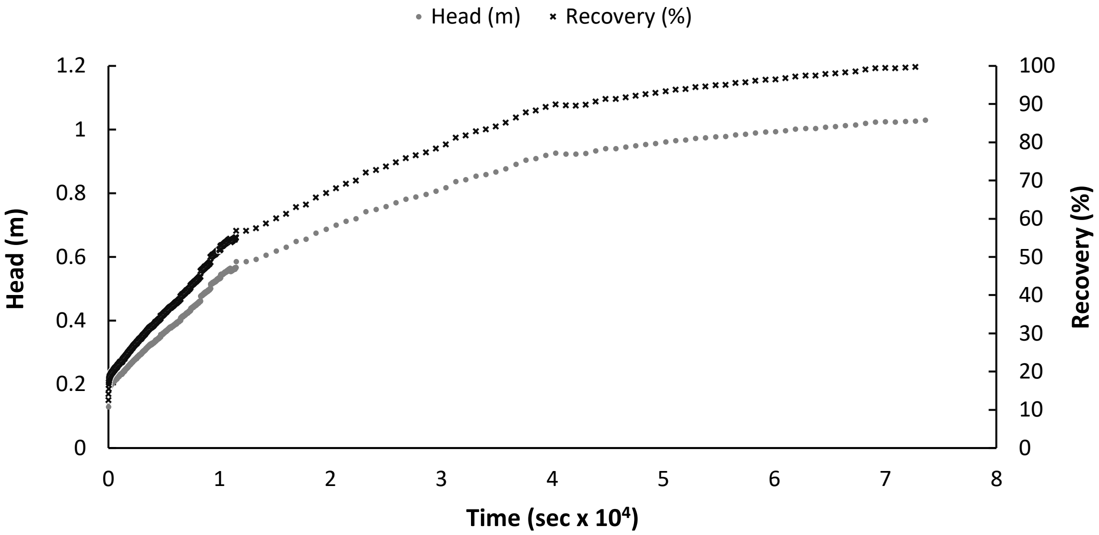

Figure 19. Slug test recovery data, in terms of percent recovered and head (in metres), for the Dalhousie piezometer (DalWell) installed near the coast of the Kingsboro watershed.

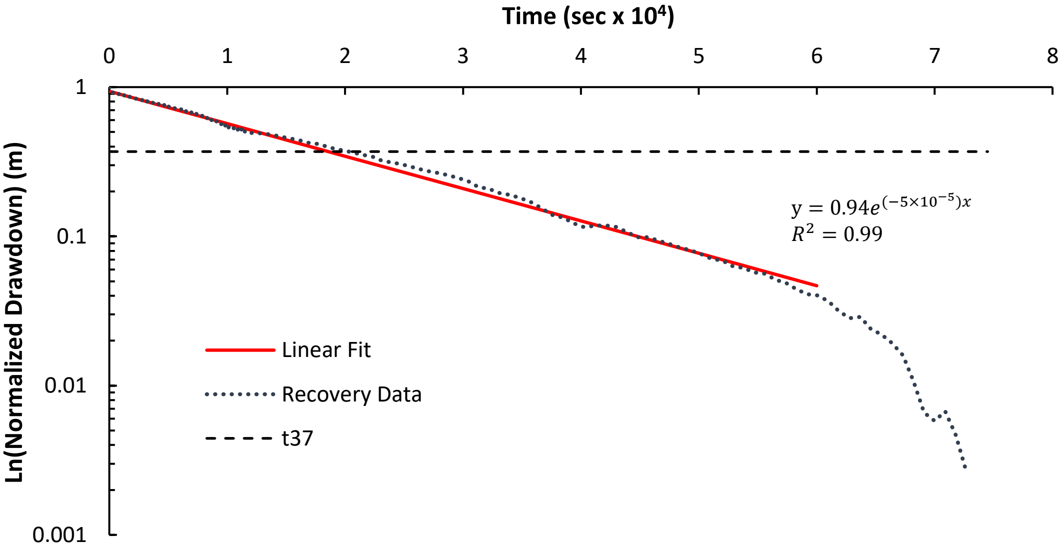

Figure 20. Graphical analysis of the slug test recovery data from the Dalhousie piezometer of the Kingsboro watershed (DalWell) using the Hvorslev slug test method.

The lower bound estimate for the hydraulic conductivity of the surficial soils immediately surrounding the well was estimated as approximately 0.0039 m/day using the Hvorslev (1951) model and 0.00262 m/day using the Bouwer and Rice (1988) model. These estimates are of the same order of magnitude, and they fall within the broad conductivity range proposed for till by Domenico and Schwartz (1990). These values likely underestimate the true hydraulic conductivity of the till in the KW due to partial well development and the heterogeneity of preferential flow paths in the subsurface.

3.2.3 Pumping Test Analysis

Pumping test data from a nearby watershed were analysed to estimate the hydraulic conductivity of the fractured sandstone and mudstone aquifer of the KW. Both the Warren and Root (1963) dual porosity model and the Theis (1935) solution for an ideal confined aquifer effectively modelled the well response data provided by Joostema (2015) for a nearby watershed in PEI (Figure 21).

The models were both used to estimate the bulk hydraulic properties of the screened region of bedrock, the thickness for which was calculated as approximately 76 metres. The Warren and Root (1963) analysis yielded a fracture transmissivity (T_f) of approximately 2000 m^2/day, a fracture storativity (S_f) of approximately 7×10^{-4}, a matrix storativity (S_m) of 6×10^{-3}, an interporosity flow coefficient (λ) of 0.56, and a bulk hydraulic conductivity of 26 m/day. The Theis (1935) analysis yielded a bulk transmissivity (T_{bulk}) of approximately 5000 m^2/day, a bulk aquifer storativity (S_{aq}) of approximately 6×10^{-4}, and a bulk hydraulic conductivity (K) of 64 m/day. Both analyses were done using the MATLAB® toolbox Hytool (Version 2.06; P. Renard, 2017).

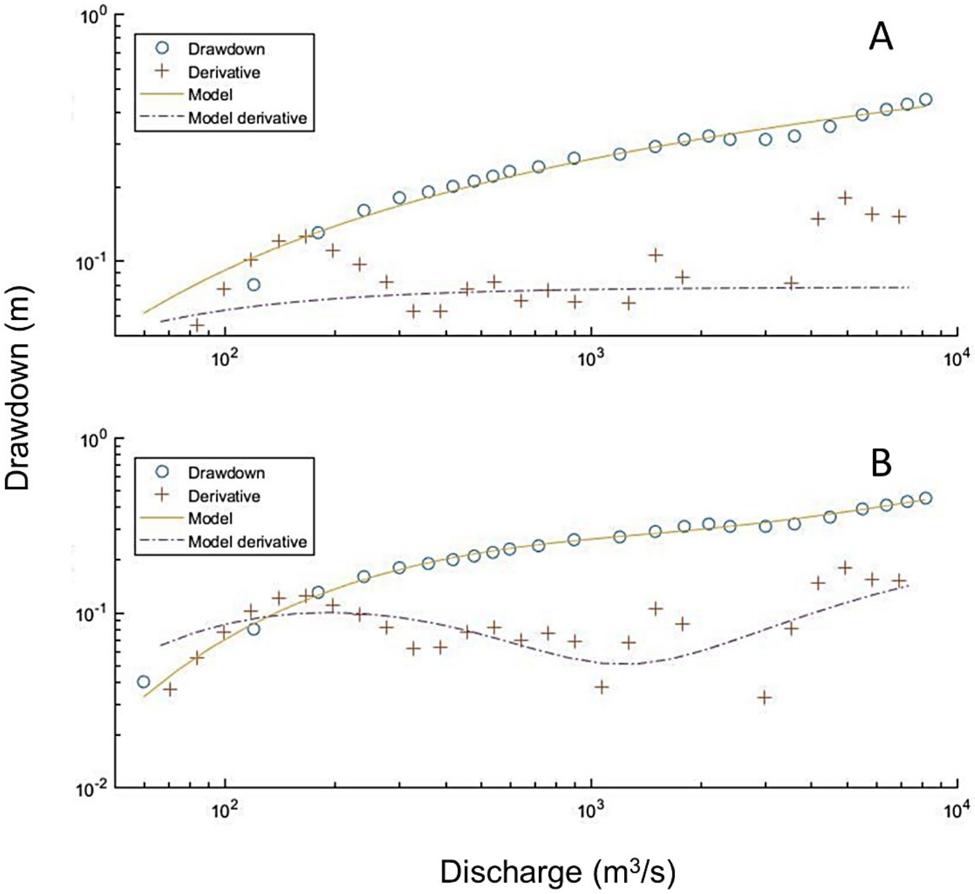

Figure 21. (A) Theis (1935) ideal confined aquifer model applied to the Joostema (2015) well pumping data recorded in Souris, PEI. (B) Warren and Root (1963) dual porosity model applied to the Joostema (2015) well pumping data recorded in Souris, PEI. Curves fitted in the MATLAB® toolbox Hytool developed by Renard (2017).

3.2.4 Specific Capacity Analysis

The result of the semi-analytical method of Thomasson Jr. et al. (1960) and the various selected empirical models are summarised in Table 12. The magnitudes of these hydraulic conductivities should not necessarily be comparable with those estimated by the pumping test, as the sites are approximately 15 km away from one another, the fractures and local low permeability layers of PEI aquifers are highly heterogeneous, the wells are at different altitudes and span different depths, and the test and analysis methodologies are substantially different from one another. The results of all three types of hydraulic tests were considered when parameterising the numerical model of this study.

Table 12. Estimated values of transmissivity and hydraulic conductivity for a Kingsboro private well, given a specific capacity of 122 m^2/day and an aquifer thickness of 33 metres, using various semi-analytical and empirical models.

Model	Transmissivity (m^2/day)	Hydraulic Conductivity (m/day)
Thomasson Jr. et al. (1960), $C_c = 0.5$	61	1.9
Thomasson Jr. et al. (1960), $C_c = 1.0$	122	3.7
Huntley et al. (1992)	35	1.1
El-Naqa (1994)	149	4.5
Mace (1997)	137	4.2

3.3 General Thermal Characterisation

The temperatures measured at stream outlets and their stability reflect a significant degree of groundwater influence over the summer. The median and interquartile range of the stream temperatures from July 26th to August 31st, for both 2019 and 2020, are presented for reference in Table 13. Stream temperature measurements were taken near the discharge points of each of the four largest streams to BHH using Onset HOBO® MX2203 Tidbits. Therefore, these data represent the cumulative result of heating and cooling effects within the stream and are generally representative of the water being delivered to BHH via streams.

Table 13. Stream temperatures (in degrees Celsius) measured in the Kingsboro watershed between July 26th and August 31st for the years 2019 and 2020.

	Year							
	2019				2020			
Stream ID	**C1A**	**C1**	**C2**	**C5**	**C1A**	**C1**	**C2**	**C5**
Median Water Temperature	9.0	10.4	10.8	10.9	8.7	10.8	10.5	10.4
Interquartile Range	0.8	1.3	1.4	1.2	0.6	1.2	1.3	1.0

Stream temperatures are notably lower than lagoon summertime temperatures, which have been measured as low as 7°C (under the direct local influence of a nearby spring) to upwards of 33°C. Five temperature sensors distributed throughout the lagoon yielded an average lagoon water temperature of approximately 22°C during the 2020 focussed period. Temperatures were typically greatest in the shallower and more poorly flushed upper reaches of the NE Arm and lowest in the deeper main basin and lagoon entrance (Figure 22). Daily average water temperatures measured by two lagoon water surface sensors installed during the summers of 2019 and 2020 are graphed along with air temperature to portray the temperature regime of the site over the study period (Figure 22). Average daily entrance temperatures in 2020 are slightly biased towards air temperature, as the sensor would occasionally be exposed to air during particularly low tides. An example of sub-daily water temperature patterns in the Upper NE Arm of the lagoon is found in Figure 27.

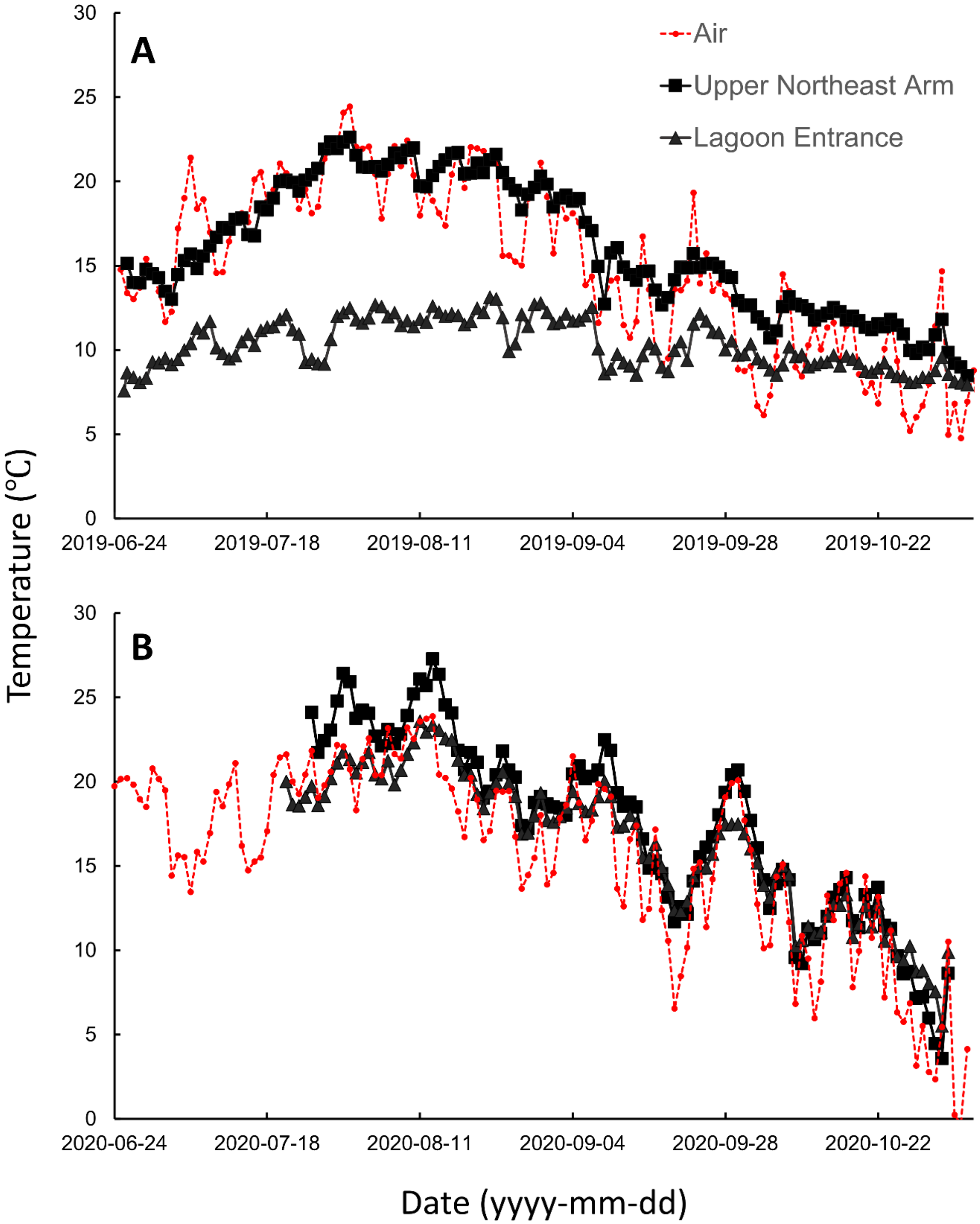

Figure 22. Average daily water temperatures of two locations in the Basin Head lagoon as well as air temperatures over the study period. A and B indicate the 2019 and 2020 data, respectively.

The seasonal air temperature maximum occurred at the beginning of the second week of August. Water temperature is so heterogeneous that it is difficult to say with certainty when/where the hottest conditions occurred; however, our data suggests that peak seasonal lagoon temperatures (and maximum offset from groundwater temperatures) were observed in late July to early August, and diel maximum water temperatures were observed in the afternoons. Lagoon and stream temperatures responded to diel air temperature signals, whereas none of the monitored springs displayed diel temperature trends. The flow of streams appeared mostly insensitive to rainfall, or their responses were significantly lagged during this period of the year, which may be explained by the seasonally depressed water table and highly permeable surficial soils. It is believed that surface runoff is very limited during July and August, except perhaps during extreme rainfall events, and that nearly all water delivered to the streams is in fact groundwater.

3.4 Spring Discharge Assessment

The areas of thirty-four springs were analysed via the TDA approach outlined in Section 2.6 and are summarised in Table 14 and Table 15. The locations of the identified springs are presented in Figure 23 and are further detailed in the associated figures of Appendix A (i.e., Figure 37, Figure 38, and Figure 39). For reference, examples of raw thermal images are presented in Figure 24, and an example of a post-processed image and its associated graphical area analysis are displayed in Figure 25.

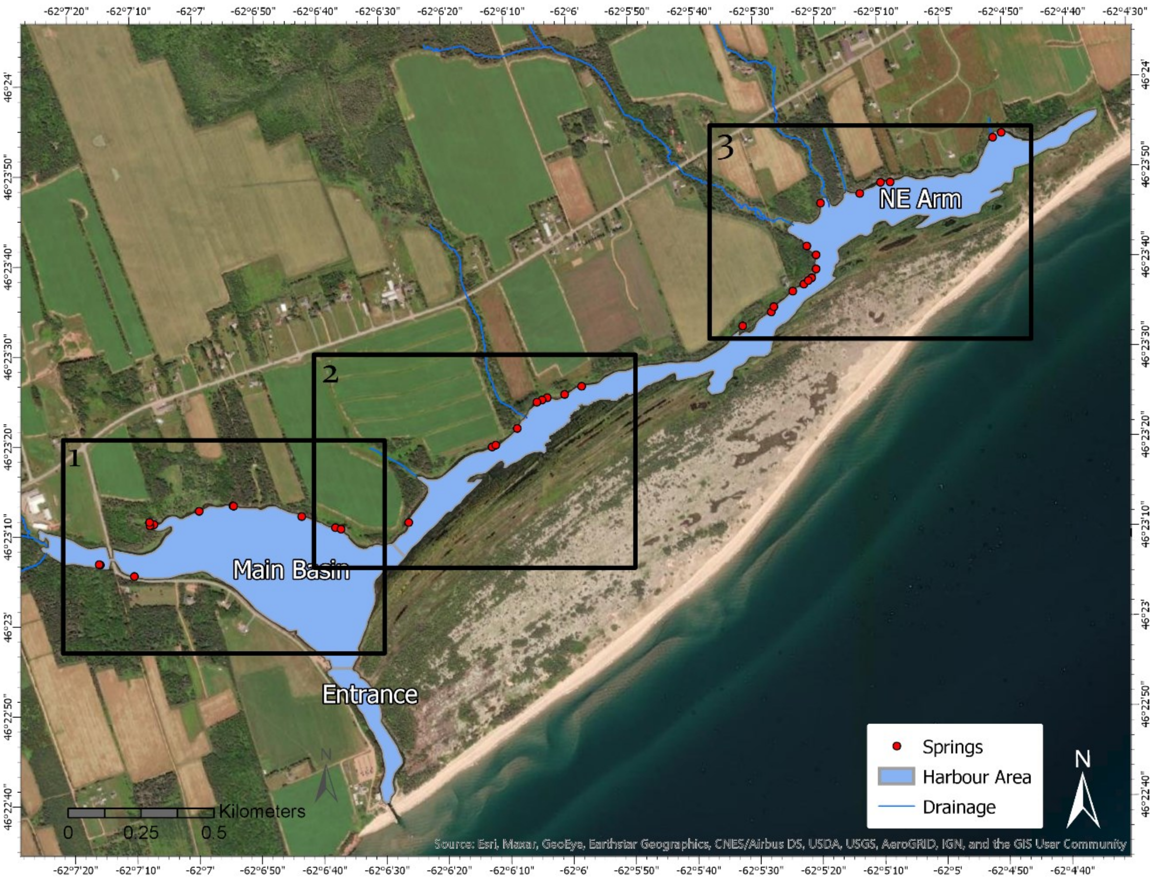

Figure 23. (Series image 1 of 4) Spring locations in Basin Head Harbour. Black boxes each represent an area depicted in subsequent series images that include spring IDs with reference to Table 15 and Table 14. (1) Figure 37, (2) Figure 38, and (3) Figure 39. Map prepared in ArcGIS Pro (Version 2.3.3, 2018).

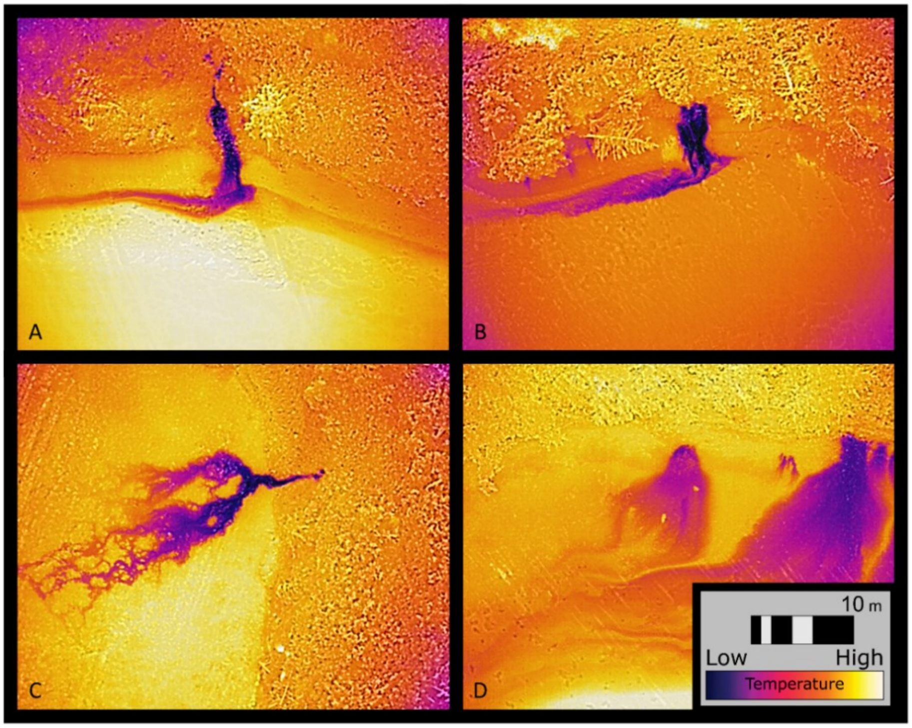

Figure 24. Example thermal images of cold-water plumes associated with springs in Basin Head Harbour. Image extents are 38.4 × 30.7 metres. Springs (A) 14, (B) 12, (C) 8, and (D, left) 9 are displayed.

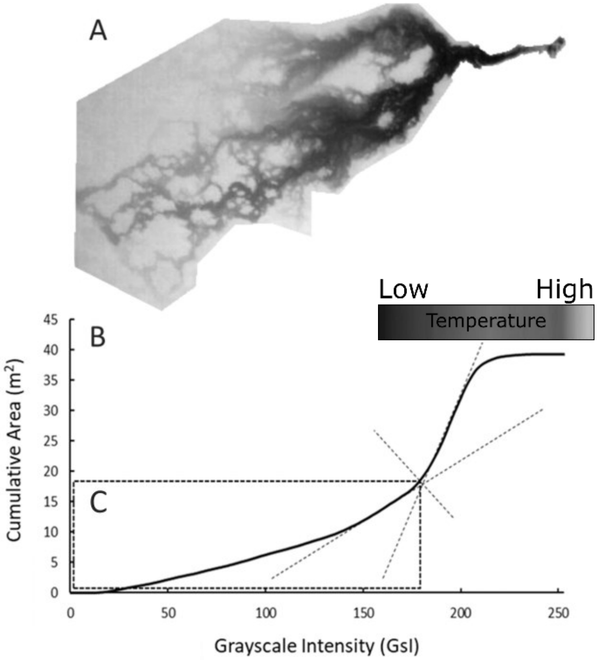

Figure 25. (A) Spring 14 thermal image after post-processing – image is in 8-bit grayscale and cropped to reduce interference (the same spring from Figure 24, panel C). (B) Graphical analysis of (A) grayscale pixel values. (C) Plume area thermal group identified via graphical analysis – plume area of Spring 14 was calculated as 18.3 m^2.

Low-low tide discharge measurements of Spring A, B, and C were paired with images taken shortly (<2 hours) beforehand under comparable hydraulic conditions (Table 14). Measured discharges were corrected for saltwater content based on conductivity and a two-component mixing model. The conductivity of the lagoon varied greatly due to its complex mixing dynamics. Conductivity measurements were as low as 9 mS/cm and as large as 43 mS/cm within the lagoon in 2019 and 2020. A representative estimate of 37.5 mS/cm was used to correct spring discharge measurements for the recirculation of salt water based on sensor data collected near the lagoon entrance while spring discharges were quantified. Conductivity measurements from the DalWell (2020) and the primary tributary (Stream C1A, 2019) were used to estimate the groundwater endmember of the two-component mixing model as 0.16 mS/cm. Data from LTC loggers, installed in two springs while gauging was taking place, were used in combination with discrete measurements of all gauged springs to estimate representative spring conductivity values. The conductivity of gauged springs ranged from 0.48 to 1.1 mS/cm. Ultimately, it was estimated that spring discharges at the times of measurement were <2% saltwater, so this correction had a very minor effect on discharge estimates. This suggests that any saltwater that intrudes into springs and their source aquifer is mostly flushed by low tide.

The local discharge-area data pairs in Table 14 were fitted with a power function (R^2=0.999; Figure 26), which differs from the linear correlation used by Roseen (2002) and the logarithmic correlation used by Danielescu et al. (2009) for similar studies. Instantaneous spring discharge was computed as a function of plume area using this power curve for Springs 1-31 (Table 15). Under the assumption that these few data points are adequately representative of springs throughout the lagoon, it may be expected that this function is representative at the lagoon scale but not at the scale of an individual spring due to the multitudinous controls on plume geometry. Additional volumetric measurements would improve the certainty of this analysis but were not possible in this study due to constraints on time and resources, as well as the challenging field conditions.

A few small plumes within BHH were considered negligible, and photographing certain known plumes was not possible. Non-idealities abounded in the graphical analyses, reflecting that this should be expected and managed systematically. Furthermore, graphical analyses should be guided by the manual inspection of image pixel values to ensure that the plume areas are properly defined. The main causes of non-idealities identified were channel geometry, surface cover, hydrodynamic factors, and thermal interference. The ubiquity of non-idealities reflects the great variety of spring discharge conditions throughout the lagoon. Variation in daily temperatures, water table conditions, and hydrodynamic factors all incorporated uncertainty into the areal analysis of the thermal plumes; however, this uncertainty is anticipated to be acceptable for first-order quantification of focussed groundwater discharge to BHH based on work by Danielescu et al. (2009).

Table 14. Measured discharge-area data pairs from springs within Basin Head Harbour. A trendline was fit to these data pairs for use in the local thermal-discharge assessment. The accuracy of measured discharges was estimated within ±25%. Values rounded to 2 significant figures.

Spring ID	Date/Time (UTC-3)	Area (m^2)	Measured Discharge (m^3/s)
A	22-07-2020 19:35	51	5.2E-04
B	22-07-2020 19:36	10	7.5E-05
C	22-07-2020 19:37	360	3.1E-03

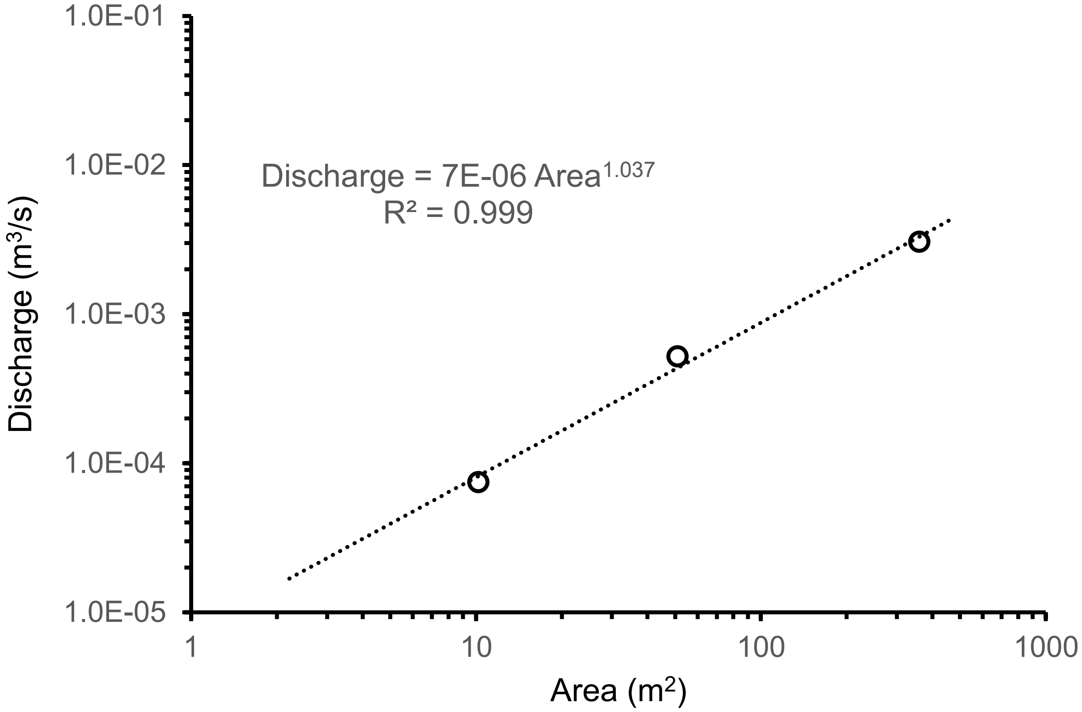

Figure 26. Correlation between summertime spring discharge and spring thermal plume area utilised in the thermal-discharge assessment of Basin Head Harbour, Prince Edward Island.

Table 15. Measured thermal plume areas of 31 springs in Basin Head Harbour over the study period, as well as their estimated instantaneous discharge determined via thermal-discharge assessment. Values rounded to at most three significant figures.

Spring ID	Date/Time	Area (m^2)	Estimated Discharge (m^3/s)
1	29-08-2020 15:27	694	6.2E-03
2	29-08-2020 15:33	360	3.1E-03
3	24-07-2020 19:33	289	2.5E-03
4	22-07-2020 19:36	259	2.2E-03
5	21-07-2020 20:17	171	1.4E-03
6	24-07-2020 18:16	164	1.4E-03
7	24-07-2020 18:16	133	1.1E-03
8	24-07-2020 19:29	115	9.6E-04
9	22-07-2020 19:36	65	5.3E-04
10	21-07-2020 20:15	59	4.8E-04
11	24-07-2020 19:29	57	4.6E-04
12	22-07-2020 17:04	55	4.4E-04
13	24-07-2020 19:30	48	3.9E-04
14	22-07-2020 19:37	48	3.9E-04
15	24-07-2020 19:36	41	3.3E-04
16	24-07-2020 19:31	31	2.5E-04
17	24-07-2020 18:13	25	2.0E-04
18	21-07-2020 20:15	22	1.8E-04
19	24-07-2020 18:18	21	1.6E-04
20	24-07-2020 19:36	15.9	1.2E-04
21	22-07-2020 19:37	13.3	1.0E-04
22	22-07-2020 17:07	12.6	9.7E-05
23	21-07-2020 20:16	11.2	8.6E-05
24	24-07-2020 19:31	9.2	7.0E-05
25	24-07-2020 18:15	7.4	5.6E-05
26	24-07-2020 18:14	6.7	5.1E-05
27	21-07-2020 20:16	3.1	2.3E-05
28	24-07-2020 18:13	2.4	1.7E-05
29	21-07-2020 20:16	2.0	1.4E-05
30	24-07-2020 19:37	1.9	1.4E-05
31	21-07-2020 20:14	1.7	1.2E-05

The instantaneous estimates of spring discharge listed in Table 14 and Table 15 were used to estimate continuous discharge over a 35-day focussed study period by associating them with water table levels in the DalWell and baseflow in the nearest streams via proportionality constants (described in Section 2.6). Assuming streamflow is groundwater-dominated during the summer, one might expect the streamflow and well water level to respond proportionally, resulting in comparable flow estimates for both TDAs in this study. However, the two TDA approaches resulted in substantially different total spring flow estimates from the surveyed springs over the focussed study period. The baseflow proportionality constant yielded a total 35-day cumulative spring flow estimate of 66,000 m^3, whereas the water table method yielded an estimate of 113,000 m^3. Streams within the watershed responded differently to declining water table, so their connectedness to groundwater may be highly variable. In contrast, the DalWell was in a discharge zone immediately adjacent to the springs, and its experience of regional water table decline likely lags that of the upper reaches of the streams. Targeted studies would be required to assess if the baseflow or water table is a better proxy for spring discharge in the KW. At a minimum, numerous distributed wells would be needed in the watershed to make an effective comparison between the two methods; however, the local water table level is suspected to be more closely related to the hydraulic gradient driving coastal discharge.

3.4.1 Spatial Analysis Correction

A spatial analysis was used to develop a spring discharge correction factor by estimating the length of shoreline that was surveyed by the drone relative to coastline that remained unsurveyed. Approximately 5.6 km of the northern and western shoreline were investigated with the drone, whereas 1.4 km were not surveyed due to legal and safety impediments. An additional 4.8 km of southern shoreline along the marsh was excluded from this portion of the analysis, despite being surveyed, as this groundwater input was assumed to be shallower, saltier, more diffuse, and warmer based on preliminary field investigations and the contrasting groundwater flow systems (i.e., coastal wetland versus fractured sandstone and mudstone aquifer). The marsh contributions are certainly relevant to the overarching objectives of this project, but this portion of the watershed is so complex that it would require dedicated study and thus remains open to interpretation. Springs were found at a density of approximately six per kilometre along the surveyed section, which amounted to roughly 330 m^3 of groundwater discharge per kilometre of shoreline per day [m^3/km/day] (3.8 L/s/km) over the focussed study period for the baseflow method and 580 m^3/km/day (6.7 L/s/km) for the water table method. This suggests that approximately 20% of focussed flows on the landward side may have been missed along the 1.4 km of unsurveyed shoreline. The presence of unquantified, relatively large springs in the northwestern marsh has been confirmed, but none have been identified along the entrance channel due to access challenges and rock armouring. Correcting the spring flows to include the focussed flow estimated for the unsurveyed sections of shoreline resulted in a total 35-day flow estimate of 83,000 and 142,000 m^3 for the baseflow and water table TDAs, respectively.

3.4.2 Tidal Head Correction

Spring discharge estimates were subsequently adjusted for the effect of tidal head. The assumed model to account for the effect of tides on springs (Equation 12, Section 2.6) is admittedly simplistic and the effect of the tides on springs requires more dedicated study. That considered, a sample of six springs were monitored over a tidal cycle in July 2020, and their thermal plume areas were measured at high-high and low-low tide to compute a generalised tidal correction factor (C_{tidal}) for BHH using Equation 12. The result of this assessment was a C_{tidal} of 0.5, which suggests that spring discharge stopped at high-high tide; however, there was evidence of certain springs that continued to discharge in a reduced capacity at high-high tide in BHH, despite minimal evidence of discharge via TIR sensing. In addition, the discharge from certain springs appeared unaffected by tides for a prolonged period spanning low tide conditions. Various tidal correction factors were tested and the resulting flows for both TDAs were compiled in Table 16. As informed by field observations (e.g., handheld and remote temperature and conductivity measurements, and drone-assisted TIR surveys), an average C_{tidal} is believed to be above 0.75 for BHH, though hard evidence is limited at this time. The C_{tidal} of individual springs is expected to be highly variable; however, it is estimated that focussed intertidal springs contributed between 60,000 and 130,000 m^3 over the 35-day study period.

Table 16. Compiled spring flow values of Basin Head Harbour for the 35-day focussed study period. Estimates are tabulated by tidal correction factor (C_{tidal}) and thermal-discharge assessment (TDA) method. The TDAs involved either using baseflow (BF) or water table (WT) as a proxy for spring discharge. Data rounded to three significant figures.

	TDA Method	
C_{tidal}	**BF (m^3)**	**WT (m^3)**
0.5	41400	70800
0.75	62000	106000
1	82700	142000

3.5 Investigation of Spring Temperatures

The thermal patterns of three springs were analysed to estimate their signal properties, relative depths, and by extension their relative vulnerability to climate warming. In addition, the temperatures of these springs were compared to lagoon water temperature to discuss the local thermal influence of springs. Spring 5 (location shown in Figure 39, Appendix A) water temperature was monitored during the summer and fall of 2019 and 2020 (Figure 27 and A, Figure 28). Conversely, Spring 2 and 21 (locations shown in Figure 37 and Figure 38, Appendix A) water temperatures were only monitored during the summer and fall of 2020 (B and C, Figure 28).

The spring water temperatures discharging from the north shore of BHH were measured between 7 and 10°C during the summer months. The respective temperature signatures of springs are indicative of the depth of, and thermal controls on, the groundwater from which the springs originated. Lagoon water temperatures were consistently lowered surrounding spring outlets, as illustrated by Figure 27. However, the local water temperatures surrounding all springs varied substantially with the tidal signal, reaching relatively high temperatures at high tide and groundwater temperatures at low tide.

The temperature signatures of springs may theoretically be used to infer the subsurface depth of the groundwater delivered to the spring via thermal modelling. The lowest local minima of the Spring 5 temperature data are indicative of groundwater temperature (i.e., ~7.65°C; A, Figure 28). The lack of periodicity in the Spring 5 signal (i.e., no seasonal harmonic signal is apparent; A, Figure 28) suggests that its source depth is below the influence of seasonal air temperature patterns. Unlike Spring 5, Springs 21 (B, Figure 28) displayed a seasonal signal. The minima reflecting the groundwater temperature were manually fitted with an idealised seasonal temperature signal to estimate the parameters of the annual sinusoid. The seasonal signal of Spring 21 had an annual average temperature of approximately 7.75°C and an annual range of about 3.2°C. This substantial range indicates that the source depth is much shallower than Spring 5. However, the overall temperature variation at its outlet is lower than Spring 5, probably because this area of the channel gets more flushing and is deeper than the upper NE Arm.

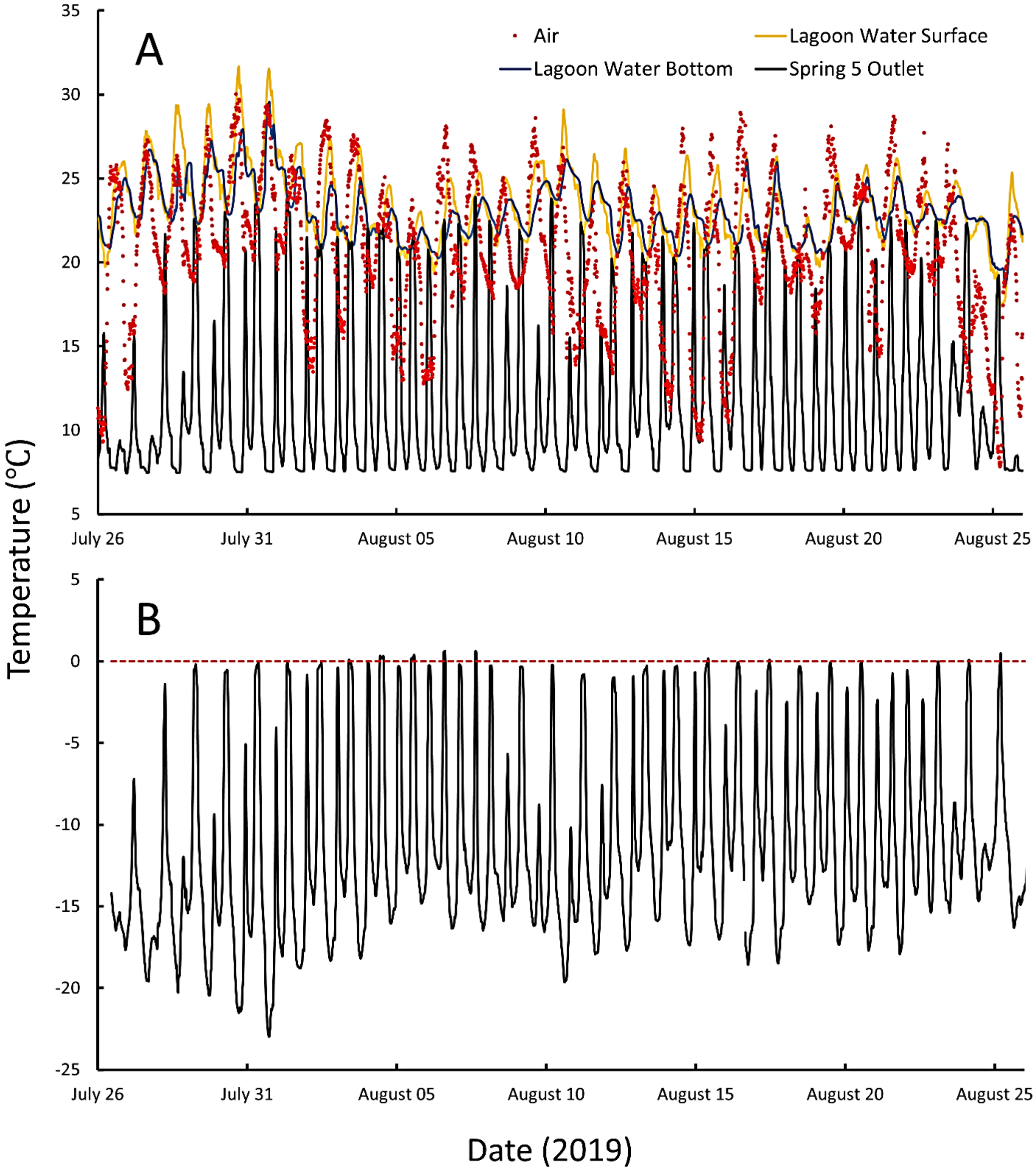

Figure 27. Temperature data from the Basin Head Harbour 2019 field investigations. (A) Paired lagoon water temperature sensors (one floating beneath the surface and the other at the channel bottom) were in the upper-northeast arm, within 30 metres of the Spring 5 temperature logger. Conversely, air temperature was collected by a remote weather station installed near the centre of the lagoon (see Figure 7 for device locations). (B) Difference between the average temperature of the sensor pair of (A) in the upper-northeast arm and Spring 5. Spring 5 temperatures are typically more than 10℃ colder than the lagoon water during the months of July and August (i.e., the period of highest thermal contrast). The red line is the threshold above which the sensor in the spring outlet is warmer than the channel.

Spring 2 is in the deeper main basin, which is apparent because the peak temperatures remain much lower over the summer, and it also displayed a seasonal signal (B, Figure 28). Although the average temperature of Spring 2 was coldest, at approximately 7.05°C, its seasonal signal was most pronounced with an annual range of approximately 4°C. This suggests that it has the shallowest source water depth of the three springs, all other controls assumed equal. However, differences in subsurface materials, watershed land cover, flow paths, and land use all influenced the patterns observed in these springs.

The reviewed data suggest that at least some of the springs are sensitive to seasonal air temperature changes. It follows that springs responsive to seasonal signals are almost certainly susceptible to the multidecadal temperature signals induced by climate change. Warming of groundwater, and thus springs and groundwater-dependent streams, could possibly have consequences for thermally vulnerable species, as mixing of groundwater into the lagoon results in lower summertime water temperatures at least locally within the lagoon (e.g., Figure 27). The significance of springs on local water temperature necessitates further study; however, the interaction of tidal stage and spring plume dynamics was explored in an associated work (KarisAllen & Kurylyk, 2021). A negative correlation between spring plume area and tidal stage has been observed, as described by (Lee et al., 2016). A greater understanding of these discharge dynamics may be valuable for characterising ecological thermal controls and quantifying nutrient delivery to PEI coastal systems via groundwater. Additional interpretations of the spring temperature data of this section are included in Appendix B, Section 4.

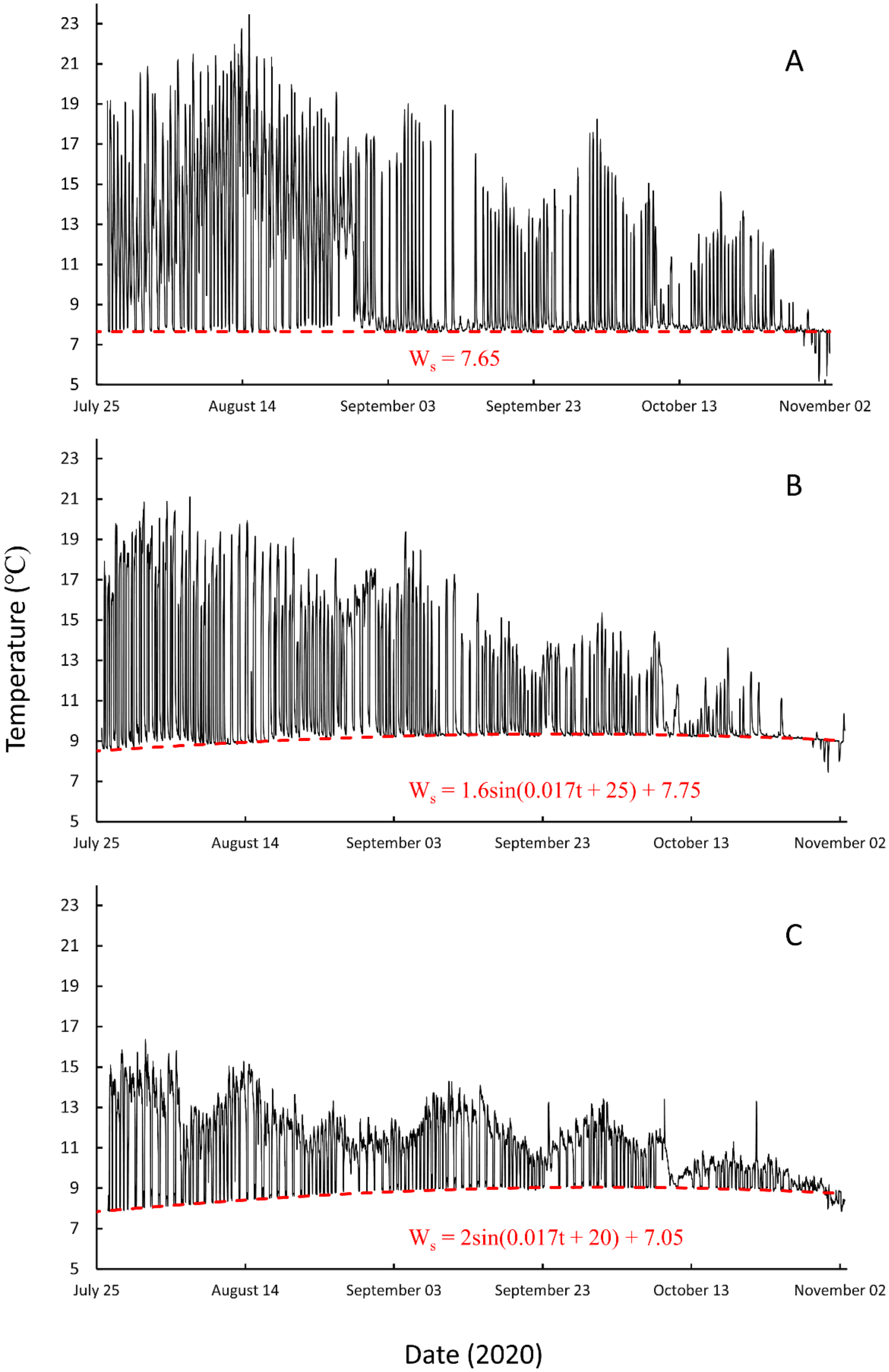

Figure 28. (A) Spring 5, (B) Spring 21, and (C) Spring 2 temperature data from the Basin Head Harbour 2020 field investigations. The annual temperature waveform (W_s; in red) has a distinguishable amplitude in Spring 21 and 2 but not in Spring 5. Groundwater temperatures begin to exceed lagoon water temperatures at the end of October. W_s = annual temperature waveform and t = time in days.

3.6 Lagoon Heat Budget Analysis

Five components of the Basin Head lagoon heat budget were estimated in this study over the 35-day focussed study period: the net advective heat from springs, rainfall, and streams, as well as the net shortwave and longwave radiative heat transferred into and from the lagoon, respectively (Table 17). Local shortwave radiation and rainfall measurements for the focussed study period were used in the lagoon heat budget analysis (Figure 29).

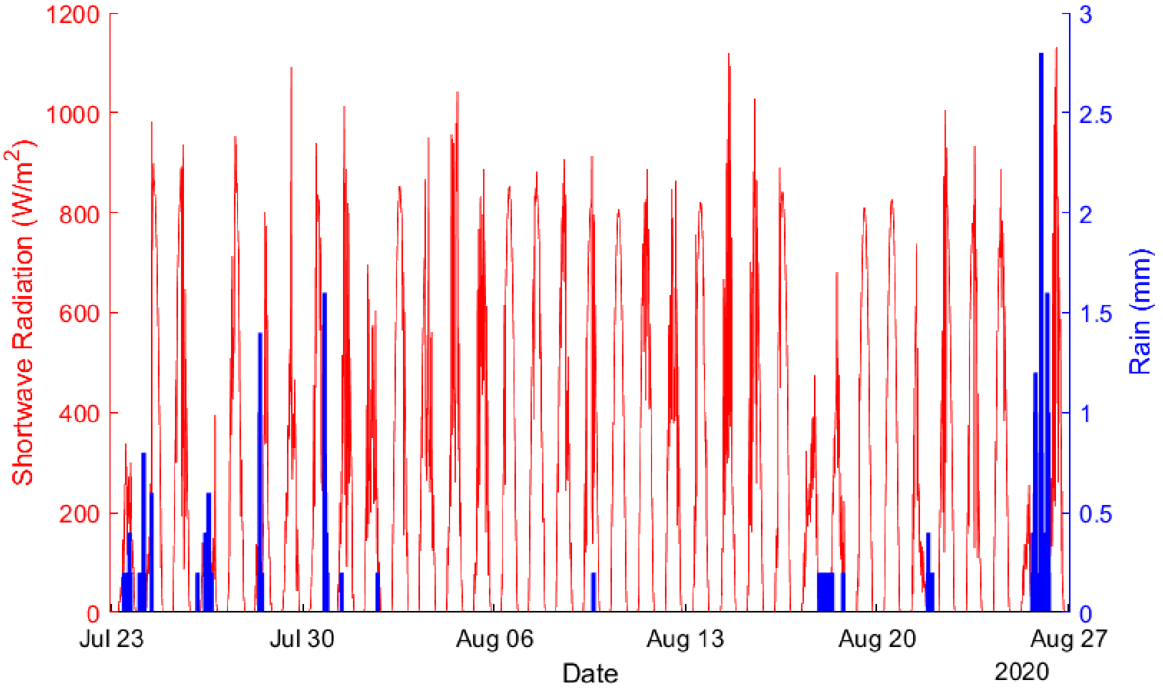

Figure 29. Local solar radiation (red) and rainfall data (blue) for Basin Head Harbour over the focussed study period of July 23 to August 26th, 2020. Data were collected at a 15-minute resolution using an Onset HOBO® weather station located near the centre of the lagoon (see Figure 7 for station location).

Two estimates of spring discharge to the lagoon were made in this study, resulting in a "low" and "high" estimate of the net advective heat associated with them. Although net advective heat components increased the heat stored in the lagoon, they all cooled the lagoon water temperature over the summer (as indicated by their negative value in Table 17). As expected, radiative heat components were substantially larger than advective heat components to the lagoon. Considering the uncertainty associated with the discharge measurements of this study, heat contributions from springs and streams may be considered of comparable magnitude. However, diffuse groundwater input would further increase the relative contribution of direct groundwater on the heat budget of the lagoon.

Table 17. Basin Head lagoon heat fluxes associated with three advective processes and two radiative processes over the 35-day focussed study period. Positive values indicate an addition of energy to the lagoon.

Heat Budget Component	35-day Net Heat Contribution (Joules)
Springs (low)	-3.51×10^{12}
Springs (high)	-7.60×10^{12}
Streams	-7.67×10^{12}
Rainfall	-2.76×10^{11}
Downward shortwave radiation	3.89×10^{14}
Emitted longwave radiation	-7.09×10^{14}

3.7 SHAW Modelling

3.7.1 Model Sensitivity Analysis

A high-level sensitivity analysis was conducted on model parameters and design elements that were highly uncertain and expected to affect the calibration targets. This assessment focussed on the calibration performance, and by extension the thermal control parameters of the model. The estimated likely range of each of the model parameters/elements listed in Table 18 were tested one at a time. To reflect the high degree of uncertainty involved in this modelling process, only relative qualitative indicators of sensitivity were used for the tested parameters (i.e., low [L], medium [M], and high [H] sensitivity) based on the magnitude of their influence on calibration performance over their expected range (i.e., how much they changed the subsurface temperatures of the domain). Given the physical complexity of the model and the resulting interdependence of certain variables, an automated process may improve the accuracy of the sensitivity analysis results by assessing the complete range of each parameter and parameter combinations with a defined performance metric. Values that were assumed as default/average in the model were not included as there was inadequate information to adjust them (e.g., plant canopy and albedo parameters). The model parameters and elements investigated, as well as their relative sensitivity over the ranges tested, are listed in Table 18.

Table 18. Qualitative, relative attribution of sensitivity to SHAW model input parameters. Letters indicate low (L), medium (M), and high (H) model sensitivity to the respective parameter.

Model Parameter/Element	Sensitivity
Residue Layer	H
Lower Boundary Temperature	H
Lower Boundary Depth	M
Snow/Rain Threshold	M
Water Table Depth	M
Shallow Organic Content	L
Initial Domain Temperatures	L
Soil Compositions	L
Soil Porosity	L
Soil Density	L

Of the parameters/elements tested (Table 18), the inclusion of a residue layer and the lower boundary temperature had the greatest influence on subsurface temperatures and calibration performance. The remaining factors considered had less significant impacts individually on subsurface temperatures but were collectively leveraged to improve the calibration of the historical simulation.

3.7.2 Model Calibration & Limitations

Groundwater level and temperature data (2019-2020) were collected in an upland and lowland well to guide modelling efforts. Important values for each well are compiled in Table 19 for reference. These values were only regarded as rough approximations of field conditions for the historical simulation period of the model as they are developed from relatively short-term datasets.

Table 19. Important parameters for the two groundwater wells utilised for the calibration/parameterisation of a SHAW 1D thermal models of Basin Head Harbour. The values of the bottom three rows were calculated from the analysis of historical well data. MASL = metres above sea level.

	Well Owner	
	Dalhousie University	**Government of PEI**
Well ID	DalWell	PEIGov Well
Location (Lat; Long)	46.38934°N; 62.10207°W	46.4000°N; 62.2500°W
Ground Elevation (MASL)	5	55
Years of Record	2019-2020	2019-2020
Well Type	Piezometer	Observation Well
Well Diameter (in)	1	Unknown
Sensor Type	Onset HOBO U20-001-01	Solinst Levelogger Gold
Sensor Depth (m)	4.24	13.67
Average Annual Temperature (℃)	7.14	7.22
Amplitude of the Annual Temperature Signal (℃)	2	0.16
Average Annual Depth to Water Table (m)	2	7

The calibration targets for the SHAW model were subsurface temperatures as measured in the wells, as well as the amplitude and lag of the annual temperature subsurface signal in comparison to the annual air temperature signal, as summarized in Table 20. These value ranges are approximated through the analysis of the data from the DalWell and PEIGov

Well (Government of PEI, 2021). The DalWell was used as the calibration target for the lowland domain (water table depth of 3 m), whereas the PEIGov Well was mainly used to guide the upland domain (water table depth of 7 m).

Table 20. Thermal calibration targets for the site's SHAW model that were derived from two wells within or near to the Kingsboro watershed. DalWell is in a lowland discharge area, whereas PEIGov Well is in an upland recharge zone with a relatively deeper water table.

Well ID	Depth (m)	Temperatures (℃)	Amplitude (℃)	Lag (days)
DalWell	4.24	5.10 - 9.50	1.80 - 2.20	70 - 100
PEIGov Well	13.67	7.075 - 7.45	0.11 - 0.18	230 - 245

The calibration targets in Table 20 were developed from 1- to 2-year datasets, and significant interannual variability is expected at these depths based on other available data. Thus, these should be considered only as approximate guidelines for model calibration, as the historical range of values at these depths is likely much larger than reflected by these calibration targets.

The calibrated outputs of the lowland and upland baseline simulations at approximately 4.24 and 13.67 metres are compiled in Table 21. The range of average annual temperatures, as well as the amplitude and lag of the thermal signal at each depth were calculated using the final 5 years of the baseline simulations (i.e., 2016-2020).

Table 21. Calibrated outputs of the lowland lower domain (3 m water table depth) for both calibration depths of the baseline simulation and upland lower domain (7 m water table depth) baseline simulation. Calibration targets are found within Table 20.

Domain	Depth (m)	Average Annual Temperatures (℃)	Amplitude (℃)	Lag (days)
Lowland	4.2	7.45 – 7.80	2.10 – 2.20	92-105
Lowland	13.88	7.61 – 7.63	0.05 – 0.10	280-310
Upland	13.24	6.91 - 6.99	0.05 – 0.10	270-296

Various adjustments were made to the model domain and parameterisation through manual calibration. Although there are likely significant residue layers throughout the KW, the residue module within SHAW (as parameterised) increased subsurface temperatures unreasonably and may not effectively represent the study site. Therefore, the residue layer was entirely removed, as it substantially reduced calibration performance. Instead, the organic content in the shallow soil nodes was increased to reflect the influence of an organic-rich upper layer on subsurface temperatures, preserving the conceptualisation of the study site and improving calibration performance. The soil compositions, densities, and porosities of the domain were also changed slightly, as well as the snow-rain threshold, to improve the calibration. The shallow water table domain was lowered from 2 to 3 metres. This adjustment was justified by the improved calibration performance and field data suggesting that the DalWell was behaving as a piezometer occasionally experiencing partial confinement.

The many iterations of the model domain, soil stratigraphy, initial conditions and boundary conditions that were initially investigated to settle on the parameterisation communicated in this thesis will not be reviewed in detail for succinctness. The calibration of other model parameters (e.g., albedo and plant canopy) could improve agreement with the calibration targets, as well as the automation of the calibration process based on performance metrics. Considering the data deficit, the uncertainty regarding the calibration targets, solution equifinality, and the modelling objectives, the resulting calibration was deemed satisfactory to proceed with the investigation of future spring temperatures.

Several limitations of the model should be acknowledged to guide the interpretation and application of modelling results. The calibrated model appears to exaggerate the attenuation of the amplitude and lag of the annual signal in the subsurface when compared with field data, which will influence future simulation results. Furthermore, the average annual temperatures of the simulations may be higher than reality in the lowland domain and less than reality in the upland domain, although this discrepancy appears to be within 0.5°C. Adjustments to the surface domain to reduce the temperature of the lower lowland domain further reduced temperatures in the lower upland domain, so a compromise was made to balance the error of both domains, rather than prioritizing one over the other. One explanation for the disjoint between the two models may be that one dataset was from a discharge zone in the watershed and the other was from a recharge zone, and these may be expected to have different subsurface thermal regimes (Bense & Kurylyk, 2017; Dong et al., 2018). Differences in the modelled and observed temperatures may be the result of advective (or other) processes inadequately captured by this modelling framework. For example, this 1D model does not account for preferential fracture flow or the horizontal convolution of thermal signals (Kurylyk et al., 2015).

Certainly, the lack of field data to constrain model parameters made the issue of equifinality pronounced during calibration. Furthermore, the 3D system is heterogenous, involving many nuances that cannot be captured in a 1D model (e.g., snow drift, land-use and cover variability, soil and fractures heterogeneity, and flow routing). Given the data deficit, the heterogeneity of till depth was not explicitly considered by the model but is probably shallower in upland regions relative to the lowland regions (Francis, 1989).

Additional sources of uncertainty throughout the modelling process abounded. The DalWell is in a discharge zone and could be partially confined by the overlying till during high water table conditions, which may result in an overestimation of the true water table height (this was adjusted for during the calibration). Due to the well installation being between a piezometer and observation well, it is difficult to confidently interpret its response to its environment; however, field data suggest that it is operating more as a piezometer and is partially confined, suggesting that the water table is deeper than well water level measurements implied. Separately, the upland PEIGov Well had QA/QC problems that were dealt with as comprehensively as possible but may still introduce error.

Advective and horizontal heat transport were simplified drastically in this model due to perceived instability issues. Instability challenges were avoided by using two communicating domains, with a simplified lower domain, at the cost of calculating advective heat and water transport below the water table. Additionally, the stable average water table imposed in the lower domains may inadequately capture the interplay between seasonal heat fluxes and water table levels. Furthermore, SHAW did not allow for direct control over various important thermal properties. Instead, soil thermal properties are defined based on functions using soil composition, limiting the flexibility of the manual sensitivity analysis and calibration process.

As always with groundwater modelling, this is a simplified mathematical representation of a complex natural system. The goal here was never to recreate the system, but to approach a model that represented an idealised system that responded to forcing comparably to the system in question. It is believed that this objective was reasonably achieved. A more comprehensive modelling study is appropriate to reduce uncertainty;

however, this modelling effort made use of the information and resources currently available for the site.

3.7.3 Model Results

The final 5 years of the future simulations (2096-2100) were compiled and compared to the final 5 years of the baseline (historical) simulation (2016-2020). The results for the lowland and upland model domains are presented in Table 22. The subsurface temperatures at ~4.24 and ~13.67 metres were projected to increase with increasing surface temperatures in all simulations. Groundwater temperature is projected to increase by 0.08-2.23℃ at ~4.24 metres and 0.32-1.42℃ at ~13.67 metres. The modelled temperatures of the baseline and future lowland simulations are depicted in Figure 31 for reference. If these projected groundwater temperature changes are experienced by the springs and streams discharging to BHH, the impacts could range from ecologically insignificant to potentially very harmful when considering resident heat-sensitive species.

Table 22. Subsurface temperatures of the future SHAW simulations of the lowland (3 m water table depth) and upland (7 m water table depth) lower domains. GCM = Global Circulation Model; RCP = Representative Concentration Pathway.

Domain	GCM	RCP	Depth (m)	Average Annual Temperatures (℃)	Projected Change (℃)[a]
Lowland	CNRM-CR5	Historic	4.2	7.45 – 7.80	NA
Lowland	CNRM-CR5	4.5	4.2	7.88 – 8.45	0.08 – 1.00
Lowland	CNRM-CR5	8.5	4.2	8.59 – 9.62	0.79 – 2.17
Lowland	MRI-CGCM3	4.5	4.2	7.90 – 8.61	0.10 – 1.16
Lowland	MRI-CGCM3	8.5	4.2	9.13 – 9.68	1.33 – 2.23
Lowland	CNRM-CR5	Historic	13.88	7.61 – 7.63	NA
Lowland	CNRM-CR5	4.5	13.88	8.26 – 8.41	0.63 – 0.80
Lowland	CNRM-CR5	8.5	13.88	8.79 – 9.03	1.16 – 1.42
Lowland	MRI-CGCM3	4.5	13.88	8.08 – 8.25	0.45 – 0.64
Lowland	MRI-CGCM3	8.5	13.88	9.14 – 9.23	1.51 – 1.62
Upland	CNRM-CR5	Historic	13.24	6.91 – 6.99	NA
Upland	CNRM-CR5	4.5	13.24	7.31 – 7.45	0.32 – 0.54
Upland	CNRM-CR5	8.5	13.24	7.66 – 7.90	0.67 – 0.99
Upland	MRI-CGCM3	4.5	13.24	7.23 – 7.38	0.24 – 0.47
Upland	MRI-CGCM3	8.5	13.24	7.92 – 8.02	0.93 – 1.11

[a] *The projected temperature change was calculated by comparing the last five years of the future simulation with respect to the last five years of the baseline (historic) simulation. As with the calibration, the lowland calibration depth was above 7 m and is therefore not present in the upland lower domain.*

The amplitudes of the annual thermal signals of the monitored springs suggest that some springs will be more sensitive than others to surficial warming. The atmospheric forcing and subsurface temperature response over the last five years (2016-2020) of the lowland baseline simulation are presented to exemplify the intra-annual variability of temperature, signal attenuation, and how model signals may be matched to the measured spring temperature data (Figure 30). The amplitude of the annual temperature signals of the baseline simulations may be compared to spring outlet thermal patterns (Figure 28) to make a rough estimation of their source depths. Springs 2 and 21 are likely between 3 and 7 metres deep, whereas Spring 5 is likely below 12 metres. The overall distribution of spring source depths would need to be further explored to assess how sensitive groundwater inputs to BHH may be at the lagoon scale, but this preliminary information is valuable to understand the present/future system and to inform future research and management initiatives in the area.

The notion of diverse spring thermal sensitivities is further supported by comparing the warming rates of subsurface temperature at different depths within the soil column. For example, 5-year averaged air temperature is simulated to increase by approximately 4.32°C over the future period of the warmest simulation (i.e., MRI-CGCM3, RCP8.5 from 2020 to 2100). This air temperature signal increased the 5-year averaged subsurface temperature by approximately 1.78°C at 4.2 metres depth and 1.57°C at 13.88 metres depth. For relative comparison, this suggests a relative warming rate of 0.41°C at 4.2 metres depth and 0.36°C at 13.88 metres depth per 1°C of air temperature increase by the year 2100. This example demonstrates that deeper springs will take longer to respond to downward thermal forcing.

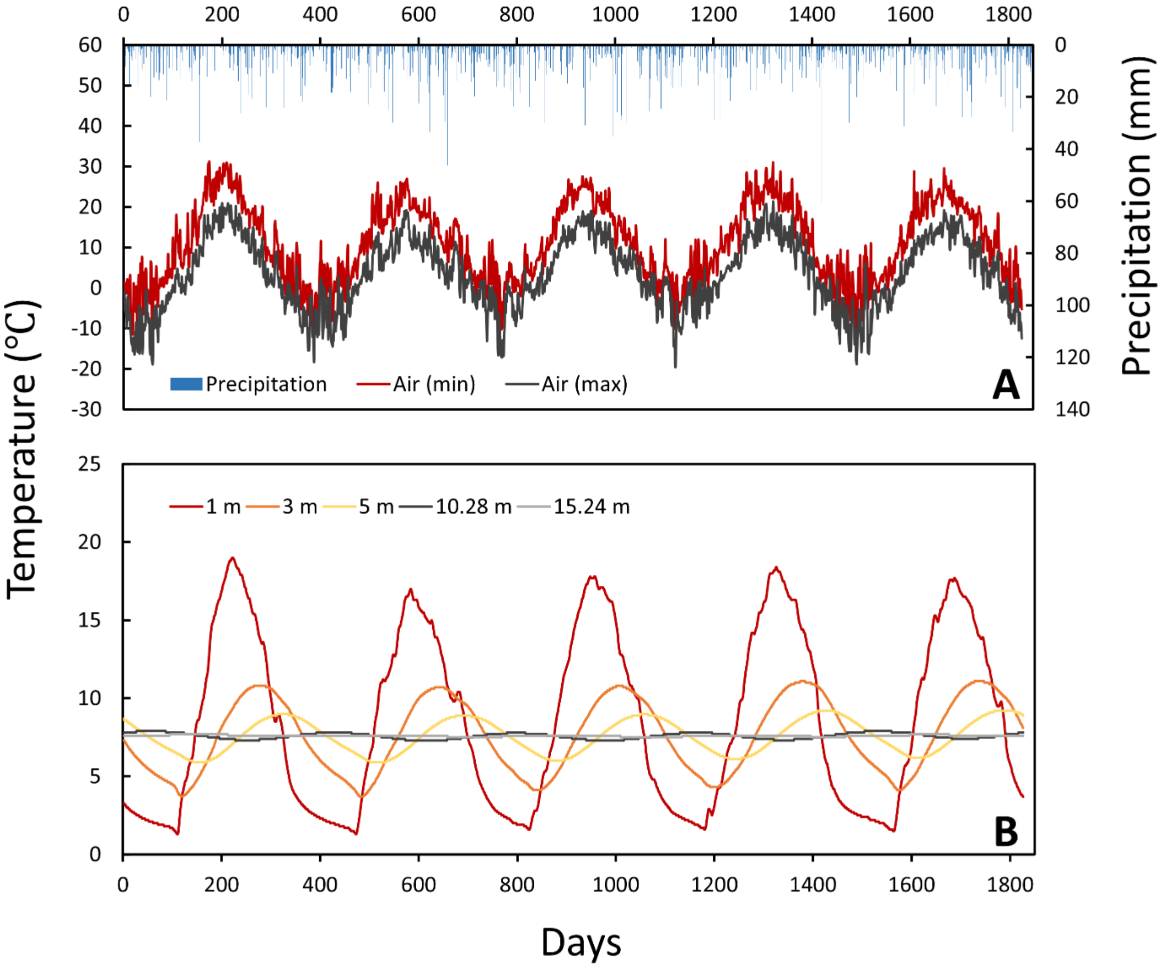

Figure 30. Baseline lowland model simulation data for the years of 2016-2020 extracted from SHAW. (A) Maximum and minimum daily air temperature and total rainfall input to the model. (B) Subsurface temperatures at various depths in response to forcing from the surface. The temperature data at depths of 1 and 3 m were extracted from the surface domain, whereas the others are from the conduction-only lower lowland domain. The temperature signals are damped and lagged with depth. The geometry of these modelled signals may be compared to measured spring signals to estimate their source depths.

Although there is a high degree of uncertainty involved in these results, they indicate that there is potential for springs to be significantly sensitive to increasing air and land surface temperatures in BHH. As intended, this modelling study has established that there is potential for springs to warm in the future and that a more robust 3D model, informed by detailed field measurements and a robust ensemble of future climate simulations, may be worthwhile to further elucidate the processes involved.

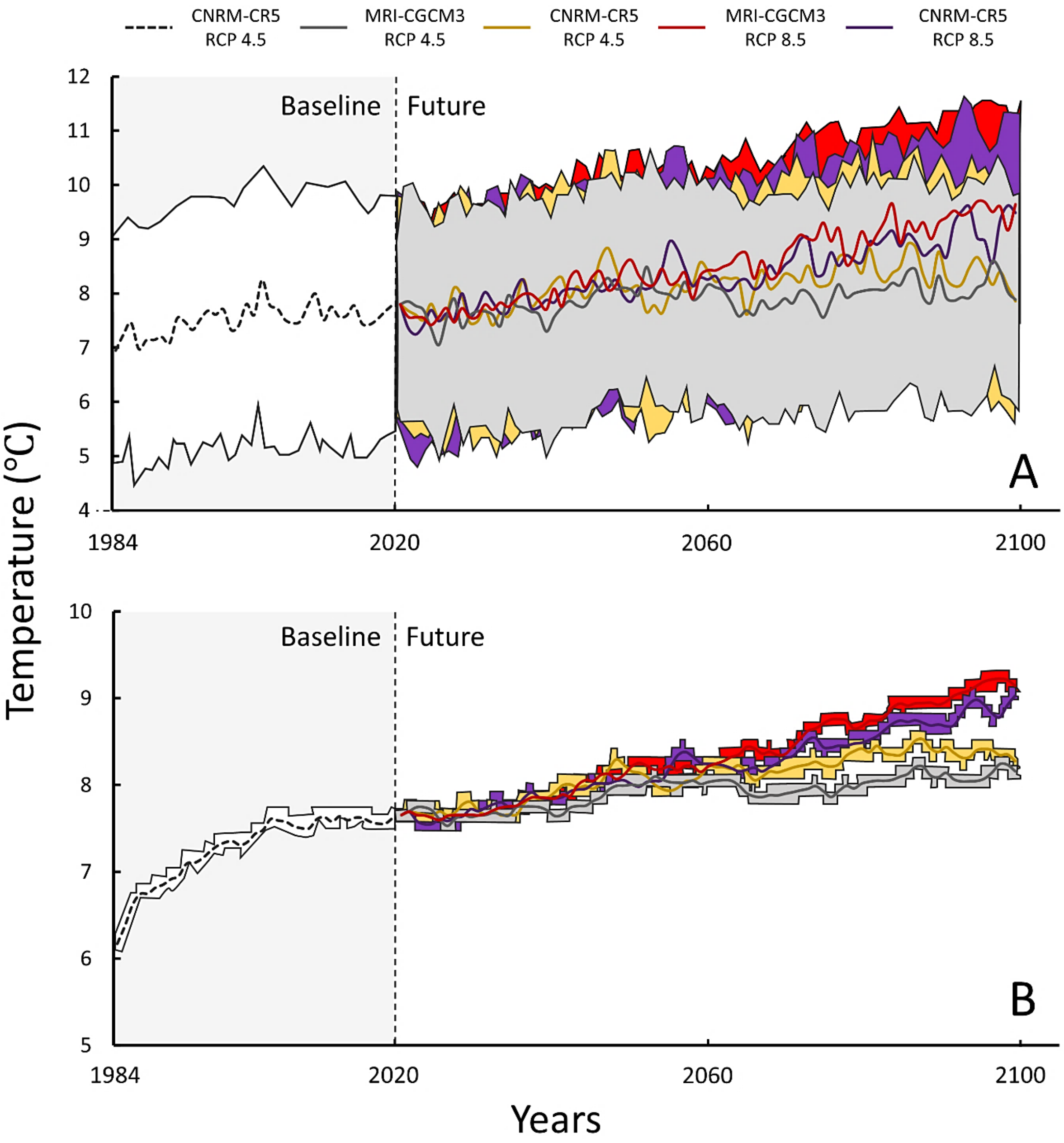

Figure 31. Modelled 365-day-averaged subsurface temperatures (lines) and their associated daily range (area) at two depths within the lowland model. The baseline period (1984-2020) uses the CNRM-CR5 simulation data, and four future simulations were run for the period of 2020-2100. The greatest temperature increase was induced by the MRI-CGCM3 RCP 8.5 simulation, and the lowest was induced by the MRI-CGCM3 RCP 4.5 simulation. (A) depicts the temperature at a depth of 4.2 metres (approximate depth of the lowland well sensor), whereas (B) was at 13.9 metres (approximate depth of the upland well sensor). Temperature variance decreased with depth. The beginning of the baseline simulation involves the model domain stabilizing and should be regarded carefully.

CHAPTER 4: SYNTHESIS & FUTURE WORK

The DFO is committed to improving and maintaining the ecological health of BHH and its endemic population of GIM, an initiative that is strongly linked to the summertime thermal regime of the Basin Head lagoon. Lagoon water temperatures averaged about 22℃ during the summer of 2020 and were measured above 30℃ in some parts of BHH. Blue mussels and GIM are negatively impacted by this level of thermal stress. This study explored the role of groundwater in maintaining survivable thermal stress levels for GIM in BHH over the summer and investigated the sensitivity of groundwater to increasing air temperatures.

Using TIR imagery and temperature sensors during the summers of 2019 and 2020, intertidal springs and streams (with temperatures of approximately 7-10℃ and 8-13℃, respectively) were observed to locally impact water temperature surrounding their discharge points. This localised influence is in part modulated by tidal stage, which was evidenced by field measurements of water properties and TIR timelapse imagery. This study began to elucidate the lagoon-scale influence of fresh cold-water inputs by making an estimation of focussed spring and stream discharge to the lagoon over a 35-day focussed study period. Streams were estimated to contribute 153,000 m^3 over the focussed study period, and this flow was assumed to be entirely groundwater-derived based on the meteorological record of this period, the temperature of the streams, and the nature of the hydrographs. Direct groundwater discharge to BHH via intertidal springs was estimated between 60,000 and 130,000 m^3 over the same 35 days, which is similar in magnitude to the incoming streamflow. Direct rainfall to the surface of the lagoon amounted to approximately 22,000 m^3. Additional direct freshwater input from the coastal wetland system within the harbour, as well as widespread diffuse seepage to the system is certain, but were not quantified in this study. However, Danielescu et al. (2009) found that approximately 25% of groundwater input was delivered via diffuse mechanisms to two PEI coastal systems. Like Danielescu et al. (2009), the findings of this study emphasise that the magnitude of direct groundwater inputs to PEI coastal systems is likely significant relative to stream inputs. This may be particularly relevant when considering anthropogenic nutrient inputs, which is of interest to the DFO. The preliminary volumetric estimates derived from this study may be useful to develop preliminary nutrient loading estimates to BHH when coupled with nutrient concentration data.

The influence of groundwater on the temperature of the lagoon, relative to other thermal controls (e.g., tidal exchange, rainfall, solar radiation), is likely very dynamic in space and time. Groundwater inputs may be most significant as a thermal buffer throughout the hottest periods of the summer months when rainfall is scarce and lagoon temperatures and stream baseflow indices peak. It is expected that groundwater influence is more impactful during low tides relative to high tides, when spring discharge is potentially at its greatest and the total volume of water within the lagoon is reduced, and overnight when solar radiation is less impactful on the lagoon and streams. The overall temperature of BHH may be expected to be largely dominated by solar radiation (e.g., Rodríguez-Rodríguez & Moreno-Ostos, 2006); however, focussed and indirect groundwater discharges generated localised cold-water refuges within the lagoon, and the estimated net advective heat of the springs and streams were the same order of magnitude over the focussed study period (Chapter 3, Section 3.6). Conversely, the advective heat flux associated with direct rainfall to BHH was at least one order of magnitude smaller. In the context of BHH, the significance of lagoon temperature changes could be assessed based on species-specific temperature thresholds and measurements of metabolic activity or survival. Further characterisation of the complex processes controlling the lagoon's heat budget (as shown in Figure 6) would need to be undertaken to conduct a full energy budget and concretise our understanding of lagoon-scale thermal dynamics and thus the larger-scale significance of groundwater and its sensitivity to climate warming.

Intertidal springs in BHH are sourced from different effective depths in the groundwater system(s) feeding the harbour. Different springs in BHH experience varied thermal forcing based on their associated soil layers, land-use, land cover, and travel paths that dictate their thermal signature and sensitivity to surface temperatures. In this study, a 1D subsurface model was used to demonstrate that some springs within BHH will likely warm in response to future air temperature increases within decades, though this warming will be at least temporarily attenuated in comparison to atmospheric warming. The various simulation results suggested that there is potential for the degree of warming to be negligible to potentially significant for the ecological health of the harbour, as the annual average temperature of shallower groundwater supplying some springs may warm more than 2℃ before the year 2100. Hydrogeological assessments and field investigations were conducted that confirmed that the subsurface conditions were consistent with values expected for PEI soils and bedrock; thus, findings from this work likely apply to other PEI coastal watersheds. However, a greater sample size of springs is required to assess the average source depth and sensitivity of intertidal springs at the lagoon scale and elsewhere on PEI. A more complex, robust, and data-rich modelling exercise may engender greater certainty in the future projections of groundwater temperature in PEI; however, this study provides compelling preliminary findings and the initial motivation for such a labour-intensive modelling investment.

Characterising the results of future climate warming and urban expansion on groundwater thermal regimes would be highly related to this work and relevant to marine management objectives comparable to those of the DFO in BHH. Subsurface heating attributed to urban heat islands compounds with the heating associated with climate (Benz et al., 2021; Taniguchi et al., 2007; Taylor & Stefan, 2009). A future area of research may be to characterise the thermal impact these coastal developments may have on the temperatures of coastal groundwater discharges and the resulting downgradient ecological impacts inflicted on heat-sensitive species. This may be of particular interest for coastal water features with high seasonal thermal gradients between surface water and groundwater, restricted flushing rates, shallow depths, and substantial groundwater inputs.

There are many other opportunities to build upon this work in the future if there are the resources and interest to do so, using this project as a foundation. Firstly, increasing the number of springs sampled for temperature and volumetric discharge would improve the certainty and interpretability of the results. Secondly, groundwater discharge to the harbour could be more robustly estimated by comparing various groundwater discharge quantification methods in BHH (e.g., radon, distributed coastal wells, seepage meter arrays, tracers, and alternative TDA methods). Lastly, the hydrodynamics and thermodynamics within the lagoon could be explored in greater depth, with consideration of future climate change, sea level rise, and aquatic habitat suitability. The coastal wetland is certainly a highly complex and fascinating hydrogeological system that likely plays a significant role in the thermal energy balance of the lagoon – additional understanding of this system would be of academic and practical significance. Further elucidation of the lagoon's heat budget may help guide lagoon-scale management priorities.

This thesis contributes novel local data and interpretations about lagoon and watershed thermal dynamics, watershed and coastal hydrology, and groundwater thermal sensitivity to future climate change to local watershed groups and federal decision makers. It is believed that this work has novelty in the field of ecohydrology, as no previous studies were identified that investigated groundwater thermal sensitivity as a driver of future change in coastal lagoon ecosystems. This thesis also includes methodological advancements and opportunities for the assessment of near-shore springs using drone-assisted TIR imagery and inexpensive temperature sensors. In addition to the numerous historical studies and DFO investment into BHH, the contributions of this thesis emphasize that this study site has excellent potential for academic collaborations with government that benefit all parties and the progression of scientific knowledge.

REFERENCES

Aldridge, B. N., & Garrett, J. M. (1973). *Roughness coefficients for stream channels in Arizona* (Open-File Report 73-3). U.S. Geological Survey. https://doi.org/10.3133/ofr733

Aller, L., Bennett, T., Hackett, G., & Petty, R. J. (1991). *Handbook of suggested practices for the design and installation of ground-water monitoring wells* (No. EPA160014-891034). U.S. Environmental Protection Agency.

Almada-Villela, P. C., Davenport, J., & Gruffydd, L. D. (1982). The effects of temperature on the shell growth of young mytilus edulis L. *Journal of Experimental Marine Biology and Ecology*, *59*(2–3), 275–288. https://doi.org/10.1016/0022-0981(82)90121-6

Anderson, M. P. (2005). Heat as a ground water tracer. *Ground Water*, *43*(6), 951–968. https://doi.org/10.1111/j.1745-6584.2005.00052.x

Anthony, A., Atwood, J., Byron, C., Cobb, S., Foster, C., Fry, C., Gold, A., Hagos, K., Heffner, L., Kellogg, D., Dibble, K., Opaluch, J., Oviatt, C., Pfeiffer-Herbert, A., Rohr, N., Smith, L., Swift, J., & Vinhateiro, N. (2009). Coastal lagoons and climate change: ecological and social ramifications in U.S. Atlantic and Gulf Coast ecosystems. *Ecology and Society*, *14*(1), 0–29. https://doi.org/10.5751/ES-02719-140108

Arcement, G. J., & Schneider, V. R. (1989). *Guide for selecting Manning's roughness coefficients for natural channels and flood plains* (Water Supply Paper 2339). U.S. Geological Survey. https://doi.org/10.3133/wsp2339

Archfield, S. A., & Vogel, R. M. (2010). Map correlation method: Selection of a reference streamgage to estimate daily streamflow at ungaged catchments. *Water Resources Research*, *46*(10). https://doi.org/10.1029/2009WR008481

Asquith, W. H., Roussel, M. C., & Vrabel, J. (2006). *Statewide analysis of the drainage-area ratio method for 34 streamflow percentile ranges in Texas* (Scientific Investigations Report 2006-5286). U.S. Geological Survey. https://doi.org/10.3133/sir20065286

Bader, M. (2020). *MB-Ruler - the triangular screen ruler [analysis software version 5.3]*. http://www.markus-bader.de/MB-Ruler/download.php

Barnes, R. S. K. (1980). *Coastal lagoons: the natural history of a neglected habitat*. Cambridge University Press.

Bayer, P., Rivera, J. A., Schweizer, D., Schärli, U., Blum, P., & Rybach, L. (2016). Extracting past atmospheric warming and urban heating effects from borehole temperature profiles. *Geothermics*, *64*, 289–299. https://doi.org/10.1016/j.geothermics.2016.06.011

Bedient, P. B., Huber, W. C., & Vieux, B. E. (2013). *Hydrology and floodplain analysis* (5th ed.). Pearson Education Liited.

Bejannin, S., van Beek, P., Stieglitz, T., Souhaut, M., & Tamborski, J. (2017). Combining airborne thermal infrared images and radium isotopes to study submarine groundwater discharge along the French Mediterranean coastline. *Journal of Hydrology: Regional Studies*, *13*(1), 72–90. https://doi.org/10.1016/j.ejrh.2017.08.001

Bense, V. F., & Beltrami, H. (2007). Impact of horizontal groundwater flow and localized deforestation on the development of shallow temperature anomalies. *Journal of Geophysical Research: Earth Surface*, *112*(F4). https://doi.org/10.1029/2006JF000703

Bense, V. F., & Kurylyk, B. L. (2017). Tracking the subsurface signal of decadal climate warming to quantify vertical groundwater flow rates. *Geophysical Research Letters*, *44*(24), 244–253. https://doi.org/10.1002/2017GL076015

Benson, M. A., & Dalrymple, T. (1967). *General field and office procedures for indirect discharge measurements* (Techniques of Water-Resources Investigations 03-A1). U.S. Geological Survey. https://doi.org/10.3133/twri03A1

Benson, V. S., VanLeeuwen, J. A., Stryhn, H., & Somers, G. H. (2007). Temporal analysis of groundwater nitrate concentrations from wells in Prince Edward Island, Canada: Application of a linear mixed effects model. *Hydrogeology Journal*, *15*(5), 1009–1019. https://doi.org/10.1007/s10040-006-0153-x

Benz, S. A., Davis, S. J., & Burney, J. A. (2021). Drivers and projections of global surface temperature anomalies at the local scale. *Environmental Research Letters*, *16*(6), 64093. https://doi.org/10.1088/1748-9326/ac0661

Bintz, J. C., Nixon, S. W., Buckley, B. A., & Granger, S. L. (2003). Impacts of temperature and nutrients on coastal lagoon plant communities. *Estuaries*, *26*(3), 765. https://doi.org/10.1007/BF02711987

Bird, N., Chen, L., & McLachlan, J. (1979). Effects of temperature, light and salinity on growth in culture of Chondrus crispus, Furcellaria lumbricalis, Gracilaria tikvahiae (Gigartinales, Rhodophyta), and Fucus serratus (Fucales, Phaeophyta). *Botanica Marina*, *22*(8), 521–527. https://doi.org/10.1515/botm.1979.22.8.521

Bopp, L., Le Quéré, C., Heimann, M., Manning, A. C., & Monfray, P. (2002). Climate-induced oceanic oxygen fluxes: Implications for the contemporary carbon budget. *Global Biogeochemical Cycles*, *16*(2), 6–13. https://doi.org/10.1029/2001GB001445

Bourdet, D., & Gringarten, A. C. (1980). Determination of fissure volume and block size in fractured reservoirs by type-curve analysis. In *SPE Annual Technical Conference and Exhibition* (p. 20). Society of Petroleum Engineers. https://doi.org/10.2118/9293-MS

Bouwer, H., & Rice, R. C. (1976). A slug test for determining hydraulic conductivity of unconfined aquifers with completely or partially penetrating wells. *Water Resources Research*, *12*(3), 423–428. https://doi.org/10.1029/WR012i003p00423

Braca, G. (2008). *Stage-discharge relationships in open channels: practices and problems* (FORALPS Technical Report 11). Universita degli Studi di Trento, Dipartimento di Ingegneria Civile e Ambientale. https://www.academia.edu/8471945/STAGE-DISCHARGE_RELATIONSHIPS_IN_OPEN_CHANNELS_PRACTICES_AND_PROBLEMS

Brandon, L. V. (1966). *Groundwater hydrology and water supply of Prince Edward Island* (Paper 64-38). Geological Survey of Canada. https://doi.org/10.4095/101003

Briggs, M. A., Lane, J. W., Snyder, C. D., White, E. A., Johnson, Z. C., Nelms, D. L., & Hitt, N. P. (2018). Shallow bedrock limits groundwater seepage-based headwater climate refugia. *Limnologica*, *68*, 142–156. https://doi.org/10.1016/j.limno.2017.02.005

Brooks, R. H., & Corey, A. T. (1966). Properties of porous media affecting fluid flow. *Journal of Irrigation and Drainage Division*, 61–88.

Butler, J. J. (1998). *The design, performance, and analysis of slug tests*. CRC Press LLC.

Butler, J. J., Garnett, E. J., & Healey, J. M. (2003). Analysis of slug tests in formations of high hydraulic conductivity. *Groundwater*, *41*(5), 620–631. https://doi.org/10.1111/j.1745-6584.2003.tb02400.x

Caissie, D. (2006). The thermal regime of rivers: A review. *Freshwater Biology*, *51*(8), 1389–1406. https://doi.org/10.1111/j.1365-2427.2006.01597.x

Caissie, D., & Luce, C. H. (2017). Quantifying streambed advection and conduction heat fluxes. *Water Resources Research*, *53*(2), 1595–1624. https://doi.org/https://doi.org/10.1002/2016WR019813

Carr, P. A. (1969). Salt-water intrusion in Prince Edward Island. *Canadian Journal of Earth Sciences*, *6*(1), 63–74. https://doi.org/10.1139/e69-007

Carr, P. A. (1971). Use of harmonic analysis to study tidal fluctuations in aquifers near the sea. *Water Resources Research*, *7*(3), 632–643. https://doi.org/10.1029/WR007i003p00632

Carrington, E. (2002). Seasonal variation in the attachment strength of blue mussels: Causes and consequences. *Limnology and Oceanography*, *47*(6), 1723–1733. https://doi.org/10.4319/lo.2002.47.6.1723

Carter, M. R. (1987). Physical properties of some Prince Edward Island soils in relation to their tillage requirement and suitability for direct drilling. *Canadian Journal of Soil Science*, *67*(3), 473–487. https://doi.org/10.4141/cjss87-045

Chen, Z., Grasby, S. E., & Osadetz, K. G. (2004). Relation between climate variability and groundwater levels in the upper carbonate aquifer, southern Manitoba, Canada. *Journal of Hydrology*, *290*(1), 43–62. https://doi.org/https://doi.org/10.1016/j.jhydrol.2003.11.029

Chi, G., Giles, P. S., Williamson, M. A., Lavoie, D., & Bertrand, R. (2003). Diagenetic history and porosity evolution of Upper Carboniferous sandstones from the Spring Valley #1 well, Maritimes Basin, Canada - Implications for reservoir development. *Journal of Geochemical Exploration*, *80*(2–3), 171–191. https://doi.org/10.1016/S0375-6742(03)00190-0

Chikita, K. A., Uyehara, H., Mamun, A. Al, Umgiesser, G., Iwasaka, W., Hossain, M. M., & Sakata, Y. (2015). Water and heat budgets in a coastal lagoon controlled by groundwater outflow to the ocean. *Limnology*, *16*(3), 149–157. https://doi.org/10.1007/s10201-015-0449-4

Chow, V. T. (1959). *Open channel hydraulics* (H. E. Davis (ed.)). McGraw-Hill Book Company, Inc.

Coluccio, K., Santos, I., Jeffrey, L. C., Katurji, M., Coluccio, S., & Morgan, L. K. (2020). Mapping groundwater discharge to a coastal lagoon using combined spatial airborne thermal imaging, radon (222Rn) and multiple physicochemical variables. *Hydrological Processes*, *34*(24), 4592–4608. https://doi.org/10.1002/hyp.13903

Cowan, W. L. (1956). Estimating hydraulic roughness coefficients. *Agricultural Engineering*, *37*(7), 473–475.

Crowl, G. H. (1969a). *Geology of Mount Stewart-Souris map-area, Prince Edward Island (11 L/7, L/8)* (Paper 67-66). Geological Survey of Canada. https://doi.org/10.4095/102347

Crowl, G. H. (1969b). *Glacial direction indicators, eastern Prince Edward Island* (Paper 67-66; p. 26). Geological Survey of Canada. https://doi.org/10.4095/102347

Crowl, G. H. (1969c). *Surficial geology, Mount Stewart - Souris, Prince Edward Island ["A" Series Map 1260A]* (Paper 67-66). Geological Survey of Canada. https://doi.org/10.4095/108918

Crowl, G. H., & Frankel, L. (1970). *Surficial geology of Rustico map area, Prince Edward Island [Map 21]* (Paper 70-39). Geological Survey of Canada. https://doi.org/10.4095/102361

Dadic, R., Mott, R., Lehning, M., & Burlando, P. (2010). Wind influence on snow depth distribution and accumulation over glaciers. *Journal of Geophysical Research: Earth Surface*, *115*(F1). https://doi.org/10.1029/2009JF001261

Danielescu, S., MacQuarrie, K., & Faux, R. (2009). The integration of thermal infrared imaging, discharge measurements and numerical simulation to quantify the relative contributions of freshwater inflows to small estuaries in Atlantic Canada. *Hydrological Processes*, *23*(20), 2847–2859. https://doi.org/10.1002/hyp.7383

Davison, I. R., & Pearson, G. A. (1996). Stress tolerance in intertidal seaweeds. *Journal of Phycology*, *32*(2), 197–211. https://doi.org/10.1111/j.0022-3646.1996.00197.x

DELJ. (2013). *Water extraction permitting policy*. https://www.princeedwardisland.ca/sites/default/files/publications/water_extraction_permitting_policy_2013.pdf

DeVries, D. A. (1963). Thermal properties of soils. In W. R. Van Wijk (Ed.), *Physics of plant environment* (p. 382). North-Holland Publishing Co.

DFO. (2009). *Ecological assessment of Irish moss (Chondrus crispus) in Basin Head Marine Protected Area [corrected August 2011]* (Gulf Region CSAS Science Advisory Report 2008/059). Fisheries and Oceans Canada.

DJI. (2018). *Zenmuse XT 2 - User manual V1.0*. https://dl.djicdn.com/downloads/Zenmuse XT 2/Zenmuse XT 2 User Manual v1.0_.pdf

Dobereiner, L. (1984). *Engineering geology of weak sandstones* [Doctoral dissertation, University of London]. https://spiral.imperial.ac.uk/bitstream/10044/1/8480/1/Lorenz_Dobereiner-1984-PhD-Thesis.pdf

Domeneghetti, A., Castellarin, A., & Brath, A. (2012). Assessing rating-curve uncertainty and its effects on hydraulic model calibration. *Hydrology and Earth System Sciences*, *16*(4), 1191–1202. https://doi.org/10.5194/hess-16-1191-2012

Domenico, P. A., & Schwartz, F. W. (1990). Physical and chemical hydrogeology. In C. Mills, D. Herbert, & E. Starr (Eds.), *Encyclopedia of Materials Characterization* (2nd ed.). John Wiley & Sons, Inc.

Dong-Woon, T. A.-H., & Byoung-Seol, T. A.-K. (2012). Temporal variations of submarine groundwater discharge (SGD) and SGD-driven nutrient inputs in the coastal ocean of Jeju Island. *The Korean Society of Oceanography*, *17*(4), 252–261. https://doi.org/10.7850/JKSO.2012.17.4.252

Dong, L., Fu, C., Liu, J., & Wang, Y. (2018). Disturbances of Temperature-Depth Profiles by Surface Warming and Groundwater Flow Convection in Kumamoto Plain, Japan. *Geofluids*, *2018*, 8451276. https://doi.org/10.1155/2018/8451276

Dowd, W. W., & Somero, G. N. (2013). Behavior and survival of Mytilus congeners following episodes of elevated body temperature in air and seawater. *The Journal of Experimental Biology*, *216*(3), 502–514. https://doi.org/10.1242/jeb.076620

Dymond, J. R., & Christian, R. (1982). Accuracy of discharge determined from a rating curve. *Hydrological Sciences Journal*, *27*(4), 493–504. https://doi.org/10.1080/02626668209491128

ECCC. (2018a). *Climate data extraction tool - Statistically downscaled climate scenarios*. https://climate-change.canada.ca/climate-data/#/downscaled-data

ECCC. (2018b). *Scenarios and climate models*. https://www.canada.ca/en/environment-climate-change/services/climate-change/canadian-centre-climate-services/basics/scenario-models.html#toc0

ECCC. (2019a). *Historical data, Kingsboro, Prince Edward Island [Station ID 30618; 2000-2007]*. https://climate.weather.gc.ca/historical_data/search_historic_data_stations_e.html?searchType=stnName&timeframe=1&txtStationName=kingsboro&searchMethod=contains&optLimit=yearRange&StartYear=1840&EndYear=2020&Year=2020&Month=4&Day=30&selRowPerPage=25

ECCC. (2019b). *Technical documentation - Statistically downscaled climate scenarios*. https://www.canada.ca/en/environment-climate-change/services/climate-change/canadian-centre-climate-services/display-download/technical-documentation-downscaled-climate-scenarios.html

ECCC. (2021a). *Canadian climate normals 1981-2010 station data: East Baltic Prince Edward Island*. https://climate.weather.gc.ca/climate_normals/results_1981_2010_e.html?searchType=stnProv&lstProvince=PE&txtCentralLatMin=0&txtCentralLatSec=0&txtCentralLongMin=0&txtCentralLongSec=0&stnID=6529&dispBack=0

ECCC. (2021b). *Historical data, East Point, Prince Edward Island [Station ID 7177; 2019-2020]*. https://climate.weather.gc.ca/climate_data/hourly_data_e.html?timeframe=1&Year=2021&Month=7&Day=20&hlyRange=1994-02-01%7C2021-07-20&dlyRange=1992-12-08%7C2021-07-20&mlyRange=2004-01-01%7C2007-07-01&StationID=7177&Prov=PE&urlExtension=_e.html&searchType=st

ECCC. (2021c). *Historical data, St. Peters, Prince Edward Island [Station ID 41903; 2019-2020]*. https://climate.weather.gc.ca/climate_data/hourly_data_e.html?timeframe=1&Year=2021&Month=7&Day=20&hlyRange=2003-08-14%7C2021-07-20&dlyRange=2003-08-14%7C2021-07-20&mlyRange=2004-01-01%7C2007-07-01&StationID=41903&Prov=PE&urlExtension=_e.html&searchType=s

Eggert, A. (2012). Seaweed responses to temperature. In C. Wiencke & K. Bischof (Eds.), *Seaweed Biology - Ecological Studies (Analysis and Synthesis)* (pp. 47–66). Springer. https://doi.org/10.1007/978-3-642-28451-9_3

El-Naqa, A. (1994). Estimation of transmissivity from specific capacity data in fractured carbonate rock aquifer, central Jordan. *Environmental Geology*, *23*(1), 73–80. https://doi.org/10.1007/BF00773142

Emerson, D. G., Vecchia, A. V., & Dahi, A. L. (2005). *Evaluation of drainage-area ratio method used to estimate streamflow for the Red River of the North Basin, North Dakota and Minnesota* (Scientific Investigations Report 2005 – 5017). U.S. Geological Survey. https://doi.org/10.3133/sir20055017

Environment and Climate Change Canada (ECCC), Computer Research Institute of Montréal (CRIM), Ouranos, the Pacific Climate Impacts Consortium (PCIC), the Prairie Climate Centre (PCC), & HabitatSeven. (2021). *Climate data for a resilient Canada*. https://climatedata.ca/

Esri, DigitalGlobe, GeoEye, I-cubed, FSA, U., USGS, AEX, Getmapping, Aerogrid, IGN, IGP, Swisstopo, & GIS User Community. (2009). *World imagery (basemap)*. https://services.arcgisonline.com/ArcGIS/rest/services/World_Imagery/MapServer

Ferguson, G., & Woodbury, A. (2005). The effects of climatic variability on estimates of recharge from temperature profiles. *Ground Water*, *43*, 837–842. https://doi.org/10.1111/j.1745-6584.2005.00088.x

Fetter, C. W. (2001). *Applied hydrogeology* (4th ed.). Pearson.

Flerchinger, G. (2017). *The simultaneous heat and water (SHAW) model: Technical documentation (version 3.0)* (Technical Report NWRC 2000-09). USDA Agricultural Research Service. https://www.ars.usda.gov/ARSUserFiles/20520000/shawdocumentation.pdf

Flerchinger, G., & Saxton, K. (1989). Simultaneous Heat and Water Model of a freezing snow-residue-soil system I. Theory and development. *Transactions of the ASAE*, *32*, 565–571. https://doi.org/10.13031/2013.31040

FLIR Systems Ltd. (2012). *The ultimate infrared handbook for R&D professionals* (Revision 12). https://termogram.com/images/pdf/termografia/flir-thermal-camera-guide-for-research-professionals.pdf

Francis, R. M. (1989). *Hydrogeology of the Winter River Basin, Prince Edward Island*. Department of Environment, PEI. http://www.gov.pe.ca/photos/original/cle_WinterR.pdf

Government of PEI. (n.d.). *PEI soil survey 1970-1978*. http://www.gov.pe.ca/gis/MapunitnumCodes.htm

Government of PEI. (2018). *General introduction to Island forest history and ecology*. https://www.princeedwardisland.ca/en/information/communities-land-and-environment/general-introduction-island-forest-history-and-ecology

Government of PEI. (2019). *Water well information system [Kingsboro well logs from 1974 to 2012]*.

Government of PEI. (2021). *Ground water data: Observation well data [Souris Line Road]*. http://www.gov.pe.ca/envengfor/groundwater/app.php?map=YES&id=SL&lang=E

Grasby, S. E., Majorowicz, J., & Ko, M. (2009). Geothermal maps of Canada. In *Geological Survey of Canada open File 6167*. https://doi.org/10.4095/247765

Guyondet, T. (2019). *Basin Head hydrodynamic modelling update [Internal oral presentation]* (p. 12). Fisheries and Oceans Canada.

Haines, P. E. (2006). *Physical and chemical behaviour and management of intermittently closed and open lakes and lagoons (ICOLLs) in NSW* [Doctoral dissertation, Griffith University]. https://research-repository.griffith.edu.au

Halford, K. J., & Kuniansky, E. L. (2002). *Documentation of spreadsheets for the analysis of aquifer-test and slug-test data* (Open-File Report 02-197). U.S. Geological Survey. http://pubs.usgs.gov/of/2002/ofr02197/

Hansen, B. (2012). *Simulating the effects of climate change on a coastal aquifer, Summerside, Prince Edward Island* [Master's thesis, Saint Francis Xavier University]. https://atlanticadaptation.ca/en/islandora/object/acasa%3A468

Hansen, B., & Ferguson, G. (2012a). *Investigation of the risk of salt water intrusion to water supply infrastructure, Lennox Island, PEI [case study]*. http://www.gov.pe.ca/photos/original/cle_WA2.pdf

Hansen, B., & Ferguson, G. (2012b). *Simulating saltwater intrusion in a changing climate, Summerside, PEI [case study]*. http://www.gov.pe.ca/photos/original/cle_WA2.pdf

Harley, C. D. G., Anderson, K. M., Demes, K. W., Jorve, J. P., Kordas, R. L., Coyle, T. A., & Graham, M. H. (2012). Effects of climate change on global seaweed communities. *Journal of Phycology*, *48*(5), 1064–1078. https://doi.org/10.1111/j.1529-8817.2012.01224.x

Harley, C. D. G., Randall Hughes, A., Hultgren, K. M., Miner, B. G., Sorte, C. J. B., Thornber, C. S., Rodriguez, L. F., Tomanek, L., & Williams, S. L. (2006). The impacts of climate change in coastal marine systems. *Ecology Letters*, *9*(2), 228–241. https://doi.org/10.1111/j.1461-0248.2005.00871.x

Healy, R. W., & Cook, P. G. (2002). Using groundwater levels to estimate recharge. *Hydrogeology Journal*, *10*(1), 91–109. https://doi.org/10.1007/s10040-001-0178-0

Heath, R. C. (1983). *Basic Ground-Water Hydrology* (Water Supply Paper 2220). U.S. Geological Survey. https://pubs.er.usgs.gov/djvu/WSP/wsp_2220.pdf

Hemmerle, H., & Bayer, P. (2020). Climate change yields groundwater warming in Bavaria, Germany. *Frontiers in Earth Science*, *8*, 523. https://doi.org/10.3389/feart.2020.575894

Hortness, J. E. (2006). *Estimating low-flow frequency statistics for unregulated streams in Idaho* (Scientific Investigations Report 2006-5035). U.S. Geological Survey. https://pubs.water.usgs.gov/sir20065035

Huntley, D., Nommensen, R., & Steffey, D. (1992). The use of specific capacity to assess transmissivity in fractured-rock aquifers. *Groundwater*, *30*(3), 396–402. https://doi.org/10.1111/j.1745-6584.1992.tb02008.x

Hvorslev, J. (1951). *Time lag and soil permeability in ground-water observations* (Bulletin No. 36). U.S. Army Corps of Engineers. http://luk.staff.ugm.ac.id/jurnal/freepdf/Hvorslev1951-USACEBulletin36.pdf

IPCC. (2014). *Climate change 2014 Synthesis Report - Contribution of working groups I, II and III to the fifth Assessment Report of the Intergovernmental Panel on Climate Change [Core writing team, Pachauri, R.K. and Meyer, L.A. (eds.)].*

Iwata, Y., Hayashi, M., Suzuki, S., Hirota, T., & Hasegawa, S. (2010). Effects of snow cover on soil freezing, water movement, and snowmelt infiltration: A paired plot experiment. *Water Resources Research*, *46*(9). https://doi.org/10.1029/2009wr008070

Jennings, K. S., Winchell, T. S., Livneh, B., & Molotch, N. P. (2018). Spatial variation of the rain–snow temperature threshold across the Northern Hemisphere. *Nature Communications*, *9*(1), 1148. https://doi.org/10.1038/s41467-018-03629-7

Jensen, A. M., Neilson, B. T., McKee, M., & Chen, Y. (2012). Thermal remote sensing with an autonomous unmanned aerial remote sensing platform for surface stream temperatures. *2012 IEEE International Geoscience and Remote Sensing Symposium*, 5049–5052. https://doi.org/10.1109/IGARSS.2012.6352476

Ji, Z.-G. (2017). Hydrodynamics. In *Hydrodynamics and water quality: Modelling rivers, lakes, and estuaries* (2nd ed., pp. 11–71). John Wiley & Sons Inc. https://doi.org/https://doi.org/10.1002/9780470241066.ch2

Jiang, Y., Somers, G., & Mutch, J. (2004). Application of numerical modeling to groundwater assessment and management in Prince Edward Island. *57th Canadian Geotechnical Conference*, *57*, 2–9. http://www.gov.pe.ca/photos/original/elj_model_gwt.pdf

Jiang, Y., Somers, G., & Paradis, D. (2007). Estimation of groundwater residence times in the Wilmot River watershed on Prince Edward Island – implications for nutrient reduction. *Ottawa Geo*, 58–65. http://www.gov.pe.ca/photos/original/cle_WA33.pdf

Johnson, A. G., Glenn, C. R., Burnett, W. C., Peterson, R. N., & Lucey, P. G. (2008). Aerial infrared imaging reveals large nutrient-rich groundwater inputs to the ocean. *Geophysical Research Letters*, *35*(15). https://doi.org/10.1029/2008GL034574

Joostema, P. (2015). *Site location plan: Saltwater production well development [Well core log and pumping test data]*. Joost Environmental.

Joseph, V., Thériault, M.-H., Novaczek, I., Coffin, M., Cairns, D., Nadeau, A., Boudreau, M., Plourde, M.-A., Quijon, P. A., & Tummon Flynn, P. (2021). *Review of monitoring activities in the Basin Head Marine Protected Area in the context of their effectiveness in evaluating attainment of conservation objectives* (Canadian Science Advisory Secretariat Research Document 2021/044). Fisheries and Oceans Canada. https://www.dfo-mpo.gc.ca/csas-sccs/Publications/ResDocs-DocRech/2021/2021_044-eng.pdf

Juanes, J. A., & McLachlan, J. L. (1992a). Productivity of Chondrus crispus stackhouse (Rhodophyta, Gigartinales) in sublittoral Prince Edward Island, Canada. I. Seasonal pattern. *Botanica Marina*, *35*(5), 391–398. https://doi.org/10.1515/botm.1992.35.5.391

Juanes, J. A., & McLachlan, J. L. (1992b). Productivity of Chondrus crispus stackhouse (Rhodophyta, Gigartinales) in sublittoral Prince Edward Island, Canada. II. Influence of temperature and nitrogen reserves. *Botanica Marina*, *35*(5), 399–406. https://doi.org/10.1515/botm.1992.35.5.399

Kaandorp, V. P., Doornenbal, P. J., Kooi, H., Peter Broers, H., & de Louw, P. G. B. (2019). Temperature buffering by groundwater in ecologically valuable lowland streams under current and future climate conditions. *Journal of Hydrology X*, *3*, 100031.

Kalacska, M., Lucanus, O., Arroyo-Mora, J. P., Laliberté, É., Elmer, K., Leblanc, G., & Groves, A. (2020). Accuracy of 3D landscape reconstruction without ground control points using different UAS platforms. *Drones*, *4*(2), 13. https://doi.org/10.3390/drones4020013

Kane, D. L., Hinkel, K. M., Goering, D. J., Hinzman, L. D., & Outcalt, S. I. (2001). Non-conductive heat transfer associated with frozen soils. *Global and Planetary Change*, *29*(3), 275–292. https://doi.org/10.1016/S0921-8181(01)00095-9

Kang, K., Kim, D., Kim, Y., Lee, E., Kim, B.-G., Kim, S. H., Ha, K., Koh, D.-C., Cho, Y.-K., & Kim, G. (2019). Quantitative estimation of submarine groundwater discharge using airborne thermal infrared data acquired at two different tidal heights. *Hydrological Processes*, *33*(7), 1089–1100. https://doi.org/10.1002/hyp.13387

Kanno, Y., Vokoun, J. C., & Letcher, B. H. (2013). Paired stream–air temperature measurements reveal fine-scale thermal heterogeneity within headwater brook trout stream networks. *River Research and Applications*, *30*(6), 745–755. https://doi.org/10.1002/rra.2677

KarisAllen, J. J., & Kurylyk, B. L. (2021). Drone-based characterization of intertidal spring cold-water plume dynamics. *Hydrological Processes*, *35*(6), e14258. https://doi.org/10.1002/hyp.14258

Kazemi, H., Seth, M. S., & Thomas, G. W. (1969). Pressure transient analysis of naturally fractured reservoirs with uniform fracture distribution. *Society of Petroleum Engineers Journal*, *9*(04), 451–462. https://doi.org/10.2118/2156-A

Kelly, J., Kljun, N., Olsson, P.-O., Mihai, L., Liljeblad, B., Weslien, P., Klemedtsson, L., & Eklundh, L. (2019). Challenges and best practices for deriving temperature data from an uncalibrated UAV thermal infrared camera. *Remote Sensing*, *11*. https://doi.org/10.3390/rs11050567

Kelly, J. L., Dulai, H., Glenn, C. R., & Lucey, P. G. (2019). Integration of aerial infrared thermography and in situ radon-222 to investigate submarine groundwater discharge to Pearl Harbor, Hawaii, USA. *Limnology and Oceanography*, *64*(1). https://doi.org/10.1002/lno.11033

Kelly, J. L., Glenn, C. R., & Lucey, P. G. (2013). High-resolution aerial infrared mapping of groundwater discharge to the coastal ocean. *Limnology and Oceanography: Methods*, *11*(5), 262–277. https://doi.org/10.4319/lom.2013.11.262

Kjerfve, B. (1994). *Coastal lagoon processes*. Elsevier.

Kjerfve, B., & Magill, K. E. (1989). Geographic and hydrodynamic characteristics of shallow coastal lagoons. *Marine Geology*, *88*(3), 187–199. https://doi.org/10.1016/0025-3227(89)90097-2

Kruseman, G. P., & de Ridder, N. A. (2000). *Analysis and evaluation of pumping test data* (2nd ed.). International Institue for Land Reclamation and Improvement.

Kübler, J, E., & Davison, I, R. (1993). High-temperature tolerance of photosynthesis in the red alga Chondrus crispus. *Marine Biology*, *117*(2), 327–335. https://doi.org/10.1007/BF00345678

Kurylyk, B. L., Bourque, C. P.-A., & MacQuarrie, K. T. B. (2013). Potential surface temperature and shallow groundwater temperature response to climate change: An example from a small forested catchment in east-central New Brunswick (Canada). *Hydrology and Earth System Sciences*, *17*(7), 2701–2716. https://doi.org/10.5194/hess-17-2701-2013

Kurylyk, B. L., MacQuarrie, K. T. B., Caissie, D., & McKenzie, J. M. (2015). Shallow groundwater thermal sensitivity to climate change and land cover disturbances: Derivation of analytical expressions and implications for stream temperature modeling. *Hydrology and Earth System Sciences*, *19*(5), 2469–2489. https://doi.org/10.5194/hess-19-2469-2015

Kurylyk, B. L., MacQuarrie, K. T. B., & Voss, C. I. (2014). Climate change impacts on the temperature and magnitude of groundwater discharge from shallow, unconfined aquifers. *Water Resources Research*, *50*(4), 3253–3274. https://doi.org/10.1002/2013WR014588

Kurylyk, B. L., Moore, R. D., & MacQuarrie, K. T. B. (2016). Scientific briefing: Quantifying streambed heat advection associated with groundwater–surface water interactions. *Hydrological Processes*, *30*(6), 987–992. https://doi.org/https://doi.org/10.1002/hyp.10709

Kylin, H. (1917). 36. Harald Kylin: Über die kälteresistenz der meeresalgen. *Berichte Der Deutschen Botanischen Gesellschaft*, *35*(4), 370–384. https://doi.org/10.1111/j.1438-8677.1917.tb07186.x

Lappala, E. G., Healy, R. W., & Weeks, E. (1987). *Documentation of computer program VS2D to solve the equations of fluid flow in variably saturated porous media* (Water-Resources Investigations Report 83-4099). U.S. Geological Survey. https://doi.org/10.3133/wri834099

LeBlanc, N., Landry, T., Davidson, J., Tremblay, R., & McNiven, M. (2010). *The effect of elevated water temperature stress on the mussel Mytilus edulis (L.), survival and genetic characteristics* (Canadian Technical Report of Fisheries and Aquatic Sciences 2900). Fisheries and Oceans Canada. https://publications.gc.ca/collections/collection_2011/mpo-dfo/Fs97-6-2900-eng.pdf

LeBlanc, N., Landry, T., Stryhn, H., Tremblay, R., McNiven, M., & Davidson, J. (2005). The effect of high air and water temperature on juvenile Mytilus edulis in Prince Edward Island, Canada. *Aquaculture*, *243*(1–4), 185–194. https://doi.org/10.1016/j.aquaculture.2004.09.035

Lee, E., Kang, K., Hyun, S. P., Lee, K.-Y., Yoon, H., Kim, S. H., Kim, Y., Xu, Z., Kim, D., Koh, D.-C., & Ha, K. (2016). Submarine groundwater discharge revealed by aerial thermal infrared imagery: a case study on Jeju Island, Korea. *Hydrological Processes*, *30*(19), 3494–3506. https://doi.org/10.1002/hyp.10868

Lemmen, D. S., Warren, F. J., James, T. S., & Mercer Clarke, C. S. L. (2016). *Canada's marine coasts in a changing climate*. Government of Canada. https://www.nrcan.gc.ca/sites/www.nrcan.gc.ca/files/earthsciences/files/pdf/NRCAN_fullBook accessible.pdf

Li, Q., Peng, Y., Wang, G., Wang, H., Xue, B., & Hu, X. (2019). A combined method for estimating continuous runoff by parameter transfer and drainage area ratio method in ungauged catchments. *Water*, *11*(5), 1104. https://doi.org/10.3390/w11051104

Li, Y., Zhao, M., Mildrexler, D. J., Motesharrei, S., Mu, Q., Kalnay, E., Zhao, F., Li, S., & Wang, K. (2016). Potential and actual impacts of deforestation and afforestation on land surface temperature. *Journal of Geophysical Research: Atmospheres*, *121*(24), 14,314-372,386. https://doi.org/10.1002/2016JD024969

Lüning, K., Guiry, M. D., & Masuda, M. (1986). Upper temperature tolerance of North Atlantic and North Pacific geographical isolates of Chondrus species (Rhodophyta). *Helgoländer Meeresuntersuchungen*, *41*(3), 297–306. https://doi.org/10.1007/BF02366194

Ma, D. H., Zhang, J. B., Lai, J. B., & Wang, Q. J. (2016). An improved method for determining Brooks-Corey model parameters from horizontal absorption. *Geoderma*, *263*, 122–131. https://doi.org/10.1016/j.geoderma.2015.09.007

MacDougall, A. H., & Beltrami, H. (2017). Impact of deforestation on subsurface temperature profiles: implications for the borehole paleoclimate record. *Environmental Research Letters*, *12*(7), 74014. https://doi.org/10.1088/1748-9326/aa7394

MacDougall, J. I., & Veer, C. (1981). *Soils of Prince Edward Island: preliminary report of the soil survey of Prine Edward Island* (Report Number pe141). Agriculture Canada. http://sis.agr.gc.ca/cansis/publications/surveys/pe/index.html

MacDougall, J. I., Veer, C., & Wilson, F. (1988). *Soil of Prince Edward Island: Prince Edward Island soil survey* (Report Number pe83-54). Agriculture Canada. https://sis.agr.gc.ca/cansis/publications/surveys/pe/pe83-54/index.html

Mace, R. E. (1997). Determination of transmissivity from specific capacity tests in a karst aquifer. *Groundwater*, *35*(5), 738–742. https://doi.org/10.1111/j.1745-6584.1997.tb00141.x

Mace, R. E. (2001). *Estimating transmissivity using specific-capacity data* (Geological Circular 01-2). Bureau of Economic Geology. https://doi.org/10.23867/gc0102D

Maliva, R. (2016). *Aquifer characterization techniques* (1st ed.). Springer, Cham. https://doi.org/10.1007/978-3-319-32137-0

Mareschal, J.-C., & Beltrami, H. (1992). Evidence for recent warming from perturbed geothermal gradients: Examples from eastern Canada. *Climate Dynamics*, *6*(3), 135–143. https://doi.org/10.1007/BF00193525

Martínez-Alvarez, V., Gallego-Elvira, B., Maestre-Valero, J. F., & Tanguy, M. (2011). Simultaneous solution for water, heat and salt balances in a Mediterranean coastal lagoon (Mar Menor, Spain). *Estuarine, Coastal and Shelf Science*, *91*(2), 250–261. https://doi.org/10.1016/j.ecss.2010.10.030

Mathieson, A. C., & Burns, R. L. (1971). Ecological studies of economic red algae. I. Photosynthesis and respiration of Chondrus crispus Stackhouse and Gigartina stellata (stackhouse) batters. *Journal of Experimental Marine Biology and Ecology*, *7*(2), 197–206. https://doi.org/10.1016/0022-0981(71)90031-1

Mayer, T. D. (2012). Controls of summer stream temperature in the Pacific Northwest. *Journal of Hydrology*, *475*, 323–335. https://doi.org/10.1016/j.jhydrol.2012.10.012

Mcmillan, H., Krueger, T., & Freer, J. (2012). Benchmarking observational uncertainties for hydrology: Rainfall, river discharge and water quality. *Hydrological Processes*, *26*(26), 4078–4111. https://doi.org/10.1002/hyp.9384

Meisner, J. D., Rosenfeld, J. S., & Regier, H. A. (1988). The role of groundwater in the impact of climate warming on stream salmonines. *Fisheries*, *13*(3), 2–8. https://doi.org/10.1577/1548-8446(1988)013<0002:TROGIT>2.0.CO;2

Menberg, K., Blum, P., Kurylyk, B. L., & Bayer, P. (2014). Observed groundwater temperature response to recent climate change. *Hydrol. Earth Syst. Sci.*, *18*(11), 4453–4466. https://doi.org/10.5194/hess-18-4453-2014

Menció, A., Casamitjana, X., Mas-Pla, J., Coll, N., Compte, J., Martinoy, M., Pascual, J., & Quintana, X. D. (2017). Groundwater dependence of coastal lagoons: The case of La Pletera salt marshes (NE Catalonia). *Journal of Hydrology*, *552*, 793–806. https://doi.org/10.1016/j.jhydrol.2017.07.034

Meyboom, P. (1967). *Groundwater studies in the Assiniboine River drainage basin: part II. Hydrologic characteristics of phreatophytic vegetation in south-central Saskatchewan* (Bulletin 139). Geological Survey of Canada. https://doi.org/10.4095/101495

Mitchell, W. D. (1954). *Stage-fall-discharge relations for steady flow in prismatic channels* (Water Supply Paper 1164). U.S. Geological Survey. https://doi.org/10.3133/wsp1164

Mohammed, A. A. (2019). *Measurement and simulation of preferential flow in frozen soils* [Doctoral dessertation, University of Calgary]. http://hdl.handle.net/1880/111213%0D

Mohammed, A. A., Schincariol, R. A., Quinton, W. L., Nagare, R. M., & Flerchinger, G. (2017). On the use of mulching to mitigate permafrost thaw due to linear disturbances in sub-arctic peatlands. *Ecological Engineering*, *102*, 207–223. https://doi.org/https://doi.org/10.1016/j.ecoleng.2017.02.020

Mohamoud, Y. M. (2008). Prediction of daily flow duration curves and streamflow for ungauged catchments using regional flow duration curves. *Hydrological Sciences Journal*, *53*(4), 706–724. https://doi.org/10.1623/hysj.53.4.706

Moriasi, D. N., Arnold, J. G., Liew, M. W. Van, Bingner, R. L., Harmel, R. D., & Veith, T. L. (2007). Model evaluation guidelines for systematic quantification of accuracy in watershed simulations. *Transactions of the ASABE*, *50*(3), 885–900. https://doi.org/10.13031/2013.23153

Mundy, E., Gleeson, T., Roberts, M., Baraer, M., & McKenzie, J. M. (2017). Thermal imagery of groundwater seeps: possibilities and limitations. *Groundwater*, *55*(2), 160–170. https://doi.org/10.1111/gwat.12451

Nav Canada. (2000). *The weather of Atlantic Canada and Eastern Quebec - Chapter 3 weather patterns*. http://www.navcanada.ca/EN/media/Publications/Local Area Weather Manuals/LAWM-Atlantic-3-EN.pdf

Novaczek, I., & Breeman, A. M. (1990). Thermal ecotypes of amphi-Atlantic algae. II. Cold-temperate species (Furcellaria lumbricalis and Polyides rotundus). *Helgoländer Meeresuntersuchungen*, *44*(3–4), 475–485. https://doi.org/10.1007/BF02365481

Ozotta, O., & Gerla, P. (2018). *Using thermal imaging to characterize groundwater seepage in a North Dakota fen* [Master's Thesis, University of North Dekota]. https://commons.und.edu/theses/2424

Parsons, M. L. (1970). Groundwater thermal regime in a glacial complex. *Water Resources Research*, *6*(6), 1701–1720. https://doi.org/10.1029/WR006i006p01701

Pasha, E. (2018). *Quantifying groundwater recharge during dynamic seasonality in cold climates* [Master's Thesis, University of Waterloo]. http://hdl.handle.net/10012/12883

PEI Dept. Env. (2000a). *Corporate land use inventory 2000 [GIS layer for Prince Edward Island]*. http://www.gov.pe.ca/gis/index.php3?number=1011269&lang=E

PEI Dept. Env. (2000b). *PEI corporate land use inventory 2000: Land use and subuse codes*. http://www.gov.pe.ca/gis/CLUI2000.htm

PEI Dept. Env. (2002). *1973 surficial geology [GIS layer for Prince Edward Island]*. http://www.gov.pe.ca/gis/index.php3?number=1021412&lang=E

PEI Dept. Env. (2008). *2 Meter contours [GIS layer for Prince Edward Island]*.

http://www.gov.pe.ca/gis/index.php3?number=1011267&lang=E

Pix4D. (2020). *GSD calculator [Excel workbook tool]*. https://support.pix4d.com/hc/en-us/articles/202560249-TOOLS-GSD-calculator

Pluhowski, E. J. (1972). *Hydrologic interpretations based on infrared imagery of Long Island, New York* (Water Supply Paper 2009-B). U.S. Geological Survey. https://doi.org/10.3133/wsp2009B

Prest, V. K. (1973a). *Glacial indicators map of Prince Edward Island ["A" Series Map 1366A]*. Geological Survey of Canada.

Prest, V. K. (1973b). *Surficial deposits of Prince Edward Island ["A" Series Map 1366A]*. Geological Survey of Canada.

Prince, J. S., & Kingsbury, J. M. (1973). The ecology of Chondrus crispus at Plymouth, Massachusetts. III. Effect of elevated temperature on growth and survival. *The Biological Bulletin*, *145*(3), 580–588. https://doi.org/10.2307/1540638

Rantz, S. E., Barnes, H. H., Carter, R. W., Smoot, G. F., Matthai, H. F., Pendleton, A. F., Hulsing, H., Bodhaine, G. L., Davidian, J., & others. (1982a). *Measurement and computation of streamflow: Volume 1 - Measurement of stage and discharge* (Water Supply Paper 2175; Vol. 1). U.S. Geological Survey. https://doi.org/doi:10.3133/wsp2175

Rantz, S. E., Barnes, H. H., Carter, R. W., Smoot, G. F., Matthai, H. F., Pendleton, A. F., Hulsing, H., Bodhaine, G. L., Davidian, J., & others. (1982b). *Measurement and computation of streamflow: Volume 2 - Computation of discharge* (Water Supply Paper 2175; Vol. 2). U.S. Geological Survey. https://doi.org/doi:10.3133/wsp2175

Raven, J. A., & Geider, R. J. (1988). Temperature and algal growth. *The New Phytologist*, *110*(4), 441–461. http://www.jstor.org/stable/2434905

Read, K. R. H., & Cumming, K. B. (1967). Thermal tolerance of the bivalve molluscs Modiolus modiolus L., Mytilus edulis L. and Brachidontes demissus dillwyn. *Comparative Biochemistry and Physiology*, *22*(1), 149–155. https://doi.org/10.1016/0010-406X(67)90176-4

Renard, P. (2017). Hytool: an open source matlab toolbox for the interpretation of hydraulic tests using analytical solutions. *Journal of Open Source Software*, *2*(19), 441. https://doi.org/10.21105/joss.00441

Riedel, T. (2019). Temperature-associated changes in groundwater quality. *Journal of Hydrology*, *572*, 206–212. https://doi.org/https://doi.org/10.1016/j.jhydrol.2019.02.059

Rivera, A. (2014). *Canada's groundwater resources*. Fitzhenry & Whiteside. https://doi.org/10.4095/293431

Rodríguez-Rodríguez, M., & Moreno-Ostos, E. (2006). Heat budget, energy storage and hydrological regime in a coastal lagoon. *Limnologica*, *36*(4), 217–227. https://doi.org/https://doi.org/10.1016/j.limno.2006.05.003

Roseen, R. M. (2002). *Quantifying groundwater discharge using thermal imagery and conventional groundwater exploration techniques for estimating the nitrogen loading to a meso-scale estuary* [Doctoral dissertation, University of New Hampshire]. https://scholars.unh.edu/dissertation/77

Ryan, D., Heap, A. D., Radke, L., & Heggie, D. T. (2003). *Conceptual models of Australia's estuaries and coastal waterways: Applications for coastal resource management* (Record 2003/09). Geoscience Australia.

Sadat-Noori, M., Santos, I. R., Tait, D. R., McMahon, A., Kadel, S., & Maher, D. T. (2016). Intermittently closed and open lakes and/or lagoons (ICOLLs) as groundwater-dominated coastal systems: Evidence from seasonal radon observations. *Journal of Hydrology*, *535*, 612–624. https://doi.org/10.1016/j.jhydrol.2016.01.080

Sawyer, A. H., Michael, H. A., & Schroth, A. W. (2016). From soil to sea: The role of groundwater in coastal critical zone processes. *WIREs Water*, *3*(5), 706–726. https://doi.org/https://doi.org/10.1002/wat2.1157

Schwartz, F. W., & Zhang, H. (2003). *Fundamentals of ground water*. John Wiley & Sons, Inc.

Seuront, L., Nicastro, K. R., Zardi, G. I., & Goberville, E. (2019). Decreased thermal tolerance under recurrent heat stress conditions explains summer mass mortality of the blue mussel Mytilus edulis. *Scientific Reports*, *9*, 1–14. https://doi.org/http://dx.doi.org/10.1038/s41598-019-53580-w

Sharp, G., Semple, R., Connolly, K., Blok, R., Audet, D., Cairns, D., & Courtenay, S. (2003). *Ecological assessment of the Basin Head lagoon: A proposed Marine Protected Area* (Canadian Manuscript Report of Fisheries and Aquatic Sciences 2641). Fisheries and Oceans Canada.

Silliman, S. E., & Booth, D. F. (1993). Analysis of time-series measurements of sediment temperature for identification of gaining vs. losing portions of Juday Creek, Indiana. *Journal of Hydrology*, *146*, 131–148. https://doi.org/https://doi.org/10.1016/0022-1694(93)90273-C

Singh, J., Knapp, H. V., & Demissie, M. (2004). *Hydrologic Modelling of the Iroquois River watershed using HSPF and SWAT* (Contract Report 2004-08). Illinois State Water Survey. https://swat.tamu.edu/media/90101/singh.pdf

Sparks, A. (2018). Nasapower: A NASA POWER global meteorology, surface solar energy and climatology data client for R. *Journal of Open Source Software*, *3*(30), 1035. https://doi.org/10.21105/joss.01035

Stone, M. L., Rasmussen, T. J., Bennet, T. J., Poulton, B. C., & Ziegler, A. C. (2012). *Protocols for collection of streamflow, water-quality, fish, and habitat data to describe stream quality for the hydrobiological monitoring program*. https://doi.org/10.3133/ofr20121055

Szczypta, C., Gascoin, S., Houet, T., Hagolle, O., Dejoux, J. F., Vigneau, C., & Fanise, P. (2015). Impact of climate and land cover changes on snow cover in a small Pyrenean catchment. *Journal of Hydrology*, *521*, 84–99. https://doi.org/10.1016/j.jhydrol.2014.11.060

Tamborski, J. J., Rogers, A. D., Bokuniewicz, H. J., Cochran, J. K., & Young, C. R. (2015). Identification and quantification of diffuse fresh submarine groundwater discharge via airborne thermal infrared remote sensing. *Remote Sensing of Environment*, *171*(15), 202–217. https://doi.org/10.1016/j.rse.2015.10.010

Taniguchi, M., Dulai, H., Burnett, K. M., Santos, I. R., Sugimoto, R., Stieglitz, T., Kim, G., Moosdorf, N., & Burnett, W. C. (2019). Submarine groundwater discharge: Updates on its measurement techniques, geophysical drivers, magnitudes, and effects. *Frontiers in Environmental Science*, *7*, 141. https://doi.org/10.3389/fenvs.2019.00141

Taniguchi, M., Uemura, T., & Jago-on, K. (2007). Combined Effects of Urbanization and Global Warming on Subsurface Temperature in Four Asian Cities. *Vadose Zone Journal*, *6*(3), 591–596. https://doi.org/https://doi.org/10.2136/vzj2006.0094

Taniguchi, M., Williamson, D. R., & Peck, A. J. (1999). Disturbances of temperature-depth profiles due to surface climate change and subsurface water flow: 1. An effect of linear increase in surface temperature caused by global warming and urbanization in the Tokyo metropolitan area, Japan. *Water Resources Research*, *35*(5), 1519–1529. https://doi.org/10.1029/1998WR900010

Tasende, M. A., & Fraga, M. I. (1992). Efecto de las condiciones de cultivo en la germinación de esporas de Chondrus crispus stackh, (Gigartinales, Rhodophyta). *Cahiers de Biologie Marine*, *33*(4), 407–415.

Taylor, C. A., & Stefan, H. G. (2009). Shallow groundwater temperature response to climate change and urbanization. *Journal of Hydrology*, *375*(3), 601–612. https://doi.org/https://doi.org/10.1016/j.jhydrol.2009.07.009

Theis, C. V. (1935). The relation between the lowering of the piezometric surface and the rate and duration of discharge of a well using ground-water storage. *Eos, Transactions American Geophysical Union*, *16*(2), 519–524. https://doi.org/10.1029/TR016i002p00519

Thomasson Jr., H. G., Olmsted, F. H., & LeRoux, E. F. (1960). *Geology, water resources and usable ground-water storage capacity of part of Solano County, California* (Water Supply Paper 1464; 2nd ed.). U.S. Geological Survey. https://doi.org/10.3133/wsp1464

Tibbet, W. N. (2015). *An investigation of groundwater and surface water interactions near a small stream in Prince Edward Island* [Master's thesis, University of New Brunswick]. https://unbscholar.lib.unb.ca/islandora/object/unbscholar%3A8259/datastream/PDF/view

Turnipseed, D. P., & Sauer, V. B. (2010). Discharge measurements at gaging stations (Techniques and Methods 3-A8). In *Techniques of Water-Resources Investigations of the United States Geological Survey*. http://pubs.er.usgs.gov/browse/usgs-publications

USGS. (2017). *Landsat 8 (L8) data users handbook version 5.0 (LSDS-1574)*. https://www.usgs.gov/core-science-systems/nli/landsat/landsat-8-data-users-handbook

van de Poll, H. W. (1989). Lithostratigraphy of the Prince Edward Island redbeds. *Atlantic Geology*, *25*, 23–35. https://doi.org/10.4138/1668

Voldoire, A., Sanchez-Gomez, E., Mélia, D., Decharme, B., Cassou, C., Senesi, S., Valcke, S., Beau, I., Alias, A., Chevallier, M., Déqué, M., Deshayes, J., Douville, H., Fernandez, E., Madec, G., Maisonnave, E., Moine, M.-P., Planton, S., Saint-Martin, D., & Chauvin, F. (2013). The CNRM-CM5.1 global climate model: Description and basic evaluation. *Climate Dynamics*, *40*, 2091–2121. https://doi.org/10.1007/s00382-011-1259-y

Warner, S. (2016). *Assessing the potential impact of climate change on the surface hydrology of Prince Edward Island* [Master's thesis, Dalhousie University]. http://hdl.handle.net/10222/72317

Warren, J. E., & Root, P. J. (1963). The behaviour of naturally fractured reservoirs. *Society of Petroleum Engineers Journal*, *3*(3), 245–255. https://doi.org/10.2118/426-PA

Xing, X., Wang, H., & Ma, X. (2018). Brooks-Corey modeling by one-dimensional vertical infiltration method. *Water*, *10*(5), 593. https://doi.org/10.3390/w10050593

Yukimoto, S., Adachi, Y., Hosaka, M., Sakami, T., Yoshimura, H., Hirabara, M., Tanaka, T. Y., Shindo, E., Tsujino, H., Deushi, M., Mizuta, R., Yabu, S., Obata, A., Nakano, H., Koshiro, T., Ose, T., & Kitoh, A. (2012). A new global climate model of the Meteorological Research Institute: MRI-CGCM3 - Model description and basic performance. *Journal of the Meteorological Society of Japan. Ser. II*, *90A*, 23–64. https://doi.org/10.2151/jmsj.2012-A02

Zamora, P. B., Cardenas, M. B., Lloren, R., & Siringan, F. P. (2017). Seawater-groundwater mixing in and fluxes from coastal sediment overlying discrete fresh seepage zones: A modeling study. *Journal of Geophysical Research: Oceans*, *122*(8), 6565–6582. https://doi.org/10.1002/2017JC012769

Zebarth, B. J., Danielescu, S., Nyiraneza, J., Ryan, M. C., Jiang, Y., Grimmett, M., & Burton, D. L. (2015). Controls on nitrate loading and implications for BMPs under intensive potato production systems in Prince Edward Island, Canada. *Groundwater Monitoring and Remediation*, *35*(1), 30–42. https://doi.org/10.1111/gwmr.12088

Zhang, T. (2005). Influence of the seasonal snow cover on the ground thermal regime: An overview. *Reviews of Geophysics*, *43*(4). https://doi.org/https://doi.org/10.1029/2004RG000157

APPENDIX A: ADDITIONAL SITE MAPS

Source: Esri, DigitalGlobe, GeoEye, Earthstar Geographics, CNES/Airbus DS, USDA, USGS, AeroGRID, IGN, and the GIS User Community

Figure 32. Topography and drainage patterns of the Kingsboro watershed. The area is generally gently sloping (2-5% slopes), with the steepest portions being located along the shore. The maximum elevation is approximately 60 metres. Topography data was sourced from the PEI Dept. Env. (2008). Map prepared in ArcGIS Pro (Version 2.3.3, 2018).

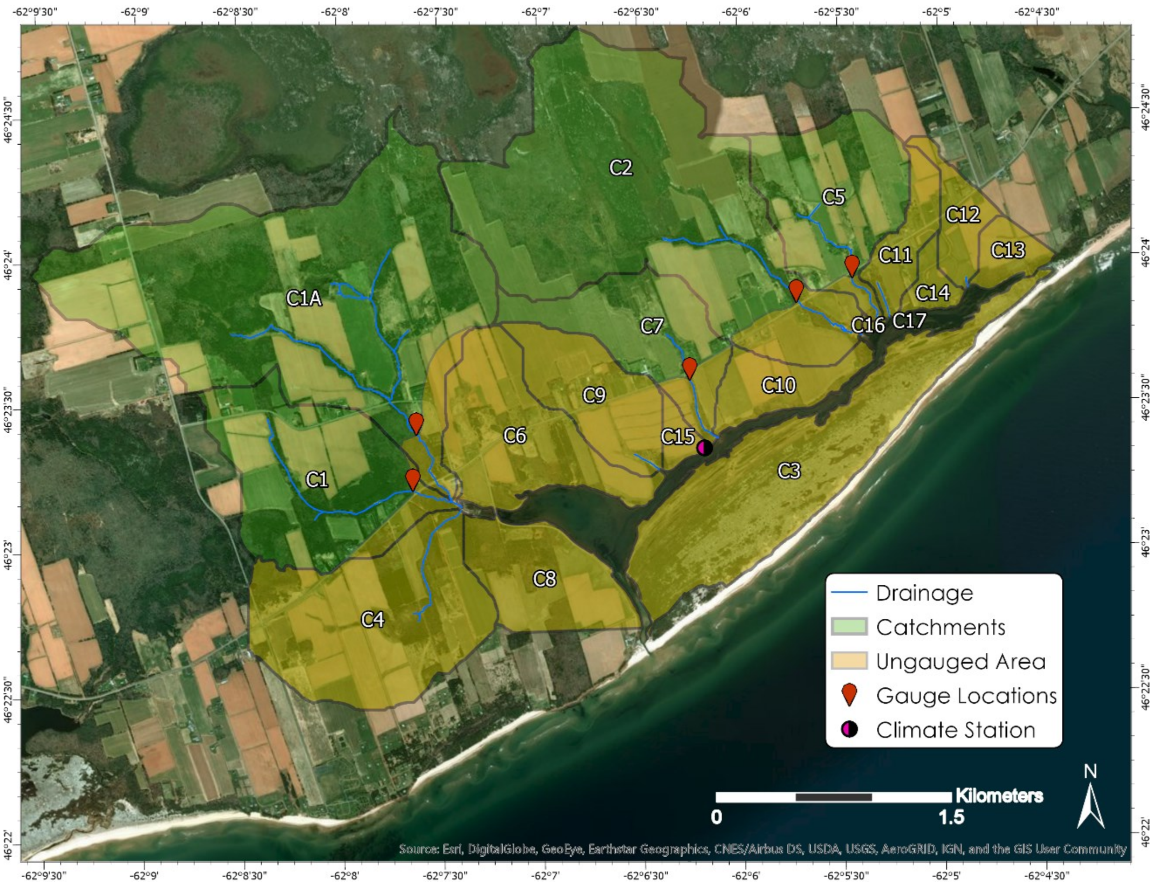

Figure 33. Gauged and ungauged areas of the Kingsboro watershed. Stream discharge was measured at the locations indicated in red during 2019 and 2020. Stage-discharge relationships were developed using stilling wells installed in Streams C1, C1A, C2, and C5. The subcatchments are divided into areas that likely supplied water to gauged sites ("Catchments"; 55% of area) and those which were downstream of flow measurements ("Ungauged Area"; 45% of area). Map prepared in ArcGIS Pro (Version 2.3.3, 2018).

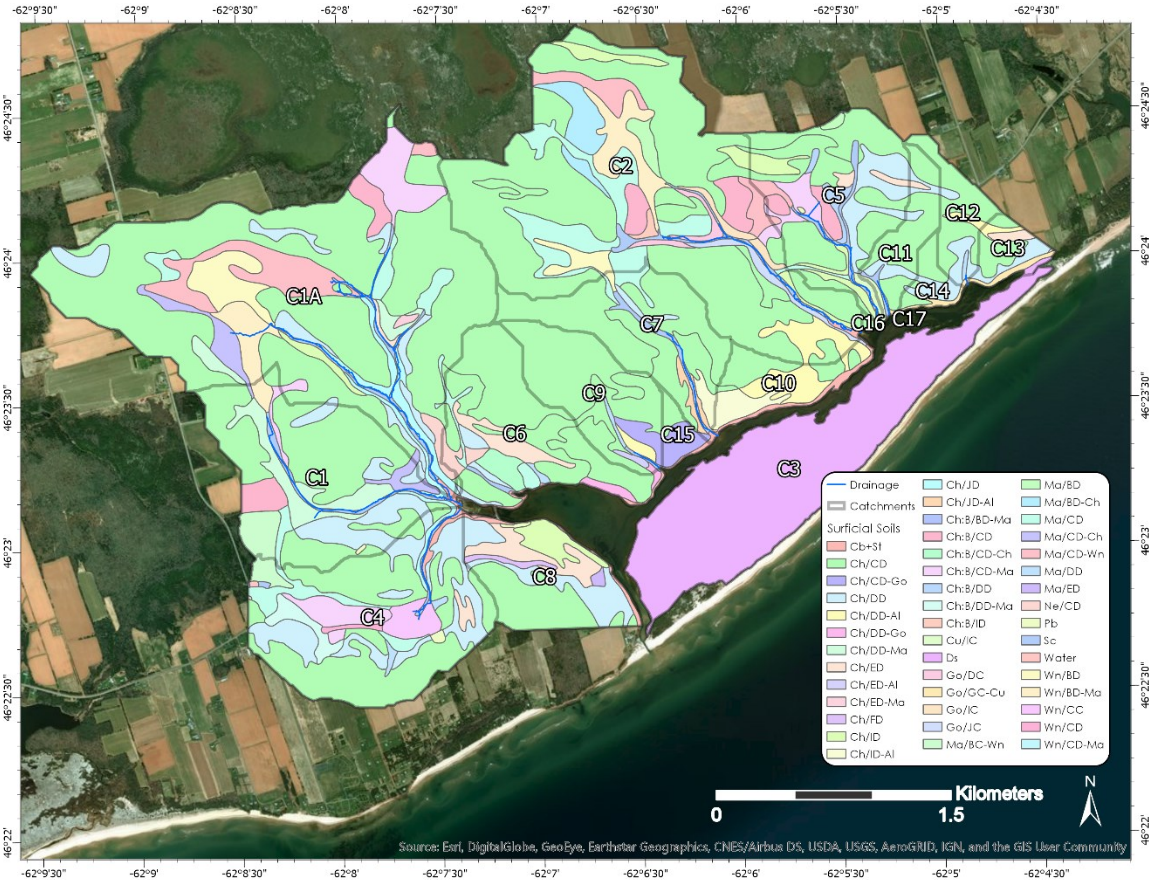

Source: Esri, DigitalGlobe, GeoEye, Earthstar Geographics, CNES/Airbus DS, USDA, USGS, AeroGRID, IGN, and the GIS User Community

Figure 34. Surficial soil layers of the Kingsboro watershed (PEI Dept. Env., 2002). The most ubiquitous soil type is the Charlottetown soil series, which covers approximately 74% of the watershed (i.e., the Ch/CD map unit shown in green). This soil is most frequently found with slopes between 2-5% and a fine sandy loam or very fine sandy loam texture. Soil codes in this map are too numerous to list here, but are freely available from the Government of PEI website (n.d.). Map prepared in ArcGIS Pro (Version 2.3.3, 2018).

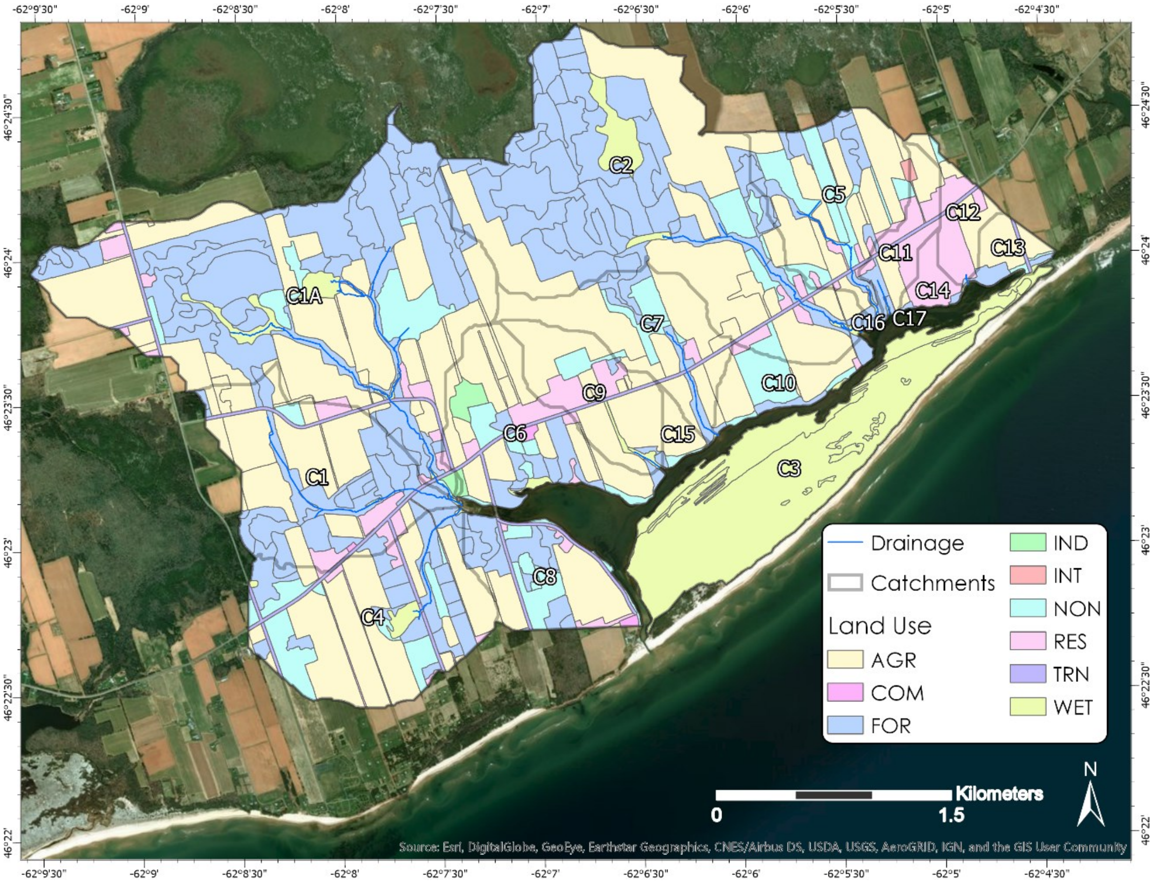

Figure 35. The land use inventory geospatial layer for the Kingsboro watershed (PEI Dept. Env., 2000a). AGR = Agriculture; COM = Commercial; FOR = Forestry; IND = Industrial; INT = Institutional; NON = Non-evident; Res = Residential; TRN = Transportation (roadways); and WET = Wetland. Map prepared in ArcGIS Pro (Version 2.3.3, 2018).

Sources: Esri, DigitalGlobe, GeoEye, Earthstar Geographics, CNES/Airbus DS, USDA, USGS, AeroGRID, IGN, and the GIS User Community

Figure 36. Well logs within the Kingsboro watershed that the provincial authority has on record (i.e., 9 pink triangles), as well as the record of civic addresses in the area (i.e., 127 blue circles). This map, coupled with the most recent land use inventory displayed in Figure 35, suggest that several wells are unaccounted for. Map prepared in ArcGIS Pro (Version 2.3.3, 2018).

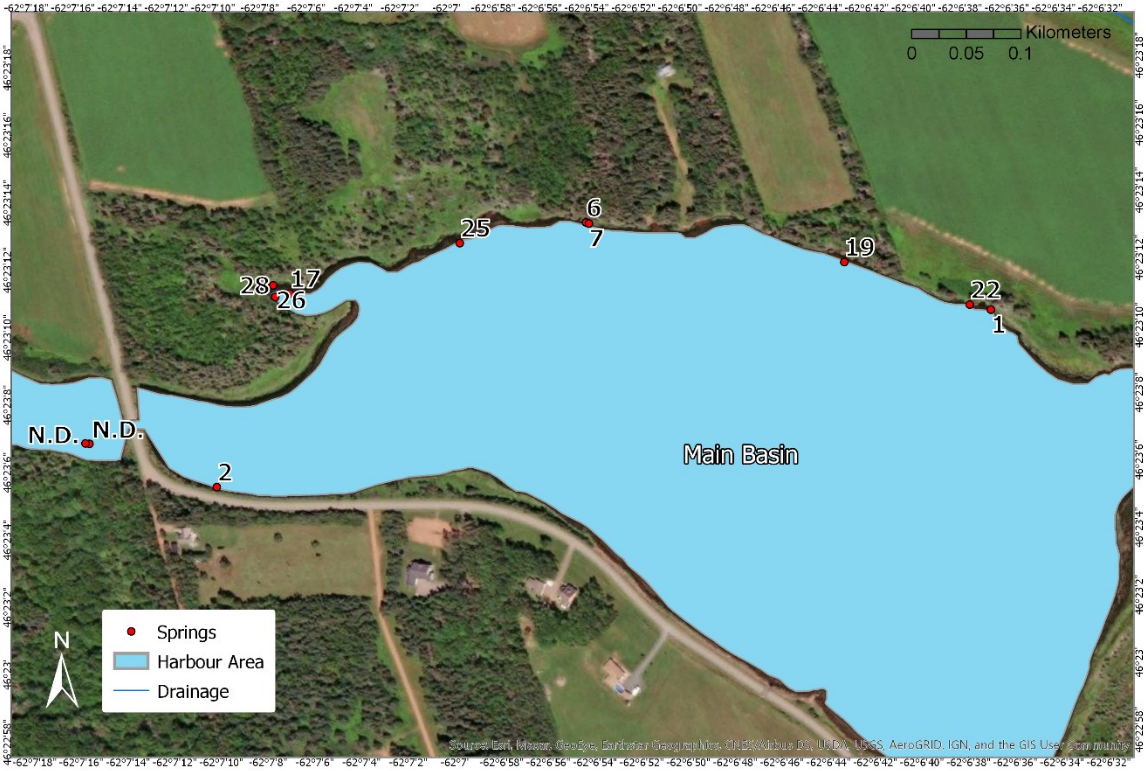

Figure 37. (Series image 2 of 4) Locations and IDs of springs in main basin of Basin Head Harbour. N.D. = No Data. Map prepared in ArcGIS Pro (Version 2.3.3, 2018).

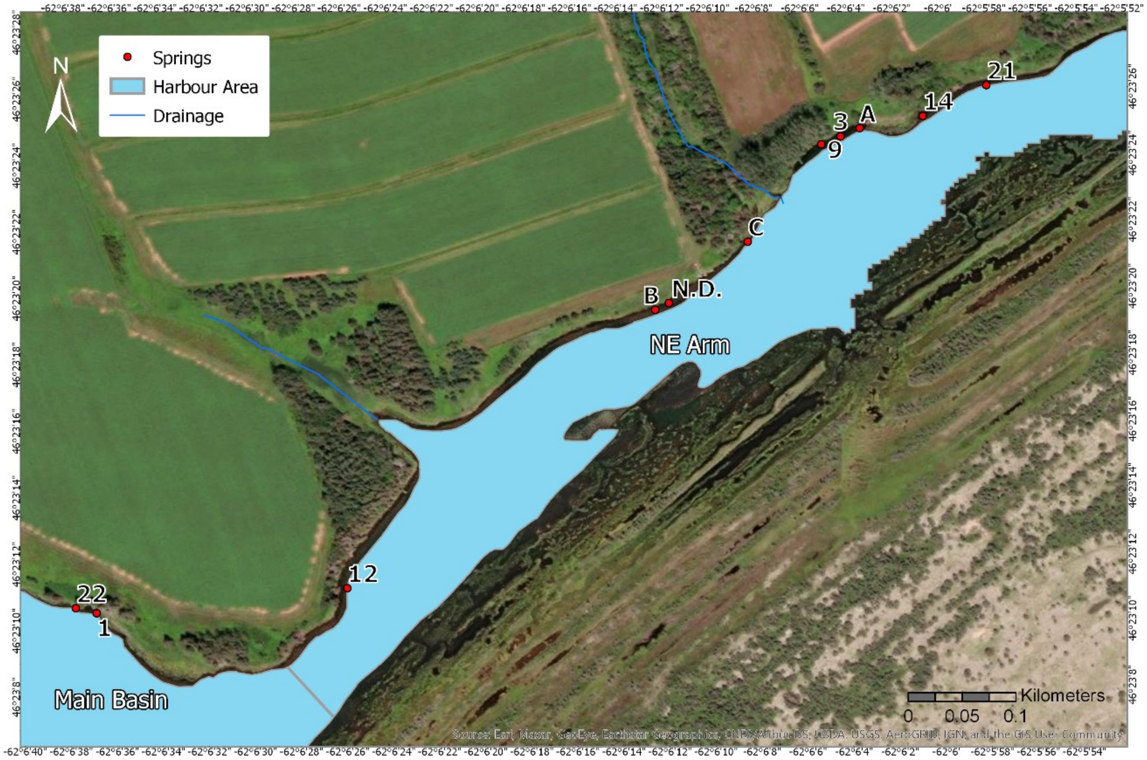

Figure 38. (Series image 3 of 4) Locations and IDs of springs in the main basin and northeast arm (NE Arm) of Basin Head Harbour. N.D. = No Data. Map prepared in ArcGIS Pro (Version 2.3.3, 2018).

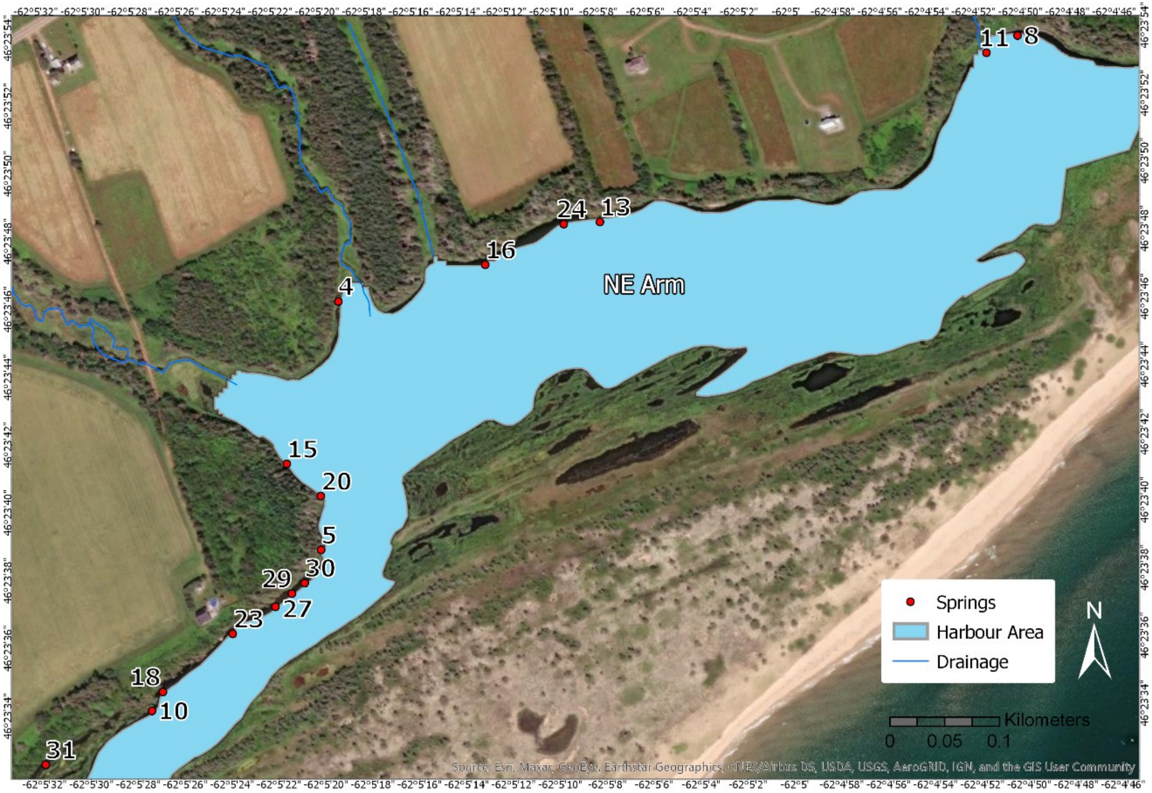

Figure 39. (Series image 4 of 4) Locations and IDs of springs in the upper northeast arm (NE Arm) of Basin Head Harbour. Map prepared in ArcGIS Pro (Version 2.3.3, 2018).

APPENDIX B: SUPPLEMENTARY MATERIAL

Section 1 – Irish Moss Ecophysiology Supplement

This section provides supplemental information on Irish moss and blue mussel ecophysiological studies to supplement Chapter 1, Section 1.2 in the main body of the report.

The life cycle of a typical morphotype of *C. crispus* is portrayed in Figure 40 for reference.

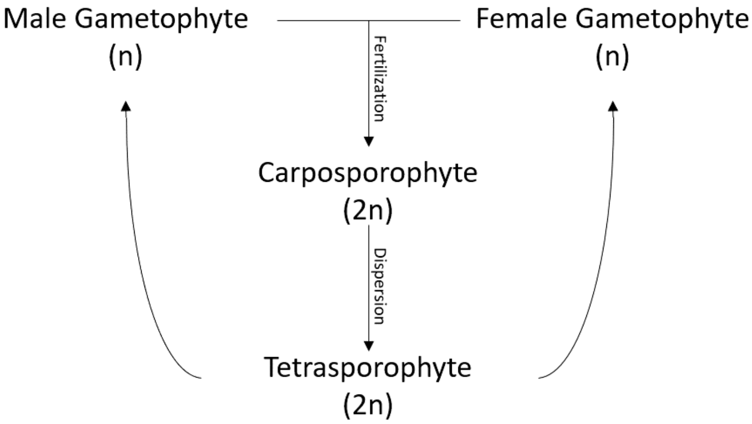

Figure 40. Outline of the major morphological stages of the red algae Chondrus crispus. Gametes combine through fertilisation to produce a carpospore. The carpospore replicates itself by mitosis and disperses to form tetrasporophytes. Tetrasporophytes generate and release gametes by meiosis, which grow into free standing aquatic plants. The variable n refers to number of chromosomes (n = 30 for C. crispus). Figure based on content available in Sharp et al. (2003).

The Irish moss found in the NE Arm of BHH is morphologically and reproductively unique with respect to other types reported in the literature (Sharp et al., 2003). The fronds are much broader, with fewer dichotomies than the typical PEI Irish moss, so it was named giant Irish moss (GIM) (Sharp et al., 2003). Typical Irish moss exhibits colour changes throughout the summer months, whereas GIM maintains a dark colouration throughout the year (Sharp et al., 2003). When removed from BHH for growth elsewhere, the unique morphology and colouration of the moss is not maintained, and the growth rate increases (DFO, 2009; Sharp et al., 2003). This behaviour suggests some level of environmental control over these properties. Another unique property of GIM is that it is found exclusively in the gametophyte phase and reproduces solely by asexual fragmentation (Sharp et al., 2003). The particularly high nitrogen content in the tissue of GIM fronds causes excessive fragmentation and loss (DFO, 2009), which may make it particularly susceptible to mechanical stressors. In addition to high nutrient content, GIM also has an uncommonly high concentration of carrageenan, which is a harvestable thickening agent used in various consumer products (DFO, 2009). Finally, the ability of GIM to anchor themselves to substrates has atrophied, and they are dependent on the byssal threads of blue mussels (*Mytilus edulis*) for anchoring (Sharp et al., 2003). Thus, the primary mechanism of successful dispersion is suspected to be fragmented portions of fronds being recruited by mussel byssal threads (DFO, 2009).

The resiliency of GIM to future climate change is challenging to characterise, as various responses to environmental stressors have been reported in the literature. Juanes and McLachlan (1992a) found that the photosynthetic capacity of a PEI strain of *C. crispus* was limited by temperature from fall to spring and by nitrogen content throughout the summer. A lower temperature boundary of 14°C was suggested to define temperature-limiting conditions for photosynthesis (Juanes & McLachlan, 1992a), though *C. crispus* can easily survive sub-zero temperatures (Kylin, 1917). Lüning, Guiry, and Masuda (1986) demonstrated that reproductively mature thalli from *C. crispus* of Nova Scotia died after 2 weeks at 28°C in culture. Other regional strands or comparable species tested from Europe and Japan survived up to 29-30°C over this period (Lüning et al., 1986). *C. crispus* have been demonstrated to be photosynthetically optimised at an approximate salinity of 24 ppt and temperature of 20°C; however, some studies have shown *C. crispus* demonstrating a relatively uniform rate of respiration between 8-20°C (Mathieson & Burns, 1971). Bird, Chen, and McLachlan (1979) also suggested an optimal salinity between 10-40 ppt based on growth criteria that were considerably depressed outside of this range. The average salinity of sea water is approximately 35 ppt; therefore, it may be expected that *C. crispus* typically benefits from freshwater inputs from a salinity perspective. Maximum growth has been suggested around 15°C by Bird et al. (1979), approximately 5°C lower than the optimal temperature proposed for photosynthesis by Mathieson and Burns (1971). This variable behaviour may be explained by the complexity and interdependence of various factors controlling growth (Harley et al., 2012). For example, the ability of *C. crispus* to uptake nitrogen has been shown to be dependent on temperature (Juanes & McLachlan, 1992b). Alternatively, the characteristics of disjunct populations may diverge (Lüning et al., 1986; Novaczek & Breeman, 1990; Tasende & Fraga, 1992).

Tasende and Fraga (1992) tested optimal environmental parameters for carpospores and tetraspores of *C. crispus* in culture. The results of their study, in combination with their extensive literature review, highlighted the expansive range of optimal conditions reported in the literature for *C. crispus* (Tasende & Fraga, 1992). For example, their study reported optimal temperatures ranging from 11 to 19°C, optimal salinities ranging from 27 and 35 ppt, and optimal pH ranging from 7.5 and 8.3 across studies (Tasende & Fraga, 1992). This may corroborate a large variance in environmental tolerances between regionally disjunct populations (Lüning et al., 1986; Novaczek & Breeman, 1990; Tasende & Fraga, 1992). Prince and Kingsbury (1973) demonstrated that spore mortality increased with temperature from 17-26% at 11.7°C, to 84-94% at 23.9°C, and 100% by 26.7°C. They also demonstrated that spores were largely unaffected by a 30 second exposure to 35°C solution, but experienced 100% mortality when the 30 second treatment was increased to 45°C (Prince & Kingsbury, 1973). The GIM in BHH do not generate reproductive spores, but these studies highlight the potential variance within the species.

Previous acclimation also plays a role in the ability of *C. crispus* to respond to temperature stress (Eggert, 2012; Kübler, J & Davison, I, 1993). *C. crispus* grown at 20°C from Maine, USA, were able to maintain constant rates of photosynthesis at 30°C for 9h and recovered more rapidly than those grown at 5°C, which declined to 20-25% of initial photosynthetic productivity following exposure to 30°C (Kübler, J & Davison, I, 1993). Both samples were unable to grow beyond a temperature threshold of 25°C, and respiration increased dramatically in both the acclimated and non-acclimated samples after 6h at 30C. This study demonstrates that short exposures to high temperatures (30°C) are survivable by *C. crispus*, and that growth environment impacts the ability of the plant to cope with thermal stress (Kübler, J & Davison, I, 1993).

The inability of GIM to anchor itself to substrate emphasises a key vulnerability, in that their survival is contingent on the survival of blue mussels in the area. Blue mussels are typically found in clumps of twenty or less, often associated with Irish moss or GIM within the NE Arm of BHH (Sharp et al., 2003). As with plant species, the metabolism, behaviour, and survival of marine animals is also affected by temperature and other environmental factors. The growth of blue mussels has been demonstrated to decline rapidly after 20°C (Almada-Villela et al., 1982), with an upper mortality temperature threshold around 27-29°C (Read & Cumming, 1967; Seuront et al., 2019). Work by LeBlanc et al. (2005) recorded ~50% mortality in mussels exposed to 27°C air temperature and ~75% mortality from a 6-hour exposure to 33°C water. Seuront et al. (2019) demonstrated that blue mussels from the English Channel could sustain 1.5 to 3-hour exposures to 41°C without mortalities. However, with recurrent exposures mortality rate increased, demonstrating a decreased thermal tolerance with recurrent heat stress (Seuront et al., 2019). Ultimately, Seuront et al. (2019) demonstrated that survival rates of blue mussels are expected to decrease with increasing duration, intensity, and consecutive number of exposures. LeBlanc et al. (2010) have also provided evidence that size of mussels influences their thermal resistance, as smaller phenotypes experienced fewer mortalities than their larger counterparts.

Thermal stress may indirectly interfere with the process of blue mussels recruiting GIM fragments. For example, blue mussels are commonly prey to the invasive green crab (*Carcinus maenas*). This predation may be intensified during instances of thermal stress, as Dowd and Somero (2013) demonstrated that mussels tend to spend more time with their valves open after exposure to a temperature of 33°C. Their research suggested that there may be a temperature threshold between 25-33°C that initiates valve opening to avoid hypoxia (Dowd & Somero, 2013). Alternatively, byssal thread attachment was shown to be weakest in the summer and strongest in the winter in a study by Carrington (2002). This observation may be the result of temperature related reproductive activities throughout the summer that divert energy expenditures from byssal thread attachment (Carrington, 2002). Other environmental factors influenced by high temperatures may also cause unfavorable conditions for blue mussel growth.

These thermal studies represent a non-exhaustive overview of the thermal characteristics and susceptibility of *C. crispus*, and they reflect the large degree of uncertainty related to the thermal limits of *C. crispus*, which may be partly attributed to differences between various ecotypes. Although exact thermal thresholds are elusive for the BHH strain, temperatures beyond 30°C are likely detrimental to *C. crispus* metabolic activity and survival. Focussing almost exclusively on thermal stress in this review section drastically oversimplifies the complex and dynamic feedback that will occur between *C. crispus* and the environmental changes induced by climate change. It is important to consider climate and ecophysiological research in a dynamic multi-stressor framework to enhance our predictive capabilities (Harley et al., 2012), but this is beyond the scope of this largely hydrogeological study.

Section 2 – Geological History of Kingsboro, PEI

This section provides supplemental information on PEI geological stratigraphy and geomorphology to supplement Chapter 2, Section 2.2.1 in the main body of the report.

Historical drill logs across PEI suggest three major soil intervals commonly assigned to the Pictou Group of Atlantic Canada (van de Poll, 1989). Van de Poll (1989) proposed that the characteristic red strata of PEI be assigned to the Prince Edward Island Group, which would be classified alongside the Pictou Group as part of the overarching Northumberland Strait Supergroup. These layers were further subdivided into megacycles (J. I. MacDougall et al., 1988; van de Poll, 1989).

The strata located under the Kingsboro watershed (KW) have been assigned to the Wood Island Member of the Hillsborough River Formation, or Megacyclic Sequence III (J. I. MacDougall et al., 1988; van de Poll, 1989). The conglomerates of this group are described as compositionally less mature and less rounded than any other PEI conglomerates (van de Poll, 1989). There is consensus that these soil layers date back to the early Permian Period, approximately 225-300 million years ago (Prest, 1973a; van de Poll, 1989). Trace amounts of hematite colour most strata red (Crowl, 1969a). It has been deduced that the preserved red colouration of exposed PEI layers is indicative of low original organic content during their formation, which differentiates PEI strata from the older grey beds of New Brunswick and Nova Scotia (Prest, 1973a; van de Poll, 1989). Sandstones native to PEI are composed of angular to subangular grains of quartz and feldspar, as well as lesser amounts of mica, chlorite, magnetite, and ferruginous cementitious material (Brandon, 1966). A high degree of crossbedding has been observed in the layers, indicative of a deltaic or low alluvial plain depositional history (Crowl, 1969a).

Outcropping is most frequently observed on the coastlines (Brandon, 1966) and are useful sources of geological information. In general, the strata beneath the KW have been interpreted as flat to gently sloping (Brandon, 1966; Crowl, 1969a; van de Poll, 1989). In the northeast of PEI, Van de Poll (1989) observed dips up to 7°, and Crowl (1969b, 1969a) proposed a strike of N60°W and a dip between 1-2°N based on regional structural trends and geomorphological surveys. Similarly, Brandon (1966) observed dips of <5% (i.e., <3°), although the localities assessed where not stated.

The primary surficial soil in the KW is clay-sand (Crowl, 1969c) to sand phase till (Prest, 1973b). The soil is primarily derived from ground moraine; however, a small area of glaciofluvial deposition is found at the mouth of the primary freshwater stream to the northwest of BHH. Unconsolidated glacial overburden on the eastern side of PEI is entirely derived from local sandstone and mudstone, so it preserves a reddish colour (Brandon, 1966; Crowl, 1969a; Francis, 1989). As such, weathering of mudstone and sandstone has created soils difficult to distinguish from deposited till, as they share the same source material (Prest, 1973a). Francis (1989) concluded from their study that clay content appeared to be overestimated in the earlier regional soil survey by Crowl and Frankel (1970). Clay content has a great influence on the hydraulic properties of a soil, so it may be important to consider that soil classifications in Crowl (1969c) may overestimate clay content at the study site if the error was systematic. This approach would favour the sand phase till interpretation of Prest (1973b). Alternatively, the observed differences of Francis (1989) may simply exemplify the limitations of the discrete sampling of a highly variable natural system.

A saltwater marshland and series of dunes, assigned to the Wood Island soil series, form part of the harbour watershed (PEI Dept. Env., 2002). Prest (1973a) considered the dune and lagoon features of BHH as the best representation of PEI beach ridges. Glacial sands deposited by the eastern island ice cap were carried westward by tidal currents to what is now the Basin Head Provincial Park (Prest, 1973a). These deposits evolved to form sand ridges, dunes, and ultimately a lagoon feature (Prest, 1973a). Kjerfve and Magill (1989) define lagoons as poorly flushed coastal landforms with limited connection to the ocean that are ephemeral on a geologic time scale. It is highly likely that the main entrance to the lagoon would close over due to natural processes if not for dredging activities and installed infrastructure. Over the past two hundred years, the geomorphology of the lagoon has changed significantly as a result of natural processes and anthropogenic interventions (Figure 2; Sharp et al., 2003). This shoreline continues to change as a result of coastal erosion, wind, and anthropogenic influences (Prest, 1973a). The resulting changes to the system's hydrodynamics have undoubtedly impacted GIM within the lagoon over time.

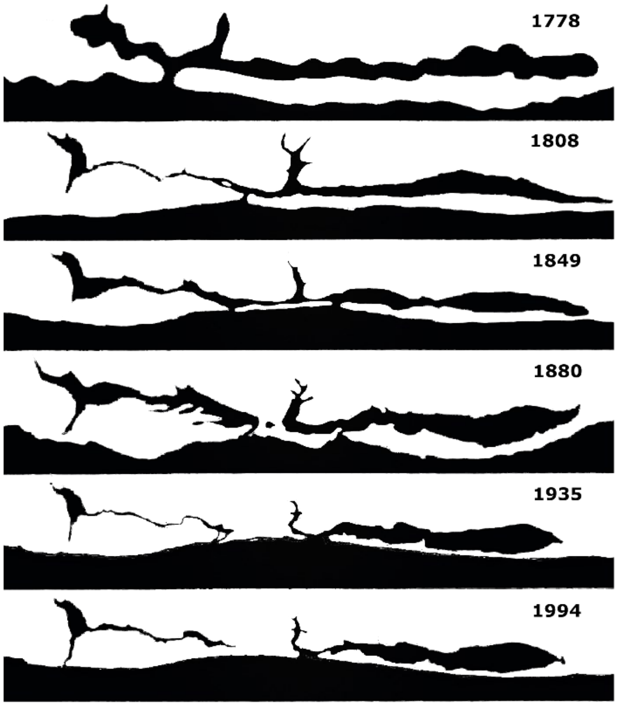

Figure 41. Historical geomorphology of the Basin Head Harbour with respect to the ocean (bottom of each panel). The constructed western entrance to the harbour was developed in 1937, paired with the damming of the upper northeast arm. This figure is adapted from a figure presented in Sharp et al. (2003), which compiled historical maps, surveys, and areal photos from the National Air Photo Library. Black = water; white = landmass.

Section 3 – Thermal Plume Areal Analysis Methodological Study

Several experiments were conducted to appraise possible sampling and analysis procedures for the thermal plume areal analysis of this study. Proposed methods are based on procedures developed for graphical information system software by Danielescu et al. (2009) and for handheld cameras by Roseen (2002). The software utilised in this method included FLIR Tools®, ImageJ, MATLAB®, and M-B Ruler (Bader, 2020). FLIR Tools® and ImageJ are image analysis software products and M-B Ruler is a digital measurement application. The reader is encouraged to review the contents of Section 2.6 before proceeding into this section.

A thermal image of an intertidal spring captured in BHH was used as the focus of this study (Figure 42). Unlike the hypothetical type-curve proposed in Section 2.6 (Figure 10), this image was selected because it demonstrates non-ideal conditions (i.e., the spring discharge travels several metres over land prior to entering the lagoon, the thermal signature of the vegetation is comparable to the plume area, the warm sand in the image forms a third distinct thermal group, and vignetting in the corners of the image is apparent).

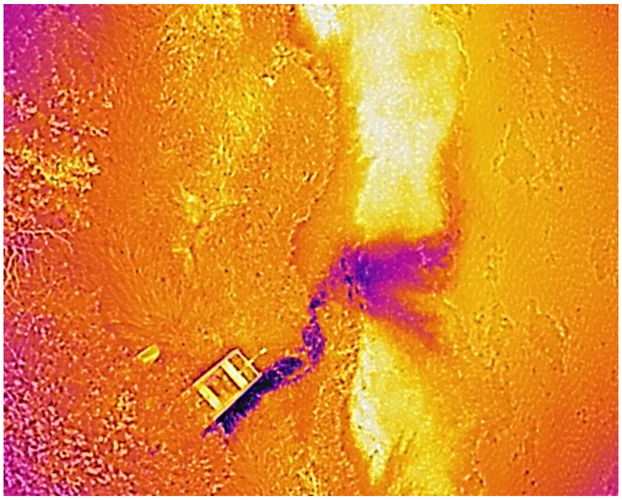

Figure 42. Raw thermal image of spring discharge in Basin Head Harbour used for methodological study (image captured 2019-08-16 at 17:00 LST during generally clear sunny conditions).

This image was selected with the intent of improving this technique for this study and disambiguating the uncertainties of the areal analysis. Within the constraints of the software available for this project, ten methods were initially assessed in Experiment 1 (listed in Table 23).

Table 23. Properties of the ten different thermal image processing methods considered for the thermal plume areal analysis of this study. The table includes the ID assigned to the method, the software package(s) involved in the method, the data output format, if the image was rectangularly cropped, the colour scale applied to the image, and whether a FLIR logo and scale bar were present during data analysis. GsI = grayscale intensity; T = temperature; S = signal.

ID	Analysis Software	Output Format	Cropped	Colour Scale	Logo and Scale Bar
T1	FLIR Tools®	T	No	NA	NA
T2	FLIR Tools®, Excel	T	Yes	NA	NA
GsI-1	FLIR Tools®, ImageJ	GsI	No	T Linear	Yes
GiS-2	FLIR Tools®, ImageJ	GsI	Yes	T Linear	No
GiS-3	FLIR Tools®, ImageJ	GsI	No	S Linear	Yes
GiS-4	FLIR Tools®, ImageJ	GsI	Yes	S Linear	No
GiS-5	ImageJ	GsI	No	Contrast Optimised	No
GiS-6	ImageJ	GsI	Yes	Contrast Optimised	No
GiS-7	FLIR Tools®, ImageJ	GsI	No	Histogram Equalisation	Yes
GiS-8	FLIR Tools®, ImageJ	GsI	Yes	Histogram Equalisation	No

Subsequent tests explored the merits of polygonal cropping (Experiment 2) and graph scale (Experiment 3). It is believed that the most effective method was identified (i.e., GsI-2 with polygonal cropping), and an overview of the different data challenges and considerations one might encounter during the application of this method was constructed. The many challenges discussed throughout Experiments 1, 2, and 3 are manageable with cautious analysis of the visual and graphical thermal data.

Section 3.1 – Plume Analysis Experiment 1: Methodological Investigations

The ten options for areal analysis summarised in Table 23 are graphed in Figure 43 and Figure 44, grouped by their data unit (i.e., binned temperature or grayscale intensity). A spatial resolution of 10 cm^2/pixel was assumed for the thermal image in each of the ten iterations.

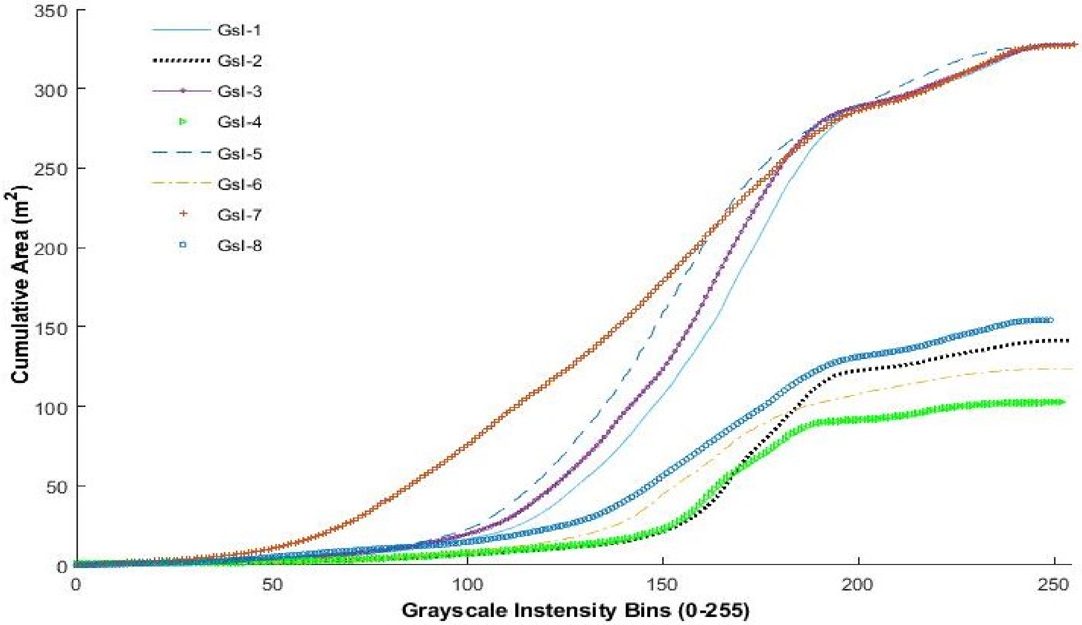

Figure 43. Grayscale intensity type-curves for eight different thermal-discharge areal analysis methods. Each type-curve describes the same thermal image data, post-processed differently. The details of each iteration are summarised in Table 23.

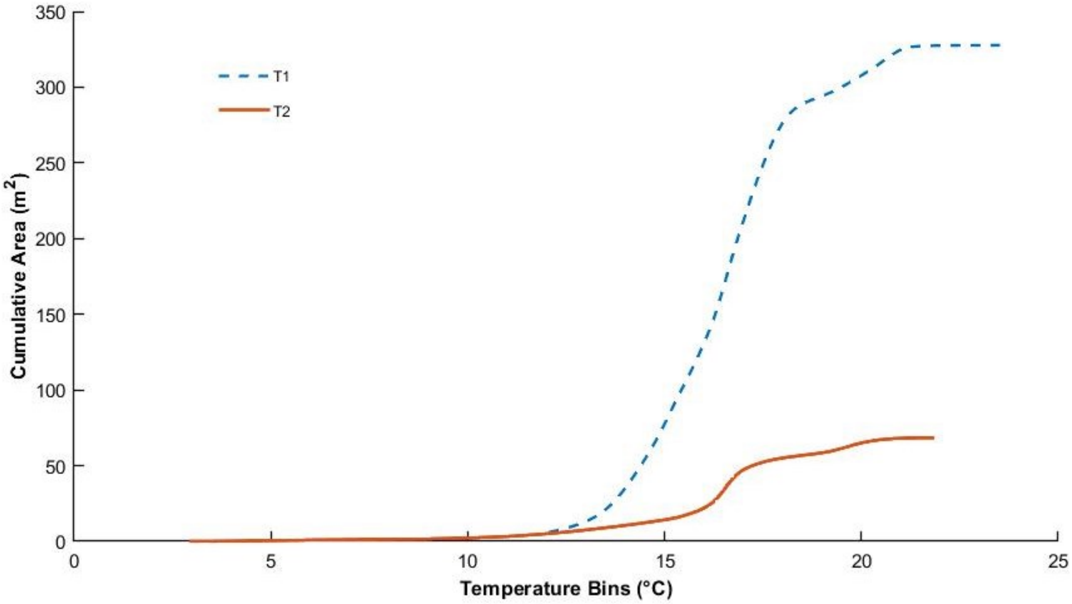

Figure 44. Relative temperature type-curves for two different thermal-discharge areal analysis methods. Each type-curve describes the same thermal image data, post-processed differently. The details of each iteration are summarised in Table 23.

The graphical method of Roseen (2002) was applied to identify the plume area. The x-axis values of the inflection points were recorded to compare the various distributions (Table 24). The area associated with the second inflection point was also recorded to assess curve geometry (Table 24).

Table 24. Type-curve properties for Experiment 1 of the methodological study. Plume area and second inflection point area are rounded to the nearest squared metre. Binned temperature values are rounded to the nearest 0.5°C, whereas grayscale intensity is rounded to the nearest whole multiple of 5. All configurations utilise an assumed spatial resolution of 10 cm^2/pixel and were analyzed using a combination of FLIR Tools®, ImageJ, MATLAB®, and M-B Ruler. GsI = grayscale intensity.

ID	Plume Area (m^2)	Second Inflection Point Area (m^2)	First Inflection Point (°C^a or GsI)	Second Inflection Point (°C^a or GsI)
T1	20	278	13.5[a]	18[a]
T2	15	48	15.5[a]	17[a]
GsI-1	29	273	115	190
GsI-2	23	117.5	150	190
GsI 3	26	275	110	190
GsI-4	20	87.5	145	185
GsI-5	26	260	100	180
GsI-6	20	95	130	180
GsI-7	19	276	60	190
GsI-8	26	126	125	190

[a] *Values are temperature [°C], whereas unflagged values in the column are expressed in grayscale intensity.*

Notable divergence from an ideal type-curve is observable, and the occurrence of at least three distinct thermal groups are apparent in most of the type-curves (Figure 43 and Figure 44). These thermal groups represent the cold-water thermal plume, the lagoon water, and the warm sandy beach. The sandy beach and plume occupy distinct thermal temperature ranges relative to the remainder of the image; however, it is clear through manual inspection of the image data that vegetation temperatures and vignetting in the corners of the image overlap the temperature group of the lagoon water as well as the sharp transition zone. This interference may be diagnosed by manual inspection of the thermal image data in conjunction with the occurrence of two distinct slopes within the transition zone observed in most of the type-curves. Thus, the cumulative area marked by the second inflection point and the slope of the transition zone is affected by interference, likely modifying the estimate of the plume area thermal group.

Additional interference was incurred by the scale bar and logo, which were unavoidable with the use of FLIR Tools®. The interference of the FLIR overlay and the effect of vignetting may be effectively mitigated by rectangular cropping, so long as the plume is centered in the image; however, the vegetation interference persists because of the in-land discharge location. This remaining interference did not overlap the plume area thermal group directly, as there is adequate contrast between the cold-water discharge and the remainder of the image, but it does impact the estimate of its extent by modifying the slope of the transition zone that is used in the identification of the first inflection point. The logo and scale bar cannot be included in the analysis while using grayscale values, as they inflate graphical thermal groups and smooth the type-curve by reducing the significance of their relative differences.

By inspecting the variability in the area of the second inflection point relative to the variability of the plume areas (Table 24), it is apparent that the magnitude of the second inflection point is more susceptible to the interference within the transition zone relative to the first. This is also the case with rectangular cropping, despite a large proportion of the interference being removed through this process. In response to the sustained interference with rectangular cropping, a more rigorous cropping procedure is required that enhances the accuracy and reproducibility of the type-curve analysis. As a result, a polygonal cropping technique was assessed in Experiment 2.

The chosen colour scale does seem to have a minor effect on manual cropping, but it is minor relative to the geometric changes the colour scale itself produces in the type-curve (e.g., GsI-2 compared to GsI-4). Cropping based on the visual extent of the plume area does inevitably increase practitioner bias and mild variability in cropping. In general, cropping should be conducted consistently by an informed practitioner to minimise interference with the thermal groups of interest, whilst including the entire extent of the plume area and as much of the discharge environment as practicable. As discussed earlier, vignetting and proprietary overlays should be removed where possible. Care should be taken to mitigate interference during image capture and the data should be rigorously preprocessed to ensure that the method of Roseen (2002) is tenable.

In many cases, spring discharge may travel a considerable distance before entering the receiving body of water. This overland travel likely impacts the thermal signature of the water by the time it reaches the receiving body, affecting the empirical relationship by reducing the extent of the thermal plume upon entry into receiving waters. As a result, it is proposed that the plume area should include this travel distance to compensate for this heat transfer. Likewise, it is considered that there needs to be a working definition for “near-shore spring” that discriminates groundwater discharges by distance (e.g., no more than five metres from the high tide mark). Otherwise, streams in PEI, which are sourced predominantly to entirely by groundwater during the summer, may arguably also be included in the definition based on thermal properties and groundwater origin alone.

Despite thermal interference and differences between the colour scales and cropping, the range of estimates for the plume area is well constrained between 15-29 m^2. This instills reasonable confidence that slightly different methods may still yield reasonably comparable estimates of plume area with adequate thermal contrast. However, it is not tenable to compare the second inflection point area in the same manner due to widespread interference in the first study.

Both temperature and temperature linear GsI may easily be field calibrated using temperature sensors as required, which is a notable advantage over the other eight methods examined. As cropping has been proven to be essential, this narrowed the selection to methods T2 and GsI-2. Ultimately, GsI-2 was selected because T2 overemphasised the uncalibrated and unreliable temperature measurements of the thermal images.

Section 3.2 – Plume Analysis Experiment 2: Polygonal Cropping

Originally, a rectangular cropping procedure was anticipated to be adequate, based on binning strategies demonstrated to be effective by Danielescu et al. (2009) and Roseen (2002). However, Experiment 1 demonstrated that polygonal cropping would enhance the accuracy and reproducibility of plume areal assessments, which is practicable in ImageJ (Figure 45). Linear temperature grayscale (GsI-2) was polygonally cropped and compared to signal linear grayscale (GsI-4) to demonstrate the practicability of the new analysis method and to further investigate the role of practitioner bias. There are only minor differences between the two temperature scales, so the results of their respective analyses should be comparable.

Type-curves were developed for both cropped images (Figure 45) and are presented in Figure 46. The curves are comparatively ideal to those displayed in Experiment 1, as might be expected with very minor thermal interference, and the two thermal groups were easily defined. The manual type-curve areal analysis for TL (i.e., GsI-2 with polygonal cropping) is displayed for reference in Figure 46, and the same analysis was carried out on SL (i.e., GsI-4 with polygonal cropping).

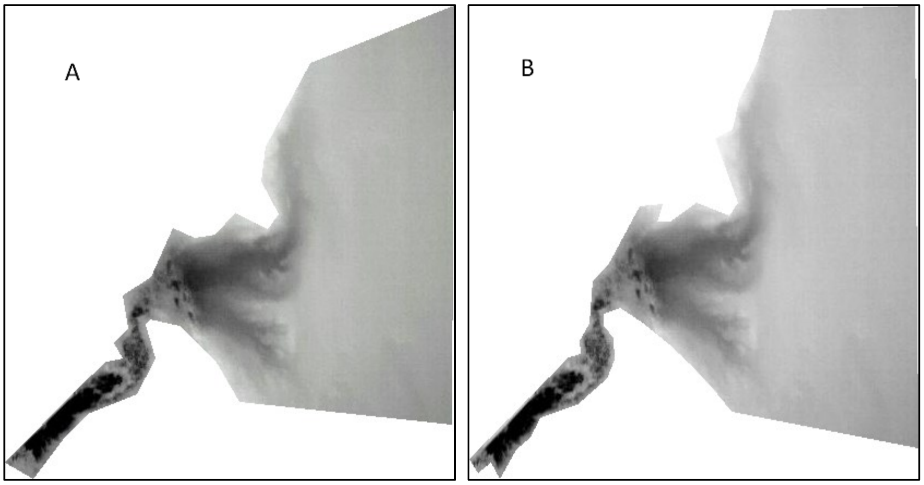

Figure 45. Polygonal cropping of GsI-4 (A) and GsI-2 (B) conducted in ImageJ software. Note minor differences in cropping result (sampling bias) and minor differences in grayscale intensities. The plume area estimated by the two approaches are within 5 m^2 of each other (Table 25), given an assumed spatial resolution of 10 cm^2/pixel.

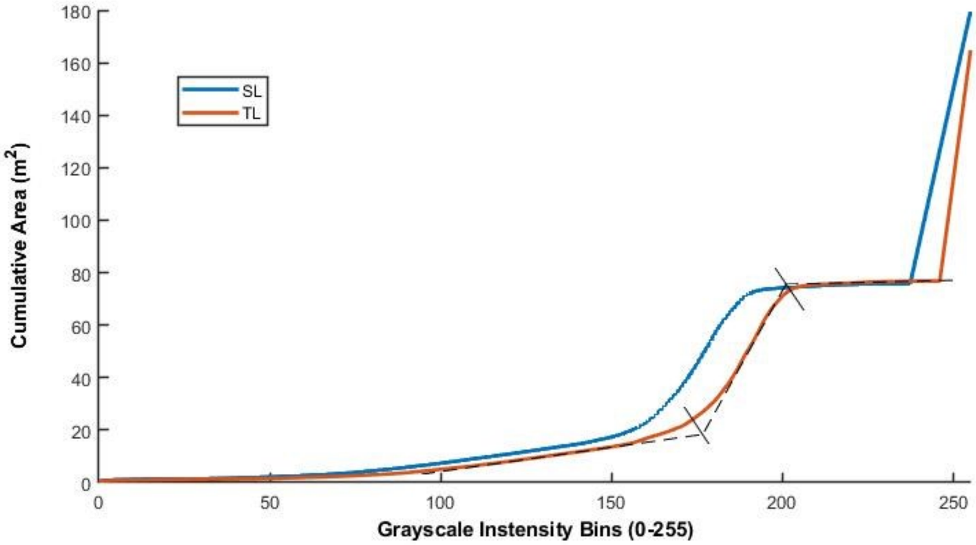

Figure 46. Type-curves for Experiment 2 of the methodological study. Manual graphical analysis of the TL curve is portrayed for reference and methodological clarity (dashed lines and perpendicular markers). Cropped-out area was converted to white in ImageJ, generating linear artifacts near the curve terminals. SL= signal linear grayscale; TL = temperature linear grayscale.

Calculated type-curve parameters for SL and TL were compiled in Table 25 with GsI-2 and GsI-4 for comparison. The estimates of plume area remain well constrained across all methods. Unlike the rectangularly cropped methods (i.e., GsI-2 and GsI-4), the consistency of the second inflection point area is also well constrained for SL and TL, evidencing a reduction in thermal interference. Differences between SL and TL are attributed to practitioner bias, resulting in different amounts of thermal interference, as well as the minor differences between the colour scales. Although Experiment 2 demonstrates that interference may be effectively mitigated, minor amounts of interference and user bias are likely unavoidable.

Table 25. Type-curve properties for Experiment 2 of the methodological study. This test demonstrates the effect of polygonal cropping relative to rectangular cropping. All configurations are in units of grayscale intensity, utilise an assumed spatial resolution of 10 cm^2/pixel, and were analyzed using a combination of FLIR Tools®, ImageJ, MATLAB®, and M-B Ruler. Plume area and the second inflection point area are rounded to the nearest squared metre. Binned temperature values are rounded to the nearest 0.5℃, whereas grayscale intensity is rounded to the nearest whole multiple of 5. GsI = grayscale intensity.

ID	Cropping	Colour Scale	Plume Area (m^2)	Second Inflection Point Area (m^2)	First Inflection Point (GsI)	Second Inflection Point (GsI)
TL	Polygonal	T Linear	24	73	175	200
GsI-2	Rectangular	T Linear	23	117.5	150	190
SL	Polygonal	S Linear	22	71	160	195
GsI-4	Rectangular	S Linear	20	87.5	145	185

It became apparent in Experiment 2 that there may be two linear segments in the plume thermal group. There is a near-uniform temperature signal at the immediate discharge location, with relatively rapid diversification of temperature readings as water is transported away from its origin towards the lagoon. In this circumstance, the latest stable linear portion should be used for inflection point identification. It is likely that this type-curve behavior was present in Experiment 1, but it was not apparent because of y-axis scale and thermal interference. Thus, it may be important to enhance the axes scales to improve areal analysis procedures by revealing critical details of the type-curve. This notion was quickly examined in Experiment 3.

Section 3.3 – Plume Analysis Experiment 3: Graph Scale

Given the manual method of type-curve analysis, the scale of the graph axes may impact the parameter estimates. To examine this, the axes were trimmed to exclude the cropped-out portion of the thermal image (Table 26 and Figure 47) and the type-curves were reassessed.

Table 26. Type-curve properties for Experiment 3 of the methodological study. This test demonstrates the effect of graph scaling. All configurations are in units of grayscale intensity, utilise an assumed spatial resolution of 10 cm^2/pixel, were polygonally cropped, and were analyzed using a combination of FLIR Tools®, ImageJ, MATLAB®, and M-B Ruler. Plume area and the second inflection point area are rounded to the nearest squared metre. Binned temperature values are rounded to the nearest 0.5°C, whereas grayscale intensity is rounded to the nearest whole multiple of 5. GsI = grayscale intensity.

ID	Colour Scale	x-Axis Maximum	y-Axis Maximum	Plume Area (m^2)	Area of Second Inflection Point (m^2)	First Inflection Point (GsI)	Second Inflection Point (GsI)
TL	T Linear	255	180	24	73	175	200
TL’	T Linear	225	80	21	74	170	205
SL	S Linear	255	180	22	71	160	195
SL’	S Linear	225	80	21	72	160	190

Non-idealities in the type-curve (e.g., the multiple linear segments in the plume area thermal group of TL’ in this case; Figure 47), become more apparent when the axis scales are focussed on the region of interest. These non-idealities are likely caused by thermal interference, colour scaling, cropping practices, and complex thermal mixing and transport. This highlights that the linear fitting of the plume thermal group may be affected by the scale of axes, which affects the calculation of curve parameters (Table 26). The TL’ plume area estimate is sufficiently different to make the consideration of axis scale a recommended best practice. Further, curve smoothing is not recommended, as it may conceal indicators of thermal interference and reduce the ability of the practitioner to critically evaluate the data. Non-idealities create additional opportunities for practitioner bias to be introduced into fitting linear segments of the type-curve, so axis scaling and robust data pre-processing should be guided by sound professional judgement to enhance the analysis process. Inspecting image pixel values in tandem with graphical assessment should be considered essential to the process.

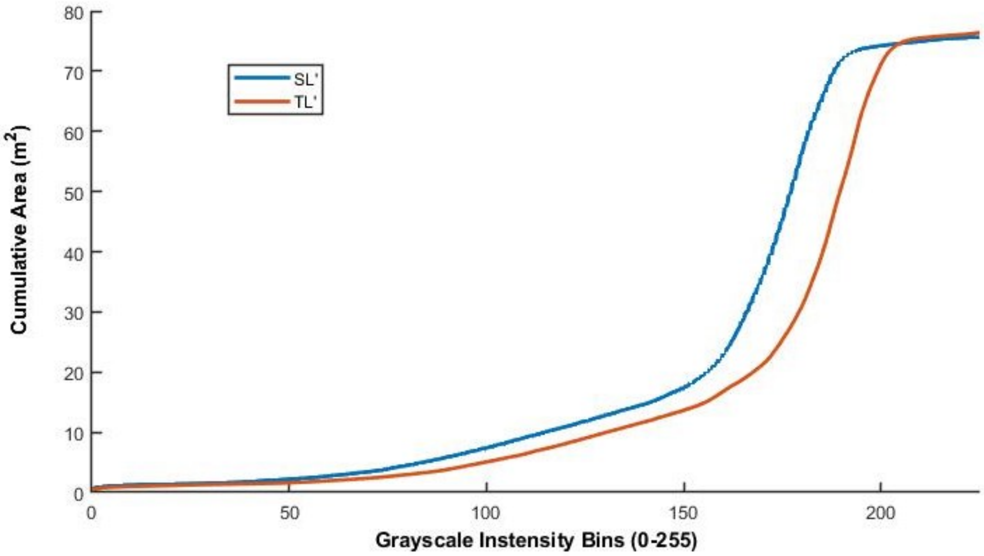

Figure 47. Type-curves for Experiment 3 of the methodological study, wherein the scale of the axes is more targeted to highlight risks for sampling bias. SL'= signal linear grayscale with modified axes; TL' = temperature linear grayscale with modified axes.

The second inflection point area and the calculated inflection points are minorly affected in this example; however, it is conceivable that non-idealities could exist within the transition zone and lagoon thermal group of a type-curve instead. In the case where the plume area portion of the graph has two or more distinct linear behaviors, commonly the result of discharge and mixing dynamics, fitting the segment before the transition zone is recommended.

Section 4 – Supplemental Interpretations of Spring Data

This section provides supplemental interpretations of the spring temperature data analysed in Chapter 3, Section 3.5 in the main body of the report.

Figure 27 demonstrates that lagoon water temperatures in the shallow upper NE Arm were dominated by a mixed diurnal signal in 2019 (Chapter 3, Section 3.5), which means that their thermal signal is predominantly dependent on solar radiation but is also impacted by the tide. This behaviour was reproduced in 2020 as well. In contrast to the lagoon water, the temperature at the outlet of the nearby Spring 5 is mainly tide dominated (Figure 27), likely because the discharge rate is impacted by tidal stage and hydraulic gradient, or rather the local mixing proportions and dynamics change. One benefit of this understanding is that this single inexpensive temperature sensor supplies temporal, directional, and relative magnitude information about tidal stage. For example, valleys on the black series in Figure 27 indicate low tides, whereas the peaks indicate high tide. It follows that the transitions between peaks indicate the ebb and flow tides. Furthermore, the occurrence of storm surge was often apparent in that it disrupted the typical thermal patterns of springs. These interpretations are possible because the sensor is in the intertidal zone and the spring temperature is relatively stable with respect to the lagoon. Combining the interpretation of intertidal temperature data with traditional pressure sensors may be an inexpensive way to enhance spatial coverage of tidal dynamics. Take BHH for instance, where the long NE Arm channel lags the propagation of the tidal signal experienced at the entrance of the lagoon. The upper NE Arm intertidal temperature sensor supplies localised timing information about tidal flooding and recession at relatively little additional cost.

Incidentally, Figure 27 also depicts a notable dampening of the diel temperature signal from the surface of the lagoon to the bottom of the lagoon channel over as little as one metre of depth. Thus, lagoon temperatures at the channel bottom are usually lower during the day and higher at night relative to surface temperatures. Although lagoon water is consistently warmer than springs over the focussed study period, spring measurements in Figure 28 suggest that groundwater temperatures converge with lagoon water temperatures around the end of October. Thus, this would be one of the worst times for capturing high thermal contrasts using TIR imaging.

APPENDIX C: HYDRAULIC TEST DATA & METHODS

Section 1 – Pumping Test Data & Models

Pumping tests refer to time-drawdown assessments conducted using groundwater wells to estimate the hydraulic properties of an aquifer or the well itself. Where possible, long-duration (i.e., ≥24-hour) multi-well tests are preferred over single-well or short-duration tests, as they have a larger area of influence and are thus conceived to represent the aquifer's properties and non-idealities more accurately. Furthermore, single-well tests may be affected by well efficiency and storage (Halford & Kuniansky, 2002). Conducting a full scale multi-well pumping test is outside of the scope and resources allocated to this project. Fortunately, a time-drawdown assessment involving one pumping well and three observation wells was conducted by Joostema (2015) in Souris, PEI, that was analyzed to provide an estimate of the bedrock hydraulic conductivity for the KW. The well casing terminates at approximately 18 metres depth, and an open "well screen" extends down to 94 metres depth. Although several discrete water bearing zones are intersected that contribute most of the water, the aquifer was regarded as a single homogeneous hydrogeological unit from which bulk properties could be inferred.

Little interpretable variation in water level was observed in the two most distant wells used in the study, so only the closest well was analyzed. Further, unknown factors appear to complicate the drawdown behaviour of the test shortly after two hours. Despite being conducted for 24 hours, only this initial selection of data was usable for modelling analysis (Table 27).

It is possible that a recharge event occurred which interfered with the aquifer response; however, precipitation data is not available for the site at the time of the study. In addition, higher pumping rates (i.e., 910, 810 and 815 igpm) were used for the first 10 minutes of the test, before subsequently being held constant at 750 igpm (Joostema, 2015). To exclude those data entirely would result in the loss of important regions of the response curve. This is considered during model interpretation and by adopting an adjusted "constant" pumping rate of 780 igpm for the 137 minutes test (Table 27), as the selected models assume a constant pumping rate.

Table 27. Reported and assumed pumping rates for a time-drawdown test in Souris, Prince Edward Island, as well as the associated drawdown data in a response well 96 metres away from the pumping well. This test was performed by Joostema (2015).

Time (min)	Reported Pumping Rates (igpm)	Assumed Pumping Rate (igpm)	Drawdown (m)
0.1		780	0
1		780	0.04
2		780	0.08
3		780	0.13
4		780	0.16
5	910	780	0.18
6		780	0.19
7	810	780	0.2
8		780	0.21
9	815	780	0.22
10		780	0.23
12	750	780	0.24
15	750	780	0.26
20	750	780	0.27
25	750	780	0.29
30	750	780	0.31
35	750	780	0.32
40	750	780	0.31
50	750	780	0.31
60	750	780	0.32
75	750	780	0.35
92	750	780	0.39
107	750	780	0.41
122	750	780	0.43
137	750	780	0.45

For the purpose of this study, the Theis (1935) and Warren and Root (1963) models were considered most applicable to evaluate the Souris time-drawdown data. Both are applied in this study because either may be regarded as a justifiable model for analysis of the pumping test response, and uncertainty remains as to which is most appropriate. Regardless, with such a complex natural system, these models are limited in their conceptual explication of what is truly anticipated in the subsurface. The models were fitted using the free MATLAB® supplemental software package Hytool (Version 2.06; Renard, 2017). Hytool is a toolbox that facilitates the interpretation of hydraulic well test data by means of fitting and assessing analytical models of groundwater flow surrounding wells (Renard, 2017).The assumptions on which these models are based are summarised in the following sections.

Section 1.1 – Theis Model (1935)

The Theis (1935) model is a transient analytical solution for a well in an idealised confined aquifer. It relies on several assumptions (Halford & Kuniansky, 2002):

1) the aquifer is fully confined, horizontal, homogenous, isotropic, and has an infinite horizontal extent of uniform thickness;
2) the pumping rate is constant, and discharge is sourced exclusively from aquifer storage;
3) the well radius is small and 100% efficient;
4) the well is fully penetrating; and
5) the potentiometric surface is initially horizontal.

Under these conditions, the equation to calculate drawdown is (Halford & Kuniansky, 2002):

$$s = \frac{Q_{pump}}{4\pi T_{bulk}} W(u) \tag{16}$$

where

$$W(u) = -0.577216 - \ln(u) + u - \frac{u^2}{2 \bullet 2!} + \frac{u^3}{3 \bullet 3!} - \frac{u^4}{4 \bullet 4!} + \cdots, \tag{17}$$

$$u = \frac{{R_{rad}}^2 S_{aq}}{4 T_{bulk} t} \tag{18}$$

and

s is the drawdown (m)

T_{bulk} is the bulk transmissivity of the aquifer (m^2/s)

Q_{pump} is the pumping rate from the well (m^3/s)

S_{aq} is the aquifer storativity ($m^3/m^2/m$)

R_{rad} is radial distance from pumping well (m)

Characteristics shapes of the Theis curve aquifer response are displayed in Figure 48.

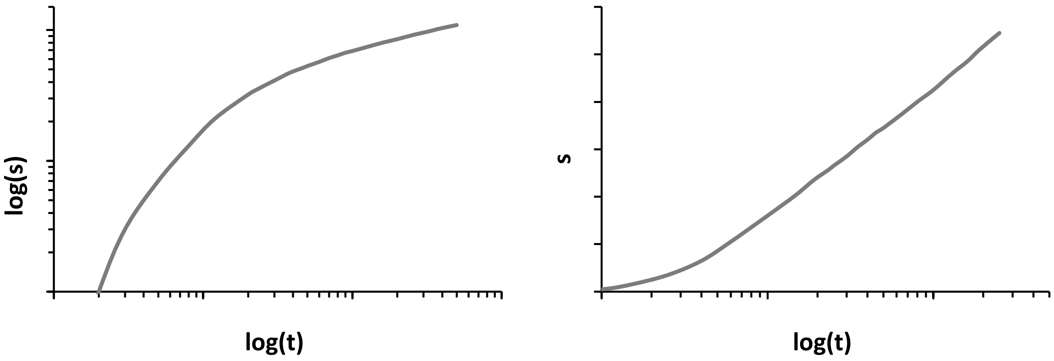

Figure 48. Generic Theis semi-log and log-log plot for confined aquifer response. Data modified from Fetter (2001) to more closely match diagrams from Kruseman and de Ridder (2000). s = drawdown; t = time.

Section 1.2 – Warren & Root (1963)

The Warren and Root (1963) analytical model can be applied to a pumping well (single-well test) or a response well (multi-well test) to analyse dual-porosity fractured media. The multi-well test is preferred, as it avoids the consideration of well losses and storage effects within a pumping well (Kruseman & de Ridder, 2000). The Warren and Root (1963) model assumes an idealised three dimensional and orthogonal fracture system (Kruseman & de Ridder, 2000), and it is less sophisticated than its successors (e.g., Bourdet & Gringarten, 1980; Kazemi, Seth, & Thomas, 1969). Additional assumptions include (Kruseman & de Ridder, 2000):

1) the aquifer is confined, has infinite horizontal extent, and is of uniform thickness over the area of influence;
2) the aquifer consists of two overlapping continuous systems (media and fractures);
3) the exchange rate between the fractures and the media is assumed to be in pseudo-steady state;
4) the transmission of water to the well occurs through the fractures only;
5) the well fully penetrates a fracture;
6) the pumping rate from the well is constant;
7) the piezometric surface is initially horizontal;
8) the flow is in an unsteady state;
9) the well radius is small and 100% efficient; and
10) generally, $\frac{t_D}{r_D^2} > 10$ for the early testing period, and $\omega < 10^{-2}$ for the intermediate testing period (variables as defined below in Equation 20).

Under these conditions, the following equation may be used to estimate the aquifer response observed in a response well (Warren & Root, 1963):

$$s = \frac{Q}{4\pi T_f}[\ln\left(\frac{4t_D}{(1+\varepsilon)r_D^2}\right) - 0.577215 - E_1\left(\frac{\omega(1+\varepsilon)t_D}{\varepsilon r_D^2}\right) + E_1\left(\frac{\omega t_D}{\varepsilon}\right)] \qquad (19)$$

where

$$t_D = \frac{T_f t}{r^2 S_f}, \qquad r_D = \frac{R_{rad}}{r}, \qquad \omega = \frac{\alpha r^2 T_m}{T_f}, \qquad \varepsilon = S_m/S_f \qquad (20)$$

and	T_f	is the transmissivity of the fracture (m^2/s)
	T_m	is the transmissivity of the matrix (m^2/s)
	S_f	is the storativity of the fracture ($m^3/m^2/m$)
	S_m	is the storativity of the matrix ($m^3/m^2/m$)
	α	is the medium compressibility (Pa^{-1})
	r	is the well radius (m)
	E_1	is the exponential integral function

The Warren and Root (1963) model depicts two parallel lines connected by a transitional period on a semi-log plot of drawdown versus time – characteristic of a confined fractured aquifer (Figure 49). This behaviour may also be expected from a unconfined aquifer with delayed yield (Kruseman & de Ridder, 2000).

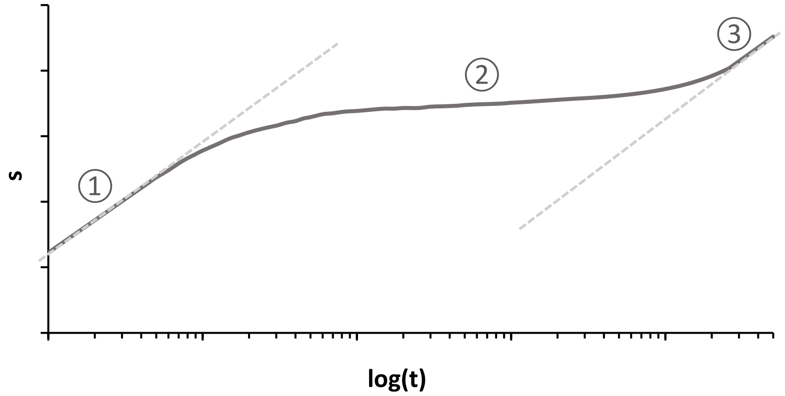

Figure 49. Generic semi-log drawdown curve for a dual-porosity or unconfined (with delayed yield) aquifer system. (1) Initial response period; (2) transitional period; (3) secondary response period.

Section 2 – Specific Capacity Analysis Methods

As a result of the costs and expertise required to conduct aquifer tests, they are infrequently conducted on private wells (Mace, 2001; Maliva, 2016). More commonly, well drillers conduct a specific capacity test, which may also be used to estimate important hydraulic properties of the aquifer, enhancing our spatial understanding of the subsurface (Mace, 2001; Maliva, 2016). Specific capacity (S_c) is equal to:

$$S_c = \frac{Q_{pump}}{s_w} \tag{21}$$

where Sc is the specific capacity (m^2/s)
s_w is the change of hydraulic head within the well (m)

Unfortunately, only 1 of the 24 wells on record in the KW included a specific capacity test (Government of PEI, 2019). This test was analyzed to diversify the methodologies used to infer the bulk properties of the subsurface within the KW. Based on the well log, the well casing descends below the surficial till, so the well screen section likely begins in the highly fractured zone of the bedrock and continues down to approximately 70 metres (Government of PEI, 2019). The test was performed at a constant pumping rate of 30 igpm over a 24-hour period. The bulk bedrock aquifer thickness was estimated as 33 metres. Hydraulic conductivity may be computed by the ratio of transmissivity to aquifer thickness:

$$Hydraulic\ Conductivity = \frac{Transmissivity}{Aquifer\ Thickness} \tag{22}$$

The first half of this aquifer may be expected to be highly fractured, so higher hydraulic conductivity estimates may be expected compared with those derived from the pumping test of Joostema (2015).

Despite being far less reliable than a multi-well pumping test analysis, as well as the numerous available literature values, this specific capacity value was analysed using two different methods proposed in Mace (2001). The results of these efforts should be regarded with scrutiny as the data, the proposed methods, the conceptual understanding of the aquifer system, and the knowledge of the well construction were all limited. Ideally, corrections can be made for well penetration, well losses, and aquifer properties when a robust dataset is available (Mace, 2001).

Section 2.1 – Thomasson Jr. et al. (1960) Semi-Analytical Method

The first selected method is based on the Dupuit-Thiem equation, and it assumes that drawdown has stabilised under the pumping perturbation, the well is partially penetrating, and that there are no well losses (Mace, 2001; Thomasson Jr. et al., 1960). In addition, this solution was developed for continuous porous media flow, which may not be a ubiquitous quality of PEI aquifers. Thomasson Jr. et al. (1960) used the Dupuit-Thiem equation to demonstrate that transmissivity (T_{bulk}) is linearly related to specific capacity by a constant (C_c):

$$T_{bulk} = \frac{1}{2\pi} \ln\left(\frac{R_{infl}}{r}\right)\left(\frac{Q}{s_w}\right) = C_c S_c \tag{23}$$

where T_{bulk} is the bulk transmissivity of the soil (m^2/s)
C_c is the specific capacity coefficient
R_{infl} is the radius of influence of the pumping well (m)

Therefore, to solve for C_c one must assume an area of influence for the pumping event (semi-analytical) or instead use a reported value for a comparable aquifer system. As this becomes somewhat subjective, a C_c value of 0.5 and 1 were used to span the likely range of PEI aquifers, as proposed by Mace (2001) for hard rock fractured systems and alluvial sediments, respectively. Other analytical solutions often require an estimate of storativity of the aquifer surrounding the well, which also introduces subjectivity into the analysis (Mace, 2001; Maliva, 2016).

Section 2.2 – Empirical Relationships

Published empirical approaches to compute transmissivity from specific capacity are also compiled in Mace (2001) in the general form of:

$$T_{bulk} = \xi S_c^{b_1} \tag{24}$$

where ξ is a fitting coefficient determined via regression analysis
b_1 is a fitting coefficient determined via regression analysis
S_c is the specific capacity of the soil (m^2/day)

Huntley, Nommensen, and Steffey (1992) developed a relationship for fractured rock, as they found that previously developed analytical methods were overestimating transmissivity. Mace (1997) found reasonable agreement between two empirical relationships derived from different fractured karst aquifers, suggesting the transferability of empirical relationships between comparable systems. However, Mace (2001) cautioned that the applicability of the relationship developed by Huntley et al. (1992) to other comparable systems is still unclear. In addition, sample size should likely exceed 25 for meaningful relationships to be constructed (Mace, 2001), and it is unclear how many samples were used to derive the Huntley et al. (1992) relationship.

None of the aquifer descriptors for the published empirical equations reviewed by Mace (2001) seem to ideally match what is known about the aquifers of PEI. Thus, three empirical equations for fractured systems, with applicable ranges of transmissivity and specific capacity, were applied to yield a range of possible values for consideration (Table 28). The models selected are for fractured hard rock and fractured/karstic carbonate aquifers because their hydraulic conductivities are generally expected to be in the same range as semi-consolidated and fractured sandstones (Heath, 1983).

Table 28. Parameters for three empirical equations used to infer hydraulic properties of aquifers based on their specific capacity. Equations are compiled in Mace (2001).

Author(s)	**Calibration Aquifer**	ξ	b_1	**R^2**	**Sample Number**	**Range of T/S_c (m^2/d)**
Huntley et al. (1992)	Fractured hard rock	0.12	1.18	0.89	NA	16 – 16,000
El-Naqa (1994)	Fractured carbonate	1.81	0.92	0.95	237	3 – 20,000
Mace (1997)	Fractured/karstic carbonate	0.76	1.08	0.89	71	1 – 100,000

APPENDIX D: SOIL-WATER CHARACTERISTIC CURVE PARAMETERISATION METHODS

The parameters of a soil-water characteristic curve within SHAW control the soil wetting dynamics and their impact on the hydraulic and thermal properties of the aquifer. This section briefly reviews the procedure used in this study to compute the Brooks and Corey (1966) parameters using moisture-retention information available for the Charlottetown soil series of PEI (i.e., Carter, 1987; J. I. MacDougall et al., 1988). Brooks and Corey (1966) defined the effective saturation (S_e) as:

$$S_e = \frac{S_x - S_{irr}}{1 - S_{irr}} \tag{25}$$

where S_e is the effective saturation
S_x is the relative saturation at a given capillary pressure
S_{irr} is the relative saturation residual

There is ambiguity surrounding the definition of the relative saturation residual, though the authors themselves suggest that the saturation residual is comparable to the irreducible limit for moisture retention in Equation 25 (Brooks & Corey, 1966). Thus, the average moisture retention at -1500 kPa was used for the Charlottetown soil series as an initial estimate of the saturation residual, where no data for greater pressures were available, and this value ($S_{irr} \approx 0.15$) was in reasonable agreement with the values used in Brooks and Corey (1966), which ranged from 0.085 for glass beads to 0.58 for a consolidated sandstone (Brooks & Corey, 1966). Brooks and Corey (1966) plotted effective saturation against capillary pressure on log-log axes for various materials and found that generally:

$$lnS_e = -\lambda ln|P_c| + \lambda \ln\ |P_b| \qquad for \qquad P_c \geq P_b \tag{26}$$

where P_C is capillary pressure (Pa)
P_b is the air-entry pressure (Pa)
λ is the pore size distribution index

They concluded that the pore size distribution index and air-entry pressure may be extracted graphically by fitting the log-linear segment of the relationship between effective saturation and capillary pressure. The air-entry pressure can be determined by visually inspecting the graph or by setting S_e=1 in Equation 26, and the pore size distribution index is the slope of the log-linear regression of the linear portion. This method requires an assumed value of the irreducible moisture content (S_{irr}), though this can be adjusted to improve linear fit (Brooks & Corey, 1966). The resolution of the data available from MacDougall et al. (1988) and Carter (1987) did not permit the informed adjustment of the irreducible moisture content. In addition, there was no way to assess if the irreducible moisture limit was reached at -1500 kPa, so a probable range of irreducible moisture content between 5-24% for the log-linear method was tested.

Alternatively, the Brooks and Corey (1966) parameters may be inferred by fitting the Brooks and Corey (1966) model to the observation data using a optimisation algorithm. This method does not require an estimate of the irreducible moisture content (S_{irr}), as it can be regarded as a calibration parameter, along with the pore distribution index (λ) and air-entry pressure (P_b). During this process, the following form of the model equation was used for relative moisture content (modified from Schwartz & Zhang, 2003):

$$S_x = \left(\left|\frac{P_b}{P_c}\right|\right)^{\lambda}(1 - S_{irr}) + S_{irr} \quad \text{when Pc} > \text{Pb}\,, \tag{27}$$

wherein all parameters have been previously defined and the absolute value bars are to avoid confusion with directional references. A generalised reduced gradient solver was used to optimise the fit of the Brooks and Corey (1966) model using the minimisation of the root mean squared error (RMSE) as the optimisation criterion. An RMSE of 0 indicates a perfect model fit to the data, and it has been proposed that an RMSE of less than half the standard deviation is a very good fit in hydrological applications (Moriasi et al., 2007; Singh et al., 2004). Thus, it was convenient to express the RMSE normalised with respect to the standard deviation (referred to as the RSR) to evaluate model performance. The standard deviation was assumed to be that of the population (*StDev.P*), so that the RMSE values were more stringent than if the data were considered a sample. For reference, the equation used for RMSE was (Moriasi et al., 2007; Singh et al., 2004):

$$RMSE = \sqrt{\frac{\sum_{i=1}^{i}(x_{obs} - x_{model})^2}{\eta}} \tag{28}$$

and the equation for RSR was:

$$RSR = \frac{RMSE}{StDev.P} = \frac{\sqrt{\sum_{i=1}^{i}(x_{obs} - x_{model})^2}}{\sqrt{\sum_{i=1}^{i}(x_{obs} - x_{mean})^2}} \tag{29}$$

where	x_{obs}	is the observed parameter value
	x_{model}	is the modelled parameter value
	x_{mean}	is the mean of the observed values
	η	is the sample size

The parameters of the Brooks and Corey (1966) model determined by the curve fitting method were assessed based on their relative RSR values. These parameter estimations, as well as those determined using the log-linear method, were compared against literature values (e.g., Table 29) to make informed approximations of the pore size distribution index and air-entry pressure for the SHAW simulations.

Various literature values for Brooks and Corey (1966) parameters for soil types that could potentially be comparable to the Charlottetown soil series are listed in Table 29 for reference. The estimations present in the literature are expansive and are challenging to interpret due to the variable methods used in their determination (Table 29). Lappala, Healy, and Weeks (1987) tabulated S_{irr} values between 0-52%, P_b values between 11-145 cm H2O, and λ between 0.22-4.4 (see Lappala et al. (1987) p.21-22 for source studies). Alternatively, Brooks and Corey (1966) reported S_{irr} values between 8-57%, P_b values between 28-150 cm H2O, and λ between 1.8-7.3. Xing, Wang, and Ma (2018) characterised loams and sandy loams with S_{irr} values between 0-12.5%, P_b values between 42-64 cm H2O, and λ between 0.45-0.5 (assuming 100% initial relative saturation). Ma, Zhang, Lai, and Wang (2016) reported P_b between 8-25 cm H_2O and λ between 0.228-1.316 for various sands and sandy loams. These data were considered when parameterising soils in the SHAW simulations, in conjunction with the results of the soil-water characteristic curve analysis.

Table 29. Compiled literature values for the Brooks and Corey (1966) calibration parameters for soil types that are potentially comparable to the Charlottetown soil series and underlying bedrock.

Soil Type	K (m/day)	Porosity (%)	$\|P_b\|$(cm)	λ	S_{irr} (%)
Sandy loam[a]	-	50.2	54.0	0.45	8.0
Sandy loam[a]	-	32.7	58.0	0.49	9.2
Loam[a]	-	36.3	64.5	0.45	0
Loam[a]	-	48.1	42.0	0.5	12.5
Sand (20 mesh)[b]	7000	36	11.2	2.5	3.1
Medium sand[b]	400	37.5	14.9	0.84	0
Unconsolidated sand[b]	8.5	42.4	11.4	4.4	21.2
Sand[b]	8.2	43.5	19.6	0.84	0
Fine sand[b]	2.1	37.7	82	3.7	16.7
Sandy loam[b]	0.70	49.6	85	1.6	22.2
Silt loam[b]	0.22	43.0	145	1.7	22.1
Sandstone[b]	0.15	25	106	2.9	52
Loam[b]	0.39	42	141	0.51	31.0
Silt[b]	0.013	44.9	33.8	0.22	0
Light clay[b]	0.011	49.5	18.1	0.25	11.1
Sand[c]	-	36.5	32	2.3	15.7
Glass beads[c]	-	38.3	58	7.3	8.5
Fine sand[c]	-	36.0	82	3.7	16.7
Silt loam[c]	-	46.9	150	1.8	27.0
Fragmented mix[c]	-	44.1	34.4	2.9	27.6
Sandstone[c]	-	20.6	86	3.7	29.9
Sandstone[c]	-	25.0	108	4.2	57.7
Sand (from river) [c]	-	36.4	28	3.4	12.5
Silty clay loam[c]	-	45.5	72	2.3	25.0
Loam[d]	0.27	45	10	0.263	-
Sandy loam[d]	0.30	48	8	0.284	-
Sand[d]	0.70	38	11	0.449	-
Sandy loam[d]	0.24	47	10	0.228	-
Sand[d]	0.70	42	25	0.499	-
Sandy loam[d]	0.97	44	22	1.316	-

[a] *Xing et al. (2018)*

[b] *See Lappala et al. (1987) for source documents.*

[c] *Brooks and Corey (1966), converted from cm oil.*

[d] *Ma, Zhang, Lai, and Wang (2016) using a method based on constant pressure head absorption.*